Experimental Investigation of Turbulent Flows at Smooth and Rough Wall−Cylinder Junctions

Nikolaos Apsilidis

Dissertation submitted to the faculty of the Virginia Polytechnic Institute and State University in partial fulfillment of the requirements for the degree of

Doctor of Philosophy

In

Civil Engineering

Panayiotis Diplas, Chair

Clinton L. Dancey

Gregory D. Boardman

William H. Woodall

December 11, 2013

Blacksburg, VA

Keywords: Junction Flows, Turbulent Horseshoe Vortex, Reynolds Number and Roughness Effects, Bridge Scour, Particle Image Velocimetry

Experimental Investigation of Turbulent Flows at Smooth and Rough Wall-Cylinder Junctions

Nikolaos Apsilidis

ABSTRACT

Junction flows originate from the interaction between a fluid moving over a wall with an obstacle mounted on the same surface. Understanding the physics of such flows is of great interest to engineers responsible for the design of systems consisting of wall-body junctions. From aerodynamics to turbomachinery and electronics to bridge hydraulics, a number of phenomena (drag, heat transfer, scouring) are driven by the behavior of the most prominent feature of junction flows: the horseshoe vortex system (HVS). Focusing on turbulent flows, the complex dynamics of the HVS is established through its unsteadiness and non-uniformity. The fundamentals of this dynamically-rich phenomenon have been described within the body of a rapidly-expanding literature. Nevertheless, important aspects remain inadequately understood and call for further scrutiny. This study emphasized three of them, by investigating the effects of: model scale, wall roughness, and bed geometry. High-resolution experiments were carried out using Particle Image Velocimetry (PIV). Statistical analyses, vortex identification schemes, and Proper Orthogonal decomposition were employed to extract additional information from the large PIV datasets. The time-averaged topology of junction flows developing over a smooth and impermeable wall was independent of the flow Reynolds number, Re_D (parameter that expresses the effects of scale). On the contrary, time-resolved analysis revealed a trend of increasing vorticity, momentum, and

eruptions of near-wall fluid with Re_D. New insights on the modal dynamics of the HVS were also documented in a modified flow mechanism. Wall roughness (modeled with a permeable layer of crushed stones) diffused turbulence and vorticity throughout the domain. This effect manifested with high levels of intermittency and spatial irregularity for the HVS. Energetic flow structures were also identified away from the typical footprint of the HVS. Finally, a novel implementation of PIV allowed for unique velocity measurements over an erodible bed. It was demonstrated that, during the initial stages of scouring, the downflow at the face of the obstacle becomes the dominant flow characteristic in the absence of the HVS. Notwithstanding modeling limitations, the physical insight contributed here could be used to enhance the design of systems with similar flow and geometrical characteristics.

Acknowledgments

I would like to express my gratitude to my advisor, Professor Panos Diplas, for his continuous support throughout my PhD studies. From the very beginning until now, he has invested numerous resources to the success of this work. I thank him for the intellectual stimulation he has provided to me through the unconditional sharing of his expertise and wisdom. I regard every single interaction with him as a unique opportunity to become a better researcher and person. I hope this will not be the last time that I am expressing my appreciation for everything he has done for me.

I also thank the co-chair of the Advisory Committee, Professor Clint Dancey, for several dozens of reasons! For instilling me the passion to perform high-quality experimental work, his time, understanding, generosity, patience, support (moral and financial), mentoring, troubleshooting, sharing, encouraging …(the list goes on)…

Professor Boardman: thank you for your thoughtful comments and suggestions for the improvement of this work. In addition to these academic contributions, I will always be indebted to you for the positive impact you had on my life in general.

Professor Bill Woodall deserves my gratitude for introducing me to the exciting world of Experimental Design. Through his instruction in class and the insightful discussions we held at his office, I realized that there is so much more to experimentation beyond the typical engineering approach. Regardless of how much of this I was able to put into this work, I am confident that the knowledge I acquired through these interactions will be of paramount importance for my professional career.

My labmates at BEHL are credited for giving me one more good reason to visit the lab every day. Celso Castro-Bolinaga, Polydefkis Bouratsis, Ahmet Celik, Brandon Dillon, Billy Kingston, David Liu, Soonkie Nam, and Richard Zavaleta: thank you for the good times you shared with me. You never spared your help when I had asked for it. I hope that I have also managed to reciprocate the assistance and kindness.

I owe many thanks to the director and the researchers of AETHER lab. Professor Pavlos Vlachos was the one who guided my first steps with Particle Image Velocimetry. He has been willing to share his expertise in support of my work and has been consistently providing the means to run every PIV test included in this dissertation. Critical assistance was provided (one way or another) towards the successful completion of experiments by: Nick Cardwell, Matt Giarra, David Hubble, Cassie Niebel, Jaime and Sam Raben, Chris Weiland.

I would like to thank every professor that has contributed to my academic and broader education. I will be always grateful to the late Professor Vasilios Dermissis of the Aristotle University of Thessaloniki (AUTh). Excluding members of my family, he had been the person that has helped me the most in my life so far. Professors Christoforos Koutitas, Konstantinos Katsifarakis, and Pericles Latinopoulos (also of AUTh) deserve recognition for their continuous support and encouragement of my academic endeavors.

I acknowledge the opportunity that Virginia Tech gave me to pursue studies at the highest level under its auspices. I thank the Departments of Civil and Environmental Engineering and Mechanical Engineering for the financial support, the Graduate Student Assembly for sponsoring my travels to conference venues, and the many people of the Hokie community (administrative personnel, technicians, classmates, students) for enhancing my graduate life experiences.

My research at Virginia Tech would have never been completed without the generous financial support from: Academy of Athens (Argyropoulos Fellowship), American Society of Civil Engineers (J. Waldo Smith Hydraulic Fellowship), Gerondelis Foundation, Edna Bailey Sussman Foundation, Matthew G. Gwaltney Memorial Fellowship, Geological Society of America (Research and Travel Grants), CUAHSI (Pathfinder Graduate Student Fellowship), NortekUSA (Student Equipment Grant), Sigma Xi (Grants-in-Aid-of-Research Award), NUCOR (EWR Student Travel Grant).

Last, but not least, I would like to express my gratitude to my family for their unconditional love and support of my efforts to fulfill my dreams.

Table of Contents

List of figures

List of Tables

Attribution

The main body of this dissertation consists of three self-contained Chapters (2-4). These Chapters follow the journal manuscript format and have been submitted or will be submitted for publication to journals in the area of Fluid Mechanics. The following individuals serve as co-authors on one or more of these manuscripts.

Professor Panayiotis Diplas of the Civil and Environmental Engineering Department (Lehigh University) is the PhD Committee Chair. He has contributed in the design of experiments. Dr. Diplas also reviewed and revised the manuscripts.

Associate Professor Clinton L. Dancey of the Mechanical Engineering Department (Virginia Tech) is the PhD Committee Co-Chair. He participated in the experimental design, reviewed, and revised the manuscripts.

Mr. Polydefkis Bouratsis of the Civil and Environmental Engineering Department (Virginia Tech) is a PhD candidate and member of the research group. He is expected to review and revise the manuscripts prior to their final submission.

1 Introduction

1.1 Motivation, objectives and overview

Research on junction flows is motivated by the numerous applications featuring this characteristic geometry. A fluid moving around a wall−body juncture is commonly observed in aerodynamics (wing−fuselage), underwater-vehicle hydrodynamics (sail−hull), turbomachinery (fin-and-tube heat exchangers), electronics (capacitor−board), river engineering (streambed−rigid vegetation), and infrastructure hydraulics (streambed−bridge pier). Whereas these systems do not serve necessarily the same purposes, their operation is drastically affected by the flow physics. This is because the behavior of the distinct patterns comprising the junction flow (separated boundary layer, horseshoe vortex system-HVS, downflow at the face of the pier, reversed near-wall jet) is linked to generic processes such as mixing, heat transfer, drag, and sediment erosion. The prediction of these interactions is therefore a prerequisite for sound engineering designs.

Our limited understanding on some aspects of the phenomenon provided additional incentive for this work. Despite the recent strides in physical and computational modeling, important questions remain unanswered. This is the case even for the relatively well-studied setup consisting of a hydraulically smooth and impermeable wall. One such question is with respect to the validity of results for a variety of temporal and spatial scales. For most cases of practical interest, measurements or simulations at near-prototype configurations are very expensive (and occasionally, not even doable). It is therefore important to evaluate the confidence limits within which results from smaller-scale models could be projected to larger ones. One way to express these effects of scale is using Re_D, the Reynolds number based on the bulk flow and the diameter of the body comprising the junction. So far, the extent of Re_D-dependence (or invariance) on junction flow dynamics remains poorly understood.

Very little is also known about the junction flow behavior over a fully rough wall. Studies employing idealized roughness geometries constitute only rudimentary approximations of the phenomenon. Nevertheless, realistic models are needed that more accurately represent the irregularities of roughness elements in real-life problems (bridge pier scour, aerodynamics of damaged wing−fuselage junctions). Finally, not a single study exists in the literature that reports global flow measurements at junctions with a mobile bed, without prior significant modifications to the physical setup. Considering that bridge scour is the leading cause of bridge failure, there is a dire need for such studies to be conducted.

The overall purpose of this work was to contribute an enhanced understanding on the aforementioned subjects based on physics-based investigations. More specific objectives are highlighted with the following questions:

- What are the effects of model scale on junction flow dynamics?
- In turbulent flows, is the modal behavior of the HVS independent of Re_D?
- How does roughness affect the large-scale unsteadiness of the HVS and the behavior of the junction flow in general?
- Is it possible for bridge scour experimental investigations to capitalize on the benefits of PIV without introducing unrealistic modifications to the models?
- Is there a dominant flow mechanism at the initial stages of scouring activity?

Answers to these questions were sought through physical modeling. The experimental campaign consisted of five tests. Three of them (at varying levels of Re_D) were performed on a smooth and impermeable wall. Another took place using a rough, permeable, but immobile bed. The final test used a rough, permeable, and mobile wall. Replications were administered for one experiment representing each wall configuration. The junction geometry was formed using a cylinder as the obstacle perturbing the incoming flow. In all cases, the state-of-the-art flow diagnostic tool of Particle Image Velocimetry (PIV), was employed. Planar velocity measurements were collected at the centerline junction adjacent to the leading edge of the cylinder and further upstream, within the approach boundary layer. The analysis and conclusions presented here are primarily based on the former datasets.

1.2 Dissertation outline

This dissertation is structured according to the journal article format. Namely, the layout of each one of the three subsequent chapters follows that of a typical manuscript with separate abstract, introduction, methodology, results, and discussion sections. Whereas each chapter has a per se merit, it is also helpful to consider their role within the bigger picture of turbulent junction flows. Furthermore, the sequence of the chapters is consistent with the chronological order of the subtasks of the research investigation. This allows for a better appreciation of the findings (and additional questions) that emerged as the project evolved.

Horseshoe vortex and flow dynamics at a smooth wall−cylinder junction are examined in Chapter 2. The experimental investigation of this basic configuration set the stage for inquiries included in ensuing sections of this dissertation. Emphasis was placed on the effects of scale, as expressed with Reynolds number. Three levels of Re_D were used. A painstaking study of the time-resolved dynamics of the flow unveiled the structural similarities and differences in the behavior of the turbulent horseshoe vortex. Statistical tools were also employed to quantify the unsteadiness of the organized flow patterns in both space and time. It is shown that Re_D-dependence should be considered in designs aiming at junction flow control.

Chapter 3 discusses the physics of junction flows developing over a rough and permeable wall. Extensive comparisons are reported between this setup and a benchmark one comprising of a smooth and impermeable boundary. Proper Orthogonal Decomposition (POD) is applied on flow velocity signals to complement conventional data analysis techniques based on Reynolds decomposition. Whereas qualitative and quantitative agreement is also reported here, the most striking findings of this work refer to the structural changes of flow induced by the porous and rough wall. The understanding of the role of energetic flow structures on the phenomenon is enhanced through the examination of the dominant POD modes.

In Chapter 4, the scope of the investigation is extended to include the effect of deformable bed geometry. The experimental setup is relevant to the engineering application of bridge scouring. A novel implementation of the PIV technique is presented. This is the first time that synchronized data of global flow velocities and bed elevation around a model pier were obtained in a non-intrusive fashion. The focus was on the initial stages of the scouring phenomenon. It is demonstrated that the downflow at the face of the pier is the predominant flow feature, in the presence of an active scour hole.

Finally, the main conclusions of this study are summarized in Chapter 5. Insights about future endeavors in junction flow research are also shared.

2 Time-resolved flow dynamics and Reynolds number effects at a wall−cylinder junction

Nikolaos Apsilidis, Panayiotis Diplas, and Clinton L. Dancey

ABSTRACT: This study investigated the physics of separated turbulent flows near the vertical intersection of a flat wall with a cylindrical obstacle. The geometry imposes an adverse pressure gradient on the incoming boundary layer. As a result, flow separates from the wall and reorganizes to a system of characteristic flow patterns known as the horseshoe vortex. We studied the time-averaged and instantaneous behavior of the turbulent horseshoe vortex using planar Time-Resolved Particle Image Velocimetry. In particular, we focused on the effect of Reynolds number based on the diameter of the obstacle and the bulk approach velocity, Re_D. Experiments were carried out at Re_D: 2.9×10^4, 4.7×10^4, and 12.3×10^4. Data analysis emphasized time-averaged and turbulence quantities, time-resolved flow dynamics, and the statistics of coherent flow patterns. It is demonstrated that two large-scale vortical structures dominate the junction flow topology in a time-averaged sense. The number of additional vortices with intermittent presence does not vary substantially with Re_D. In addition, the increase of turbulence kinetic energy, momentum, and vorticity content of the flow at higher Re_D is documented. The distinctive behavior of the primary horseshoe vortex for the $Re_D=12.3\times10^4$ case is manifested by episodes of rapid advection of the vortex to the upstream, higher spatio–temporal variability of its trajectory, and violent eruptions of near-wall fluid. Differences between this experimental run and those at lower Reynolds numbers were also identified with respect to the spatial extents of the bimodal dynamics of the horseshoe vortex, which is a well-known characteristic of turbulent junction flows. Our findings suggest a modified mechanism for the aperiodic switching between the dominant flow modes. Without disregarding the limitations of this work, we argue that Reynolds number effects need to be considered in any effort to control junction flows characterized by the same (or reasonably similar) configurations.

2.1 Introduction

2.1.1 Definitions and problem statement

The interaction of a turbulent boundary layer developing over a flat bed with an obstacle mounted on the same surface drastically alters the flow dynamics. Increasing pressure gradients induced by the obstacle trigger the separation of the incoming flow. Downstream of the separation line, the fluid’s momentum and vorticity reorganize into coherent flow structures, which manifest themselves at larger spatial scales than those comprising the boundary layer. These horseshoe vortices wrap around the front and the flanks of the obstacle. Their presence dominates locally the mechanisms of momentum and heat transfer. Together with the horizontal boundary layer propagating parallel to the wall and the secondary one developing along the upstream face of the obstacle, the horseshoe vortex system comprise what is collectively known as the junction flow.

The generic geometrical configuration, which characterizes junction flows, is observed in a number of applications. For example, the wing−fuselage junction plays an important role in aircraft aerodynamics. Similarly, the sail−hull configuration on submarines acts as a vertical stabilizer that controls the navigability of the vessel. In turbomachinery, fin-and-tube heat exchangers of juncture geometry are used to enhance heat transfer between adjacent media. Even at smaller scales, the corner shaped between capacitors and electrical circuit boards affects the ventilation of the system. Lastly, the turbulent horseshoe vortex developing at the base of bridge piers embedded in loose riverbeds is considered one of the major contributors to the bridge scouring phenomenon, which has been recognized as the leading cause of bridge failure.

As it is implied from these examples, the range of geometric and temporal scales characterizing junction flows can easily span several orders of magnitude. It is therefore crucial to know if (and how) scale effects modify the fundamental characteristics of flow behavior. In a more rigorous formulation of the problem, the effects of scale could be expressed with Reynolds number. This dimensionless parameter incorporates both time and length scales in its definition. Although other options are possible, the Reynolds number based on the depth-averaged approach velocity (U_o) and the diameter of the obstacle (D), $Re_D = \frac{U_o D}{\nu}$, where v is the kinematic viscosity of the fluid, has been typically used in junction flow research. In conclusion, knowledge of Reynolds number effects on the flow physics is pivotal for carrying out model studies, generalizing results applicable from one setup to another, and, ultimately, for designing robust engineering systems that include juncture configurations.

2.1.2 Junction flow dynamics

Unsteadiness and non-uniformity are integral elements of turbulent junction flows. The complexity of flow characteristics in time and space explains the difficulties researchers faced in their early attempts to map the flow topology. Traditional flow diagnostic tools, such as point-wise velocity measuring techniques and flow visualizations, can provide only rough approximations of the dynamics of coherent flow patterns. Consequently, discrepancies existed regarding the interpretation of both time-averaged and instantaneous features of fundamental junction flow setups (i.e. those that excluded effects of obstacle shape and aspect ratio, flow angle of attack, degree of obstacle submersion or bed geometry). Varying results have been reported regarding the number of vortices comprising the horseshoe vortex system and its dependence on Re_D (Baker 1979; Ishii & Honami 1986; Dargahi 1989; Eckerle & Awad 1991; Fleming *et al.* 1993). The advent of global flow diagnostic techniques (Particle Image Velocimetry-PIV) and the development of sophisticated methodologies for numerical simulations (Detached Eddy Simulation- DES) increased the confidence in obtained data. In this way, some of the aforementioned ambiguities were resolved. More recent studies employing the state-of-the-art in physical and numerical modelling (Praisner & Smith 2006b; Paik, Escauriaza & Sotiropoulos 2007; Kirkil & Constantinescu 2009; Sabatino & Smith 2009; Escauriaza & Sotiropoulos 2011c) showed that the time-averaged horseshoe vortex system consists of: 1) a primary vortex (HV1), which rotates in a clockwise sense (assuming that flow enters the junction region from the left), 2) a secondary vortex (HV2) again with a clockwise sense of rotation and located upstream of HV1, and 3) a corner vortex (CV) of counterclockwise rotation positioned downstream of HV1. A tertiary vortex (HV3) is frequently resolved in instantaneous topologies and is located at the saddle between HV1 and HV2 (Praisner & Smith 2006a; Gand *et al.*

2010; Escauriaza & Sotiropoulos 2011c). Occasionally, the cinematography of the flow field reveals various smaller and short-lived vortical structures upstream of HV2. However, the dependence of the dynamics of the instantaneous junction vortices, including their number, on Re_D remains unclear (Dargahi 1989; Escauriaza & Sotiropoulos 2011c).

In a study that set the stage for many of the posterior researches, Devenport & Simpson (1990) introduced what is now considered as the signature characteristic of junction flows: the bimodal unsteadiness of the horseshoe vortex system. Through meticulous execution of experiments and innovative data analysis, they demonstrated that the horseshoe vortex alternates quasi-periodically between two states. The first one was named *backflow mode*, because it was characterized by a strong, near-wall flow moving opposite to the bulk flow. Due to its high-momentum, this jet propagates far upstream of the junction. The second state, known as *zeroflow mode*, exists when the path of the reversed flow is blocked by incoming fluid. This results in the vertical ejection of the return flow at high velocities. The presence of the backflow mode is three to four times more probable than that of the zeroflow mode. The switching between the modes occurred at irregular and relatively long time intervals (low frequencies). Devenport & Simpson (1990), hypothesized that the backflow mode is the result of the inrush of high-momentum, low-vorticity fluid originating from the inviscid free-stream. On the contrary, the dynamics of the zeroflow mode were linked to low-momentum, high-vorticity fluid coming from the outer region of the boundary layer. Though the collected data probed the flow locally at a few points of the domain, they did not allow the confirmation of this hypothesis. More recent studies, based on DES numerical simulations, however, have supported its validity (Kirkil, Constantinescu & Ettema 2006; Kirkil & Constantinescu 2009).

The bimodal unsteadiness is an important characteristic of junction flows. Its presence has been linked to elevated turbulence stresses in the junction region (Devenport & Simpson 1990; Paik *et al.* 2007; Kirkil & Constantinescu 2009). Sediment transport studies (Escauriaza & Sotiropoulos 2011b; Escauriaza & Sotiropoulos 2011a) have suggested that the variation in shear stresses occurring during the transition from backflow to zeroflow mode is the major cause of scouring around a bridge pier. In addition to flow momentum, the bimodal behavior characterizes heat transfer (Praisner *et al.* 1997) and the fluctuations of the hydrodynamic forces on the wall of the junction (Agui & Andreopoulos 1992; Olcmen & Simpson 1994; Kirkil & Constantinescu 2009). These examples justify the interest in deciphering the underlying physics of the phenomenon. A number of interpretations are available in the literature. For instance, Devenport & Simpson (1990) attributed the bi-stable behavior of the horseshoe vortex to fluctuations in the momentum and vortical content of the outer region of the boundary layer. Praisner & Smith (2006a) related the switching between the two extreme modes to the interaction of two flows of opposing direction: an inrush of fluid originating from the upstream boundary layer and the reverse flow away from the obstacle's face. In the same study, the existence of additional flow modes was suggested. The phenomenon has been more extensively examined via numerical studies. For example, Kirkil *et al.* (2006) contributed further insights regarding the interaction of vortices, such as the destabilization of the primary vortex due to collisions with the secondary ones. Paik *et al.* (2007) argued that packets of hairpin vortices wrap around the primary vortex, cause its disintegration, and eventually signal the transition from backflow mode to the zeroflow mode. These small-scale flow structures originate from centrifugal instabilities, which in turn result from the interaction between the primary vortex and the wall. Escauriaza & Sotiropoulos (2011c) explored the implications of this mechanism with respect to its dependence on Re_D. Their DES data revealed that the number, the frequency of appearance, and the intensity of the hairpins increase with Re_D.

Regardless of its connection to the bimodal behavior of the horseshoe vortex, the eruption of near-wall fluid is per se a prominent feature of junction flows. The unsteady motion of HV1 occasionally brings the bottom streamlines of the vortex very close to the wall. This interaction brings about the violent extraction of wall fluid, which is characterized by vorticity of opposite sign compared to that of HV1. The intensity of eruptions is expressed with high levels of turbulence kinetic energy near the wall (Escauriaza & Sotiropoulos 2011c). The entire eruptive process is sporadic. According to experimental results (Agui & Andreopoulos 1992), there are instances where the entrained fluid rolls up to form a counterclockwise vortex (HV3), which partially fills the space between HV1 and HV2. At other occasions, ejected patches of fluid are advected along the periphery of the primary vortex. Eventually they merge with the vortex core or diffuse into the surrounding flow (Praisner *et al.* 1997; Sabatino & Smith 2009). Such episodes do not support the premise that the small-scale, wall-ejected vortices (hairpins) are the major destabilizing agents of HV1. In cases that eruptions are frequent enough, a continuous jet of fluid is created at an oblique angle to the wall. The jet acts as a barrier between HV1 and HV2, preventing the exchange of vorticity and momentum (Kirkil & Constantinescu 2009).

Another fundamental idea in junction flow research suggests that the seeds of the junction flow dynamics can be tracked within the characteristics of the incoming, boundary layer flow. Sabatino & Smith (2009) tested this hypothesis experimentally for a junction flow with $Re_D=1.9\times10^4$. They concluded that the bursts typically observed in a turbulent boundary layer occur at time scales comparable to those characterizing the extraction of vortical wall fluid by the primary horseshoe vortex. Similarities were also reported with respect to the frequencies characterizing the quasi-periodic switching between the zeroflow and the backflow mode. Agui & Andreopoulos (1992) extended the boundary layer−horseshoe vortex relationship and suggested that the length of wandering for HV1 scales with the boundary layer thickness. Fleming *et al.* (1993) inferred a pumping-like behavior of HV1 based on its interaction with the incoming boundary layer flow. The analogy drawn was that the primary horseshoe vortex brings high-momentum fluid from the outer flow into the junction region and at the same time ejects low-momentum fluid away from the near-wall region. The availability of high-momentum fluid within the boundary is instrumental for this mechanism to materialize. The findings and the overall approach of the aforementioned studies allude to the practice of altering the characteristics of the boundary layer, in an effort to manipulate the unsteadiness of the horseshoe vortex system. Nevertheless, prior to pursuing such solutions, it is necessary to validate the major characteristics of the boundary layer−horseshoe vortex interaction for a range of Re_D.

2.1.3 Scope and layout of the paper

Research on turbulent junction flows has capitalized on the recent strides in experimental and numerical modelling techniques. Nevertheless, several open issues call for additional investigation. Here, we explore one of them, namely the effect of

Reynolds number on the underlying mechanism that governs the dynamics of junction flows. We pursued our research goal experimentally, employing an established technique in resolving the physics of turbulent flows: Particle Image Velocimetry. High-resolution measurements were obtained at the upstream junction of a cylindrical pier and the flat bed of a water tunnel. Three cases were investigated and were named after the relative magnitudes of their Reynolds numbers. The one with the low $Re_D=2.9\times10^4$ is referred from now on as LRe, the second case at the middle $Re_D=4.7\times10^4$, MRe, and the high-Reynolds number case of $Re_D=12.3\times10^4$, HRe. Observe that for all cases the Reynolds numbers are well above the threshold that separates laminar from turbulent junction flows ($\approx1.2\times10^4-1.3\times10^4$). There is also nearly an order of magnitude difference between the numerical levels of Re_D for LRe and HRe, in an effort to cover a wider range of junction flow applications. Comparisons of turbulence statistics elucidated the intricate flow physics by revealing similarities and important differences among the three cases.

The layout of the subsequent sections of the article is as follows. First, in §2.2, we elaborate on the experimental procedures, the methodologies employed in our study as well as their limitations. Next, we compare the time-averaged features of a number of parameters characterizing the turbulent flows of interest (§2.3). The flow dynamics is further elucidated through the discussion that follows about the instantaneous flow fields. This analysis is complemented with a study of the probability density functions of the velocity components and their implications on the flow physics. Finally, we deduce the most important findings of this work and highlight its contributions in §2.4.

2.2 Experimental investigation

2.2.1 Facilities and physical model

Experiments were carried out at the premises of the Advanced Experimental Thermofluid Research Laboratory of Virginia Tech. A recirculating water tunnel with a transparent test section (0.61 m wide × 0.61 m high × 1.81 m long) was used. The facility is equipped with a set of screens, a honeycomb, and a 6:1 contraction section. The maximum freestream turbulence intensities for the velocities and flow depths of this study were less than 5% (Vlachos 2000).

Figure 2.1 illustrates the basic components of the physical model and the experimental setup. A cylinder was mounted vertically on the bottom of the channel and was suspended from its top using two aluminum bars (not shown in the figure). The center of the circular cross-section was carefully aligned with the centerline of the channel within ±1 mm. A flat black spray paint was applied on the outside surface of the cylinder to reduce undesirable reflections of laser light. A 5 cm-wide sand strip spanning the entire width of the channel was installed at the inlet of the test section. The average height of its distributed roughness elements was 1 mm. This item was used to artificially trip the incoming boundary layer, increase its thickness, and cause transition to turbulent flow.

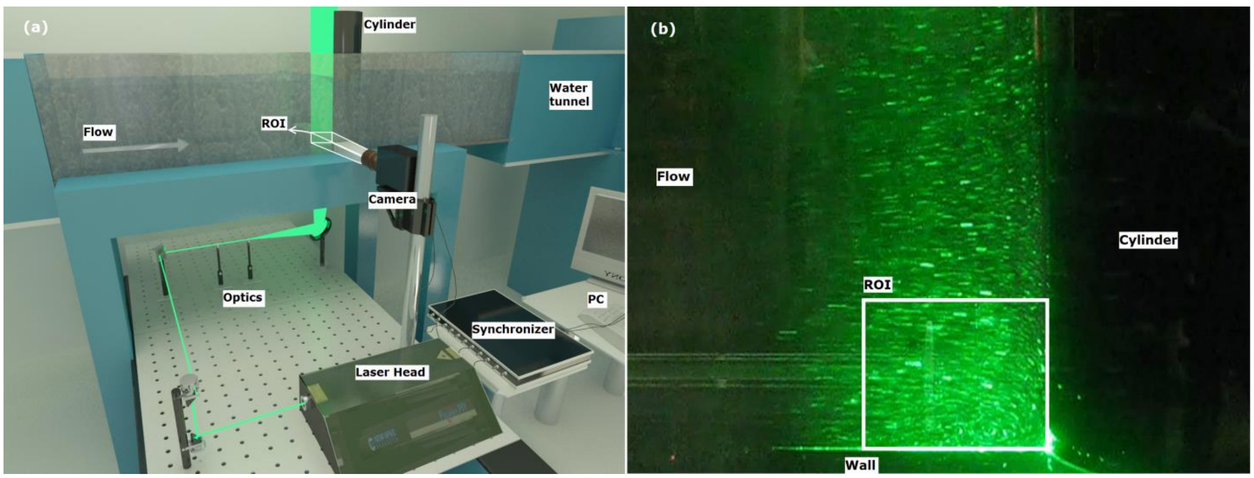

Figure 2.1- (a) Test section of the water tunnel, physical model, and basic features of the non-intrusive PIV technique. The region of interest (ROI) is highlighted with the white rectangle. (b) Close-up of ROI within a flow visualization photograph.

Due to limitations of the experimental facility, we had to obtain the selected levels of Re_D by modifying both the pier diameter and the approach flow velocity (table 2.1). Practically, this means that each run was characterized by different boundary layer thicknesses (δ_{99}) and channel blockage ratios. As mentioned in §2.1, there is some evidence in the literature that the thickness of the boundary layer affects at least some aspects of junction flows (Ballio, Bettoni & Franzetti 1998; Simpson 2001; Roulund *et al.* 2005). On the other hand, the influence of relatively thick boundary layers (δ_{99}>0.2D), like the ones in this study, is rather weak (Koken & Constantinescu 2009). In support of this statement, discrepancies in boundary layer thickness did not prevent recent numerical studies from reproducing important features of junction flows (Paik *et al.* 2007; Escauriaza & Sotiropoulos 2011c). In addition, blockage effects could be safely neglected for LRe and MRe cases, because the flow aspect ratios (channel width over flow depth) are higher than the critical number of five. The latter is known to be the threshold for the development of cross-flow circulation in the form of secondary currents (Nezu & Nakagawa 1993).

For all three experimental runs the flow depths (H) ensured that flow shallowness and flow patterns close to the free surface (superelevation of water surface, surface roller) have negligible effects on junction flow dynamics. This feature, in conjunction with the moderate levels of Froude numbers (Fr) selected, renders the results of this work comparable to those obtained from numerical simulations. However, it should be considered that such studies frequently model the free surface as a rigid-lid boundary (Ali & Karim 2002; Kirkil & Constantinescu 2010).

Table 2.1-Major geometric and flow characteristics of the experimental setups.

Case	U_o (m/s)	D (m)	H (m)	δ_{99} (m)	Fr	D/δ^+	$Re_\delta{}^+$	Re_θ	Re_D
LRe	0.442	0.060	0.150	0.054	0.36	12.77	2240	1570	2.9×10^4
MRe	0.486	0.089	0.180	0.077	0.36	10.11	4610	3250	4.7×10^4
HRe	0.673	0.169	0.250	0.089	0.42	29.14	4210	3120	12.3×10^4

As shown in figure 2.1, the primary flow measurements were performed at a streamwise−vertical plane located at the centerline of the upstream wall−cylinder junction. This region was selected because it: 1) is representative of the basic characteristics of junction flow, 2) experiences minimum disturbances due to effects from the channel's sidewalls, 3) exhibits relatively small cross-plane fluid motion, and 4) provides a good reference for comparison with past studies. Flow measurements were also taken at the inlet of the test section for all three experiments. Streamwise and wall-normal velocity components were measured at a station located five diameters upstream of the leading edge of the cylinder. Again, the measurement plane was positioned on the centerline plane of symmetry. The same location was used for the characterization of the incoming boundary layers (refer to table 2.1 for the most important information regarding the boundary layer parameters, where δ^+ is the boundary layer displacement thickness and θ the boundary layer momentum thickness).

The fluid temperature was measured at various stations of the test section using a glass thermometer a few seconds before the initiation of data acquisition. It was found to be relatively constant at 23.5±0.1^{o}C. Due to the small sampling duration, it can be safely assumed that this quantity remained constant throughout. The temperature differential between flowing water and surroundings was 0.5±0.1^{o}C, rendering negligible any effects induced by temperature-gradient advection (Allen & Naitoh 2007).

2.2.2 Application of Particle Image Velocimetry

We applied a fundamental implementation of this technique, known as planar Time-Resolved Particle Image Velocimetry (TRPIV). This generated multiple two-component velocity vectors over two-dimensional flow planes (2D2C version of PIV) with sufficient spatial and high temporal resolution.

Despite the ever-growing popularity of PIV methods, we are still lacking a comprehensive methodology to unambiguously evaluate the quality of the obtained results. Measurement error and related uncertainties generally depend on the flow under study, the experimental setup, the hardware comprising the PIV system, the data analysis algorithms, and the experimenter. Each one of these factors consists of several subcomponents. In addition, some of these errors do not remain constant over time and space.

An alternative approach embraces the use of single-factor effects on total error. This results in a set of "best practice guidelines" for the optimum application of planar PIV that could potentially be combined with uncertainty estimation methodologies (Timmins *et al.* 2012; Charonko & Vlachos 2013; Wilson & Smith 2013). The reader is referred to the books by Raffel *et al.* (2007) and Adrian & Westerweel (2011) (and included references), which provide an excellent documentation of PIV error assessment. Along these lines, we pursued the application of as many of these guidelines as possible to our experiments. Because we faithfully followed this methodology for each test, we anticipate similar levels of errors and related uncertainties for all three Re_D cases examined here. The good agreement we found between two replications of the MRe case attest to this statement. Next, we describe the outcomes of our efforts related to the use of PIV instrumentation, image processing and data analysis.

2.2.2.1 **Particle flow seeding and PIV equipment**

A basic premise in PIV is that tracing particles faithfully follow the paths of the water elements they displace. We seeded our flow with hollow glass particles. Their shape was nearly spherical, their mean diameter was d_p=35 μm, and their density had a nominal value of ρ_p=1080 kg/m^3. Using particles heavier than water generally results in underestimation of the velocity magnitude. Nevertheless, this effect is not expected to be relevant here due to the frequency content of the flows under study. The ratio of the particle response frequency to that of the characteristic flow frequency is known as the particle Stokes number: $St = \frac{\rho_p d_p^2 U_o}{18\mu \delta_{99}}$, where μ is the dynamic viscosity of water. Calculated St were 0.0066, 0.0051, and 0.0061 for the LRe, MRe and HRe cases respectively. Indeed, these values are low enough (<0.01) to ensure that seeding particles could respond without lag to changes in flow direction. Flow tracers were added in the recirculating water using trial-and-error, until a density of a minimum of ten particle images within random 16×16 pixel areas throughout the imaged flow domain was obtained. This particle density typically suffices for the good performance of PIV algorithms (Raffel *et al.* 2007).

A 20 W dual-cavity pulsed Nd:YLF laser (model: New Wave Pegasus) was used to illuminate the position of seeding particles at selected time instants. Each pulse had a wavelength of 527 nm, was fired at a frequency of 1,000 Hz, and emitted a nominal energy of 10 mJ. Using a convex lens with a focal length of 50 mm, a spherical lens with a focal length of 300 mm, and a series of mirrors, the beam was delivered in the test section through the transparent bottom of the channel (figure 2.1). A major advantage of this setup is the opportunity for non-intrusive measurements. In this way, there was no need for modifications of the setup that could potentially alter the nature of the phenomenon (for example, by installing a transparent lid to suppress surface waves and deliver the light through the free surface). The thickness of the laser sheet was 2.0±0.2 mm throughout the camera's field of view. We selected this thickness to effectively deal with out-of-plane particle motion: an important source of error in PIV measurements.

According to the guidelines, the light sheet should be thicker than the average out-of-plane motion of particles by a factor of four. In our tests, this factor was equal to 12.85 for the HRe case (worst case scenario due to higher free stream velocity). As a reference value for the maximum expected out-of-plane displacement, we used results from numerical simulations at Re_D comparable to that of HRe (Paik *et al.* 2007).

To achieve the desirable magnification of the region of interest, the distance between the center of the camera lens (Nikkor, with a focal length of 50 mm) and the CMOS sensor was adjusted using extension tubes. The final geometric configuration resulted in a maximum error of 1.35% affecting the outermost regions of the images due to deviations of the viewing angle from the optimum of 90^o. Autocorrelations of image intensities yielded an average diameter for the imaged particles of d_τ=2.3±0.5 pixel. A value close or higher than two pixel has been reported as sufficient to drastically mitigate pixel locking-induced errors (Raffel *et al.* 2007; Adrian & Westerweel 2011). Collecting data in the absence of ambient light allowed for images of higher signal-to-noise ratio (SNR). A lens' f-number of 5.6 was selected for all tests reported herein.

The resulting depth of field was 3.2±0.2 mm (>light sheet thickness, so that diffraction-limited images are captured) and the average magnification factor was equal to 63.52±0.19 μm/pixel. The Dynamic Velocity Range (DVR) of our PIV system was 134±7 (as calculated according to Adrian (1997)). The minimum DVR required to capture the flow for the high Re case (again, worst case scenario) was 120. The optical axis of the lens was perpendicular to the channel's sidewall to eliminate the unwanted effects stemming from refraction of light due to its propagation through different media (air, Plexiglas, water). The contrast of the images was optimized by traversing the camera on a linear slide with sub-millimeter resolution. Particle motion was tracked with a 1.3×10^6 pixel high-speed camera (model: XS-3, manufactured by Integrated Design Tools, Inc.), which was operated at a frequency of 1,000 Hz. With a Nyquist frequency of 500 Hz, we argue that our data adequately resolve the dynamics of the low-to-mid frequency flow components. In addition, the sampling frequency exceeded the characteristic frequency of the incoming flows ($f_c=U_o/\delta_{99}$) by 136.90±18.27 times on average. In particular, the calculated relevant frequencies for the LRe, MRe, and HRe cases were: 8.22 Hz, 6.36 Hz, and 7.58 Hz. These numbers are comparable with frequencies characterizing the dynamics of the horseshoe vortex according to previous studies (Devenport & Simpson 1990; Kirkil & Constantinescu 2009). The inter-frame time of 1ms assured maximum particle displacements between four and seven pixels for all Re cases. These numbers conform to the optimal "one-quarter" rule of particle displacements for the interrogation window used in the first pass of PIV analysis. Thus, we favored the single-frame mode for PIV data acquisition to: a) obtain maximum light intensity by the simultaneous firing of the two laser cavities, b) maximize the number of collected images, and c) minimize loss of correlation due to unequal exposures between consecutive images. As a result, 3270 frames filled the 4 GB-buffer of the camera for each Re_D case. The total sampling time of 3.27 s corresponded to an average of 24.5±1.4 characteristic times (δ_{99}/U_o) of the incoming flows. The maximum available image resolution of 1280 pixel ×1024 pixel was used. Consequently, the average dimensions of the imaged flow field was the same for all three experiments, 7.31 cm × 5.62 cm.

A timing hub (MotionPro by Integrated Design Tools, Inc.) was used to trigger and synchronize the laser unit with the camera with a resolution of 20 ns. The consistency of every TTL signal to and from the hub was double-checked using an oscilloscope.

2.2.2.2 **Image preconditioning and analysis**

Raw PIV images were characterized with high contrast (and therefore SNRs) in all regions except for those that were close to the fluid–solid boundary interfaces. There, the presence of intense light reflections was a caveat for spurious velocities. To mitigate this problem, we resorted to image preconditioning. The negligible pulse-to-pulse variation of laser intensity allowed the subtraction of the time-averaged mean image intensity from every frame (Honkanen & Nobach 2005). Additional enhancements were achieved by accurately defining the boundaries of the domain through gradient-based edge detection. To account for the undesirable contributions of some very bright particles in the resolution of the domain, we capped their intensity (Shavit, Lowe & Steinbuck 2007). Finally, an image mask was used to speed-up calculations by excluding no-flow regions (bed, cylinder).

We adopted a common analysis procedure for all three Re_D cases. PIV images were processed with software that implements the Robust Phase Correlation algorithm

(Eckstein, Charonko & Vlachos 2008; Eckstein & Vlachos 2009a, b). High shear and rotational flows (like those studied here) are notoriously difficult environments for collecting reliable PIV measurements. The local velocity gradients they introduce can result in significant variations of particle displacements (α) within the interrogation window. Adrian & Westerweel (2011) recommended that $\alpha \ll d_\tau$ (recall that d_τ is the average particle image diameter). For our data, α was two to three orders of magnitude smaller than d_τ in all areas of the flow domain. Regardless of the relationship between α and d_τ, the application of deformed interrogation windows is an established method to deal with this problem (Scarano 2002). Thus, multi-grid, iterative, and deformable windows were used to resolve the instantaneous flow fields. Three passes with two iterations in each were applied. The dimensions of the interrogation windows were reduced in each subsequent pass (from 64×64 pixels to 32×32 pixels to 16×16 pixels) to enhance the spatial resolution of the 2D velocity field. Each window overlapped by 50% with its adjacent ones in both x and y directions. In this manner, additional (though not independent from a statistical point of view) vectors were generated to improve the estimation of spatial derivatives. Before each pass, a Gaussian image filter with half the window resolution was employed to mitigate the effects of spectral leakage and wrap-around aliasing on the signal. In addition, a buffer was applied to the interrogation windows when positioned at the edges of the flow domain to prevent window clipping. Discrete Window Offsetting (Westerweel 1997) accounted for the loss of correlation signal in the second pass due to in-plain particle motion. Vector validation was performed based on velocity thresholding and the Universal Outlier Detection technique (Westerweel & Scarano 2005). The percentage of valid vectors derived from the PIV image analysis ranged from 96.5% to 99.7%. Spurious vectors were replaced with interpolated data from adjacent valid vectors. Sub-pixel displacements were resolved through the use of Gaussian peak-fitting. The final processed velocity fields had a uniform vector grid spacing of 8×8 pixels. On average, the Eulerian representation of the instantaneous, two-dimensional flow field was obtained using 17,828 velocity vectors. The total number of measurements collected for all three Re_D cases was 174,889,410.

2.2.2.3 **Data post-processing**

Apart from the length scales present in the flow field under study and the measurement error, the uncertainty in the values of derivative quantities calculated from planar PIV data (such as out-of-plane vorticity) depends on the numerical scheme used to estimate velocity derivatives. In some cases, the error increases by an order of magnitude, as a result of the poor spectral response of the selected differential operators (Foucaut & Stanislas 2002). To account for this problem, we used a compact fourth-order scheme with Richardson extrapolation. This hybrid operator has been shown to outperform conventional second-order finite difference schemes for the range of wavenumbers typically present in PIV data (Etebari & Vlachos 2005). Note, however, that some discrepancies in PIV vorticity data will exist regardless of the selection of the differential operator. These stem from contributions of the very small turbulence scales that remain under-resolved (Wallace & Foss 1995). Since this work focuses on the behaviour of larger turbulence scales, we expect that this effect is negligible.

2.3 Results and discussion

The first part of the presentation and discussion of our results is devoted to the prominent features of the time-averaged flow fields. We discuss the effects of Re_D on a number of turbulent statistics derived from the PIV data. Next, we probe into the time-dependent flow dynamics. The unsteady behavior of the dominant flow patterns is analyzed in an effort to reveal details that are filtered out, when averaged in time. Maps, tracking the trajectories of the primary horseshoe vortex in time, add important information to this discussion. Finally, we examine the probability density functions of velocity fluctuations to characterize the unsteady nature of junction flows studied here.

Most of the results are presented as maps of the spatial distribution of the parameter of interest on the measurement plane. The dimensions of the domain are scaled with the cylinder’s diameter. A constant area of 0.45D × 0.35D is illustrated in every figure included in this paper. These are the maximum dimensions of the flow field that PIV imaging captured for the HRe case. Note, however, that due to: 1) the different cylinder diameters among cases and 2) the constant spatial resolution of the measurements, the number of data points used to generate maps for each one of the three Re_D experiments is not the same. Whenever required, results are non-dimensionalized with the approach velocity or the characteristic time of the incoming flow. An asterisk is used to indicate dimensionless parameters. The convention that water flows from left to right is adopted (figure 2.1). The leading edges of the cylinders are drawn as grey rectangles on the right of each figure. To be consistent with the way PIV interrogation works between consecutive images, we plot velocity vectors with their midpoints located at the centers of the sampling areas (Adrian & Westerweel 2011). To avoid cluttering of the images, we do not show every vector available. The origin of the Cartesian coordinate system is located at the intersection of the leading edge of the pier with the bed. The orientation of the coordinate system is as follows (positive directions): x coincides with that of the approach flow, y is towards the free surface, and z points to the camera.

2.3.1 Time-averaged junction flow characteristics

We superimpose the time-averaged streamlines on non-dimensionalized velocity contour plots for each Re_D case in figure 2.2 (a-c). The junction region is home to two characteristic flow structures that manifest in the form of closed streamlines of a roughly elliptical or spiral pattern. We refer to the horseshoe vortex closer to the pier as HV1 (or primary) and the vortex further upstream as HV2 (or secondary). Their locations are not identical for every Re_D experiment. The core of HV1 is centered around (−0.14D, 0.04D), (−0.19D, 0.06D) and (−0.17D, 0.05D) respectively for the cases of LRe, MRe and HRe. The coordinates for the corresponding cores of HV2 are (−0.32, 0.01), (−0.36, 0.02) and (−0.29, 0.01). These results suggest that the spatial variability regarding the position of the cores is higher for the horizontal direction. Nevertheless, and in contrast to the findings of Agui & Andreopoulos (1992), they do not support a clear trend regarding the location of the vortices as we move from smaller to higher levels of Re_D. Differences with respect to the relative horizontal distances between HV1 and HV2 are also notable. These are 0.18D and 0.17D for LRe and MRe, but only 0.12D for HRe. The proximity between HV1 and HV2 for the latter case facilitates their interaction. Of importance are also the vertical distances between the cores of the two vortices, especially when combined with their relative sizes. The greater the vertical distance between HV1 and HV2 is, the more likely it is for incoming flow above HV2 to be deflected towards the wall upon encountering HV1. As we will show in the instantaneous analysis of the junction flows, this downward-deflected fluid plays an important role in the formation of a tertiary vortex and the overall vortex dynamics.

Streamline density indicates the level of organization (or coherence) of vortical structures. For every Re_D, HV1 consists of a larger number of streamlines compared to HV2. This observation alludes to the more prominent role of the primary vortex in the dynamics of junction flows. Motivated by this statement, we use streamline topology to examine the relationship between the two vortices and the return flow of fluid after it impinges on the cylinder's face. Figure 2.2 (a-c) reveals a different mechanism for each case. In particular, a comparison between the HV2 of LRe and MRe shows that the former receives a smaller number of streamlines (and thus less fluid mass) compared to the latter. In other words, the return flow is stronger for MRe, with both the primary and secondary vortices of this case benefiting from the influx of mass and momentum of fluid deflected on the obstacle's leading edge (figure 2.2b). The trend of increasing intensity of return flow with Re_D is valid for HRe too. Nevertheless, our data show that for this case streamlines of deflected fluid feed exclusively the primary vortex.

Focusing on the area between HV1 and HV2, the streamline topology does not suggest the presence of a tertiary vortex. This appears to contradict results from topological models inferred through flow visualizations (Baker 1979; Dargahi 1989; Simpson 2001). According to these studies, vorticity extracted from the wall below HV1 reorganizes to form a counterclockwise vortex at the saddle region between HV1 and HV2. We postulate that the absence of this flow pattern for the levels of Re_D investigated here stems from the highly unsteady behavior of the flow at the particular region. As we will elaborate on subsequent sections of the paper using animations of TRPIV data, the tertiary vortex undergoes various cycles of upliftings, eruptions and amalgamations with other vortices in a seemingly random fashion (refer to the work by Agui & Andreopoulos (1992) for descriptions of similar phenomena). This unsteadiness is filtered out, when time-averaged representations of the flow field are investigated.

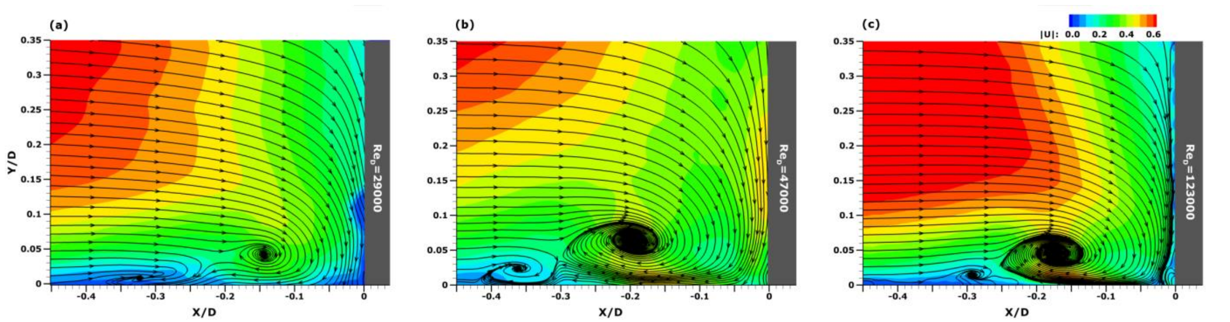

Figure 2.2-Spatial distribution of time-averaged streamlines and non-dimensionalized velocity magnitude, |U|. Two vortex cores, named as HV1 and HV2, appear regardless of Re_D.

Another notable topological characteristic is the absence of a corner vortex (CV) very close to the intersection of the wall with the cylinder. In the literature, the existence of such vortex is attributed to the separation of fluid running down the cylinder's face due to the adverse pressure gradient imposed by the wall. Here, curved streamlines for the MRe and HRe cases provide inconclusive evidence for the presence of CV in a time-averaged sense. Insufficient spatial resolution of our measurements or the increased uncertainty for the data close to solid boundaries could offer a plausible explanation for this discrepancy. A careful frame-by-frame inspection of the instantaneous flow fields though, rejects this conjecture. Corner vortices in the form of properly closed streamlines were observed for all Re_D cases. They emerged and disappeared in a seemingly random fashion. This intermittency, in conjunction with the relatively small velocities characterizing their cores, explains why corner vortices are not shown on the maps of figure 2.2 (a-c). The implication of this finding is that in the absence of a corner vortex, additional amounts of fluid vorticity escape the region at the very corner and join the return flow, which eventually merges with the main horseshoe vortex system.

Overall, our results for the time-averaged flow topology are in good agreement with those of past studies (Praisner & Smith 2006b; Paik *et al.* 2007; Kirkil & Constantinescu 2009; Sabatino & Smith 2009). The two-vortex model was verified for the studied Re_D levels, which differ by nearly an order of magnitude. The only inconsistency with some of the aforementioned works is with respect to the absence of the corner vortex.

Apart from the topological characteristics of the flow, figure 2.2 (a-c) provides insight on the spatial distribution of flow momentum. Generally, incoming flow enters the junction region at levels close to 60% of the bulk velocity and decelerates as it approaches the solid boundaries. An exception to flow retardation occurs within the region below HV1. There, velocities retain relatively high-momentum contents due to the strong near-wall jet of reversed flow (Devenport & Simpson 1990; Paik *et al.* 2007; Kirkil & Constantinescu 2009). Our measurements reveal that the increase in Re_D makes this feature more pronounced, as evidenced by the amplified velocity magnitudes. The physical mechanism underlying this increase relates to the spatial distribution of momentum in the junction. Namely, for the HRe case, fluid of higher momentum (visualized by red-colored bands) penetrates regions closer to the cylinder and the wall (figure 2.2c). Consequently, the momentum imparted on HV1 is pushing the vortex closer to the bottom. The proximity between the lower part of the vortex and the solid boundary eventually results in the contraction of streamlines comprising the near-wall jet of reversed flow. The outcome of this process is manifested in the form of increased flow velocities. In subsequent discussions about the time-averaged distribution of vorticity and the instantaneous flow fields, we will demonstrate that this feature has further implications for the flow physics dominated by vortex−wall interactions.

Next, we analyze the time-averaged velocity field into its streamwise and wall-normal components (figure 2.3a-c). This decomposition provides further details of the various flow features. For example, in all three maps two alternating regions of positive and negative wall-normal velocities (V/U_o) bound the left and right outer edges of HV1. The signs of the patterns depicted at these regions indicate the clockwise sense of rotating fluid. The exchange of momentum between them takes place through an elongated patch of negative streamwise velocities (U/U_o) located near the wall. All these characteristic flow patterns are absent for HV2, implying a pronounced difference between the behavior of HV1 and HV2. This difference is consistent for all Re_D cases. Furthermore, flooded contour maps of V/U_o more clearly display the existence of a strong downwash of fluid (or downflow) at the face of the cylinder for MRe. Both the origin of this feature and its effect on the time-averaged flow elude a straightforward interpretation.

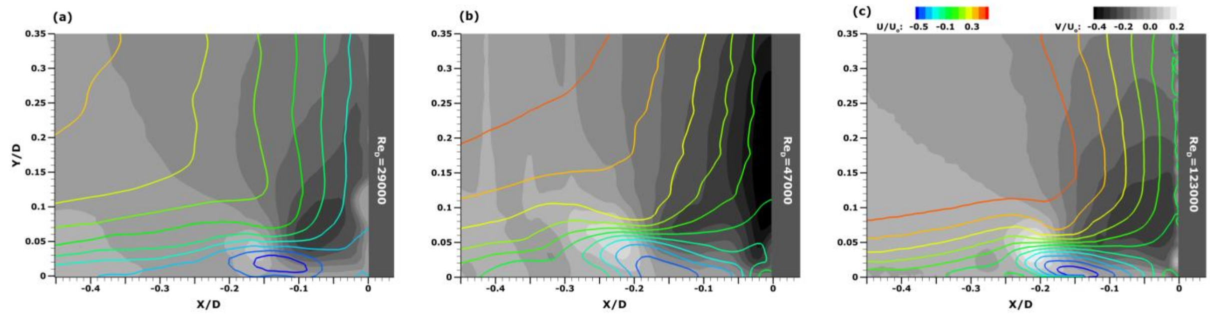

Figure 2.3-Contour lines of time-averaged streamwise velocity component superimposed on flood contour maps of time-averaged wall-normal component. Both parameters are non-dimensionalized with the approach velocity, U_o.

Out-of-plane (or spanwise) vorticity (ω_z) plays a central role in the interpretation of junction flows. Recall that the reorganization of vorticity within the separated boundary layer contributes to the generation of horseshoe vortices. Time-averaged maps (figure 2.4a-c) of this parameter attest to this statement. The color-coding of the maps was chosen to highlight only areas of significant positive (red) and negative (blue) values. Pockets of high negative vorticity overlap with the cores of the primary vortices. There is evidence for amplification of vortex-core vorticity as Re_D increases. On the other hand, the secondary eddies do not exhibit this feature. Their vortical content is an order of magnitude smaller than that of the primary vortices. Thus, it is difficult to distinguish between the vorticity of HV2 and incoming vorticity of the separated shear flow. Our measurements elucidate the spatial connections between these latter trails of incoming vorticity (pointed by the arrow on figure 2.4a) and the core of the primary vortex. This characteristic is particularly evident for the LRe and HRe cases (figures 2.4a, c). For MRe, such a connection is weakly supported (figure 2.4b). Instead, this case is characterized by another vertical patch of negative vorticity, which emanates from the downflow at the cylinder's face and merges with the core of HV1. This patch runs on top of a thinner and longer streak of positive vorticity. The latter is a common characteristic for every flow examined here. It expresses the vortical content of the downwash fluid propagating adjacent to the face of the cylinder. Note, however, that the magnitude of positive vorticity for this flow element becomes larger for higher levels of Re_D.

Another structure that calls for attention is the horizontal sheet of positive vorticity below HV1. This layer originates at −0.06D for LRe and −0.04D for both MRe and HRe. It extends respectively up to −0.20D, −0.25D and −0.24D. Its spatial extent shows that positive, near-wall vorticity is associated exclusively with HV1. The comparison of subplots in figure 2.4 (a-c) also shows that near-wall vorticity remains attached to the bed only for the LRe case. The trend of increasing vorticity as we move to higher levels of Re_D is verified here too. Positive vorticity eventually reaches levels comparable to the absolute value of those measured inside the core of HV1. Of interest is the relationship between the horizontal layer of positive vorticity below HV1 with the vertical layer of vorticity running down the leading edge of the cylinder. Figure 2.4 (a-c) does not support an unambiguous connection between these two structures (at least on a time-averaged sense). This argument indicates that the horizontal, near-wall layer of positive vorticity stems primarily from the interaction between the HV1 and the wall (Paik *et al.* 2007). Our data suggest that the interaction is stronger for HRe case. This finding concludes the previous discussion on the position of HV1 and the topology of its streamlines. In summary, we invoked here the physics of the flow to establish a link between the momentum and vortical contents of junction flows.

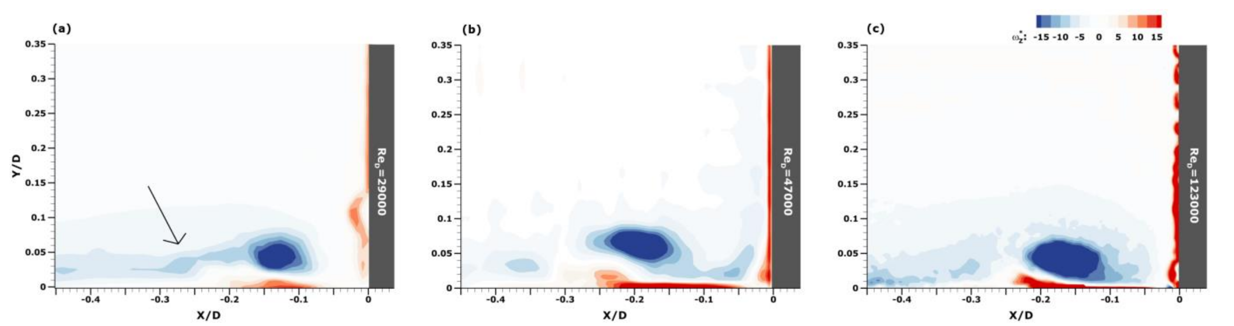

Figure 2.4-Maps of time-averaged spanwise vorticity for the various Re_D cases. Arrow indicates the trail of incoming vorticity. Vorticities are non-dimensionalized with t_c.

The non-dimensionalized turbulence kinetic energy (TKE) is calculated from the PIV data as: $= \frac{\overline{(u')^2} + \overline{(v')^2}}{2U_0^2}$, where u′ and v′ are the fluctuations of the streamwise and wall-normal velocity components. At the junction region, TKE approximately peaks within the cores of HV1 (figure 2.5). At these locations, TKE progressively grows to levels an order of magnitude higher than those characterizing surrounding flow. A nearly horizontal trail of TKE emanates from the line of flow separation (not shown in presented figures), lifts off the wall, and wraps around the periphery of HV1. Another vertical trail of TKE feeds HV1, but this happens only for the LRe and MRe cases. For the latter, increased TKE levels were measured at the very corner between the wall and the cylinder. Related to previous discussion, the implication here is that the corner vortex could exhibit high turbulence energies, despite its weak manifestation on a time-averaged sense.

Comparison of subplots in figure 2.5 (a-c) reveals an additional difference between the investigated flows. In particular, HRe case exhibits a second peak of high TKE closer to the wall (figure 2.5c). The distribution of TKE for MRe around HV1 is somewhat similar; yet the intensity near the bed is not high enough to generate a distinct secondary peak. This feature is absent from figure 2.5a. Two peaks of TKE have been reported in previous experimental (Devenport & Simpson 1990) and numerical studies (Paik *et al.* 2007; Kirkil & Constantinescu 2009; Escauriaza & Sotiropoulos 2011c). More specifically, Paik *et al.* (2007) were the first to establish a link between this second peak of TKE with the unsteady and bimodal behavior of HV1. Note, however, that there are also differences between our results and those of the aforementioned works regarding this feature. For example, we found that the second patch of increased TKE is inclined with respect to the wall, whereas in the referenced studies it develops parallel to the solid boundary. An additional discrepancy is with respect to the investigated levels of Re_D. Kirkil & Constantinescu (2009) calculated a double-peaked TKE structure for the flow around a cylinder at $Re_D=1.8\times10^4$. Escauriaza & Sotiropoulos (2011c) reported a C-shaped structure for DES simulations at $Re_D=3.9\times10^4$. Both of these Re_D levels are below our MRe case. Notwithstanding the limitations that obscure a straightforward comparison, this difference provides novel insight on the effects of Re_D on turbulent junction flows.

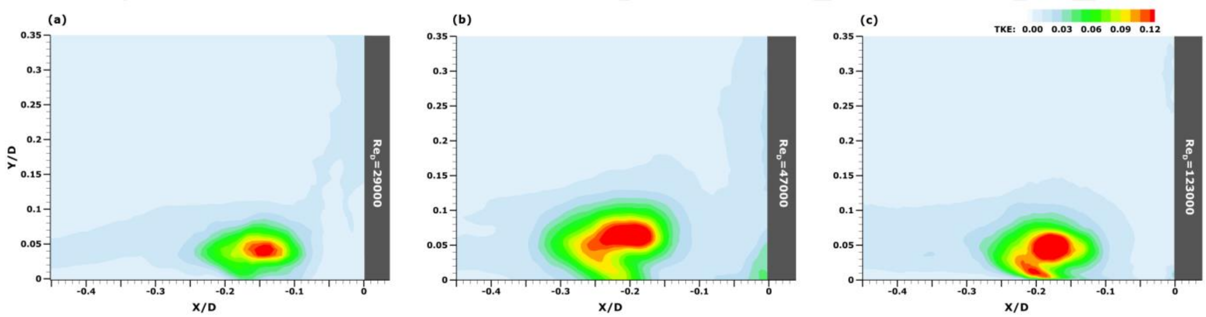

Figure 2.5-Non-dimensionalized turbulence kinetic energies (TKE). Subfigure (c) exhibits two characteristic peaks of TKE.

The analysis of the time-averaged characteristics of the junction flows under consideration concludes with the discussion about the levels of turbulence. Figure 2.6 (a-c) shows the spatial relationships between the streamwise and wall-normal turbulence intensities. A striking similarity for each Re_D cases is that u'/U_o and v'/U_o have nearly identical ranges. Consistent with previously presented results, the maximum concentration of turbulence intensity is located in the neighborhood of HV1. This is an additional testament to the degree of unsteadiness of the primary vortex. Higher levels of u'/U_o characterize HRe. For this case, streamwise turbulence intensity peaks at two locations: the core of the vortex and the region between the bottom periphery of the vortex and the bed. The shape of the HRe contours is similar to that of TKE (figure 2.5c). Interestingly, this analogy is not present at the other two cases. Although contour lines in figure 2.6 (a, b) support the existence of a double-peak structure (or even a triple-peak for LRe), this feature is absent in figure 2.5 (a, b). We conclude, therefore, that the relative contribution of the near-wall jet becomes more substantial at higher levels of Re_D. Finally, it was not possible to provide a meaningful connection between the region of reduced turbulence at the upper left corner of figure 2.6 (c) and the dynamics of the horseshoe vortex system.

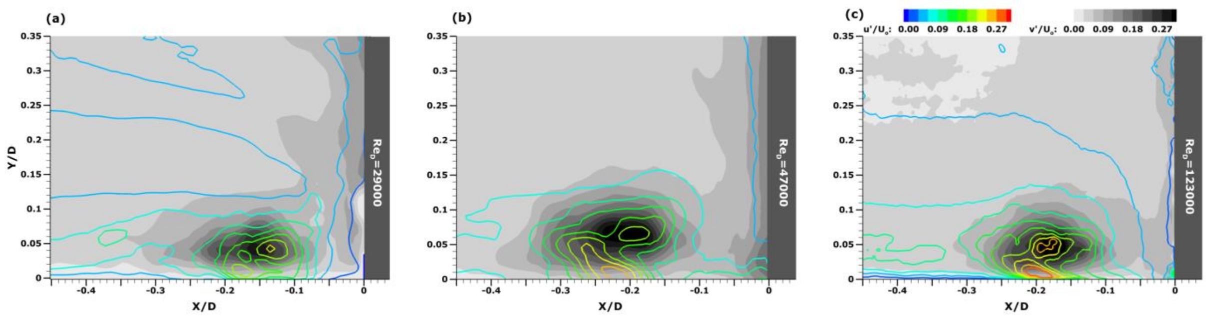

Figure 2.6-Contour lines of streamwise turbulence intensity, u'/U_o drawn on top of flood contour maps of wall-normal turbulence intensity, v'/U_o.

2.3.2 Time-resolved dynamics of junction flows

Particle Image Velocimetry allows for a global representation of the flow field at discrete time instants. We took advantage of this important feature and carried out a frame-by-frame analysis. A wealth of flow patterns was revealed. It is beyond the scope of this work to present a detailed appraisal of every instantaneous topology mapped on the measurement plane. Instead, we emphasize flow episodes that elucidate important aspects of the dynamic behavior of the horseshoe vortex for the various Re_D levels. We complement our discussion with sequences of characteristic snapshots. The analysis highlights important similarities and distinct differences that collectively portray the effects of Re_D on the turbulent flows at wall−cylinder junctions. Whenever possible, we compare our findings with those of past studies.

2.3.2.1 **Case of $Re_D=2.9\times10^4$ (LRe)**

The time-resolved analysis of flow dynamics for the LRe case revealed numerous flow patterns that were not detectable in the time-averaged velocity signals. High levels of intermittency characterize this junction flow, manifested in both large (organized vortices) and small-scale flow structures (near-wall fluid flow). For example, we discovered that the junction region is home to a number of vortices ranging from one to four (figure 2.7a, b). Vortex stretching and meandering increase the spatial extent of the orbits followed by the vortex cores. It is possible, therefore, that the secondary vortex (HV2) shown in the topology of figure 2.2 is just the average expression of a number of vortices, instead of an independent flow structure. More confidence exists in the expression of the primary vortex, although its presence on the flow field is not continuous.

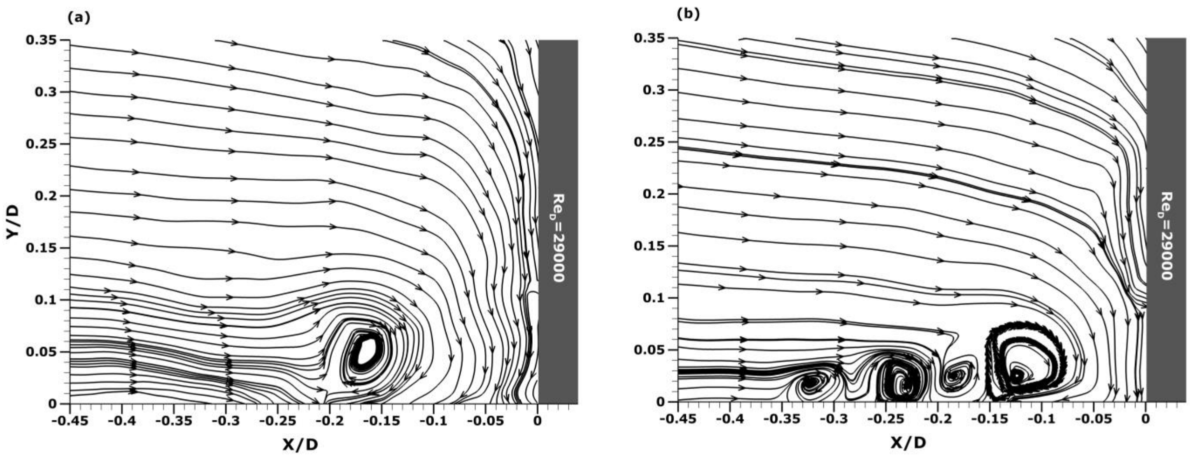

Figure 2.7-Characteristic instantaneous flow topologies for LRe case showing: (a) the minimum and (b) the maximum number of vortices.

The occasional disintegration of HV1 is a feature for which no hint was provided for by the time-averaged analysis. It was the frame-by-frame inspection of the flow field for the LRe case that revealed it. For a significant number of frames, the flow topology was devoid of the primary horseshoe vortex. These snapshots were clustered in thirteen groups. Their total duration was 440 ms, representing 13.5% of the LRe experiment. The disappearance of HV1 is interpreted as a loss of its coherence. Figure 2.8(a-d) shows that this state is preceded by the collision of HV1 with a fluid patch originating from the downwash flow parallel to the obstacle. This mechanism could offer a plausible explanation for the obliteration of HV1, because it was identified in the majority of the episodes (eight out of thirteen). The absence of this or another possible mechanism (Paik *et al.* 2007) for the remaining five episodes, however, casts doubts on the generality of that conclusion. Regardless of the origin of the phenomenon, the unsteadiness in the region formerly occupied by the core of HV1 is substantial (figure 2.8c). The flow dynamics locally appear to assume an erratic behavior with changes in topology occurring even faster than the sampling rate of 1,000 Hz. This also prohibits drawing sound conclusions about what brings about the end of the unsteadiness and re-stabilizes the flow, which then returns to more easily identifiable patterns (figure 2.8d).

Note that during the absence of HV1, the secondary vortex retains its coherence and relative position within the flow topology.

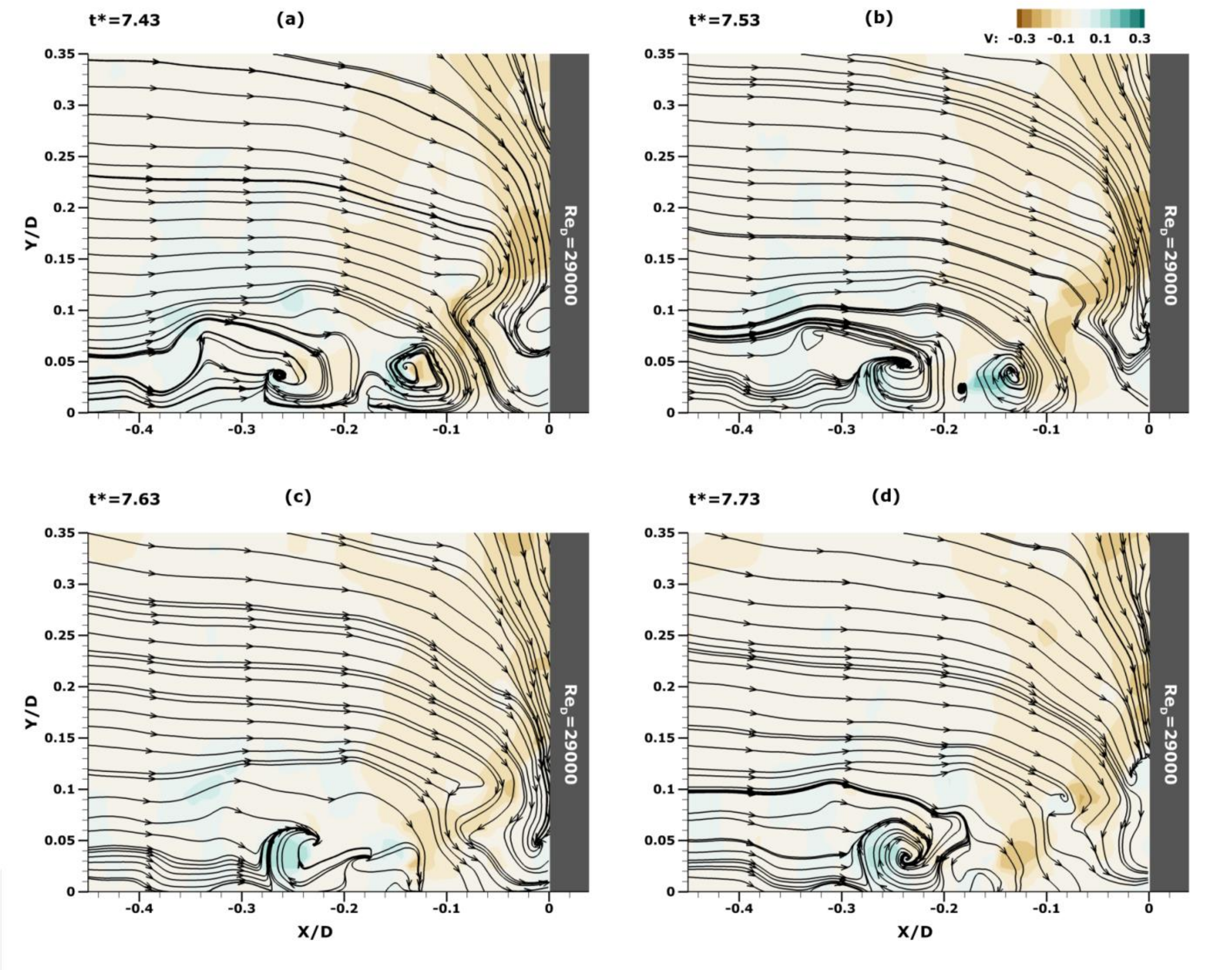

Figure 2.8-Sequence of snapshots displaying the disintegration of HV1 for the LRe case. Flood contour maps express the magnitude of the wall-normal velocity component. Dimensionless time is indicated with t*.

The discussion on the dynamics of the primary horseshoe vortex is extended to include interactions with HV2. In the absence of the tertiary vortex, there is a direct interplay between HV1 and HV2. Figure 2.9 (a-d) demonstrates a sequence of snapshots describing an episode that ends up with the amalgamation of the vortices. In the beginning, (figure 2.9a) the two cores are close together. In a subsequent frame (figure 2.9b), the two structures share a number of common streamlines at the lower edges of their peripheries. The interaction becomes closer, so that both cores are surrounded by the same outer streamlines (figure 2.9c). Note also the appearance of a new, transient structure near the cylinder. Finally, the two vortices merge into a single, large-scale structure (figure 2.9d).

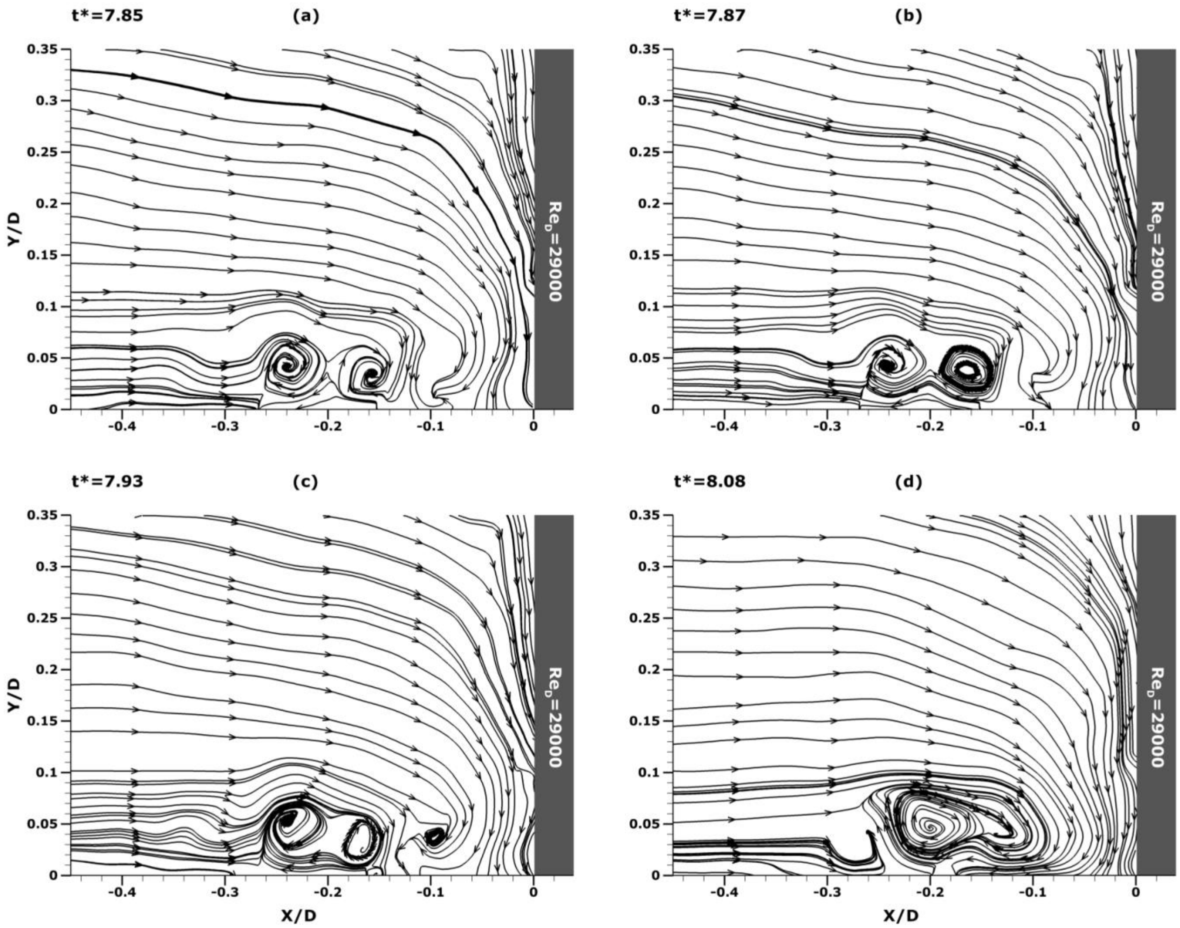

Figure 2.9-Amalgamation of HV1 with HV2.

Based on the prominent role that the bimodal dynamics of the horseshoe vortex play in the junction flow literature (Devenport & Simpson 1990; Paik *et al.* 2007; Kirkil & Constantinescu 2009), we revisit this subject within the scope of Reynolds number effects. Instantaneous representations of the global velocity field simplify flow classification. Thus, there is no need to resort to indirect methodologies (like the one devised by Devenport & Simpson (1990) for data collected with point-wise velocity measuring techniques) to determine the characteristic modes and the time spent by the flow in each one of them. A painstaking examination of the cinematography of the PIV data suffices for a direct and unambiguous detection of these modes.

An important finding of this analysis is that zeroflow and backflow are not the only modes that characterize junction flows. For a significant number of frames, the characteristics of the flow field do not verify the topologies of any of these two well-known modes. Figure 2.10 (a-c) juxtaposes three snapshots representative of the backflow, the zeroflow, and this other mode, which we will refer to from now on as *intermediate*. The backflow mode is characterized by a strong near-wall jet, which moves against the direction of the bulk flow (figure 2.10c). On the other hand, zeroflow mode occurs when the motion of the jet is impeded (figure 2.10a). The reverse flow is then directed upwards at high velocities. These descriptions are in good agreement with the original definitions provided by Devenport & Simpson (1990) and have been corroborated by subsequent studies (Paik *et al.* 2007; Kirkil & Constantinescu 2009; Gand *et al.* 2010). Differences also emerge through this comparison. The most striking of them is that, in contrast to what has been suggested in the literature, the flow modes do not have preferential locations within the flow domain. For example, in figure 2.10(c) one would have expected the appearance of zeroflow, because the primary horseshoe vortex is located very close to the cylinder. Nevertheless, the backflow mode is present. As far as the intermediate mode is concerned, it collectively symbolizes every flow topology that does not fall into one of the well-known categories. Although there are various expressions of the intermediate mode, figure 2.10(b) is representative of a typical one. It is observed that the interface between the incoming and return flow does not form a vertical line. The rather weak return flow separates from the bed and is directed upwards, but is lacking the momentum required to propagate further upstream. Its path terminates upon its encountering with the incoming flow. Unlike the zeroflow mode, the incoming flow here is not strong enough to cause the vertical ejection of fluid at high velocities. Essentially, the momentum of the return flow is diffused within its surroundings. Previous studies have mentioned the possibility of existence for additional junction flows modes, but did not elaborate further on the subject (Devenport & Simpson 1990; Praisner & Smith 2006a). The intermediate mode indicates that the switching between the two modes is not continuous. This could possibly suggest modifications in the nature of phenomena that have been linked to the mode-switching mechanism (Agui & Andreopoulos 1992; Olcmen & Simpson 1994; Praisner *et al.* 1997; Kirkil &

Constantinescu 2009; Escauriaza & Sotiropoulos 2011b; Escauriaza & Sotiropoulos 2011a).

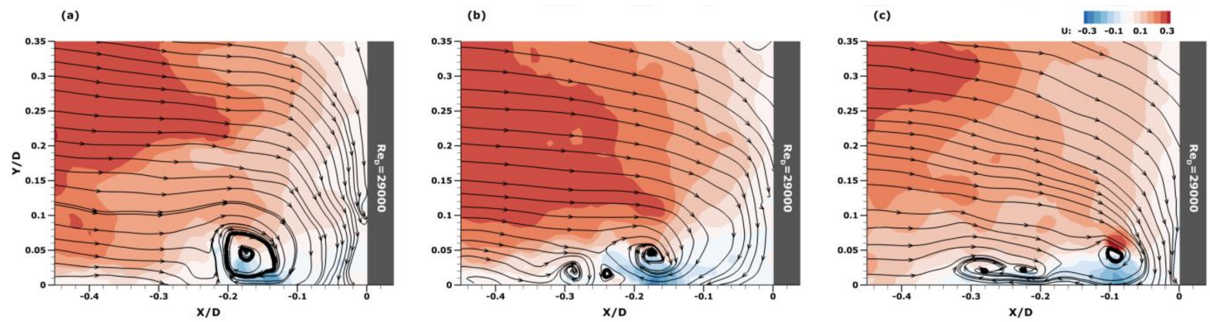

Figure 2.10-Characteristic junction flow modes: (a) zeroflow, (b) intermediate, and (c) backflow. Flood contours plot the magnitude of the streamwise velocity component.

The sequence of the three modes appears to be random. Zeroflow mode is present 41.5% of time. The intermediate mode follows with 33.8%. Backflow mode occurs only during 11.2% of the total duration of the LRe case. As mentioned previously, for 13.5% of the time the disorganization of the primary vortex does not allow classification to any of the above flow modes. The average frequencies of appearance, made dimensionless multiplied with t_c are as follows: 0.86 for the zeroflow mode, 1.12 for the intermediate, and 0.52 for the zeroflow mode. The latter mode is the most short-lived and the one that appears less frequently during the LRe case.

2.3.2.2 **Case of Re_D=4.7×10^4 (MRe)**

A characteristic snapshot of the instantaneous flow topology for the MRe case is presented in figure 2.11. A thorough inspection of the cinematography revealed that the maximum number of vortices appearing simultaneously on a snapshot was five and the minimum was one (just the primary vortex). Throughout this experiment, HV1 dominated the flow field. In general, the topologies of the MRe case were well-defined and bore many similarities to topological models representing time-averaged flows. Observe for example the characteristic sequence of vortices in figure 2.11. The symmetrical configuration comprises two pairs of clockwise−counter-clockwise vortices: HV1 with HV3 and HV2 with HV4. Most of these topologies, however, cannot be sustained for a substantial amount of time. Momentum and vorticity fluctuations in the incoming boundary layer or interactions between the vortices drive the flow into more stable topologies.

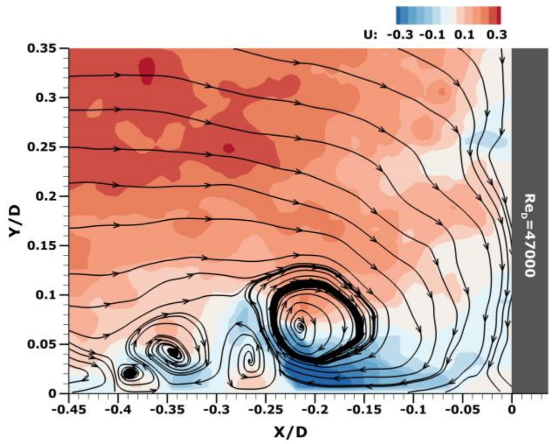

Figure 2.11-Instantaneous flow topology for MRe case demonstrating the simultaneous presence of four vortical structures. Flow streamlines are superimposed on flood contours of the magnitude of the streamwise velocity component.

We then shift the focus to the study of the downflow that was shown (figure 2.2 and figure 2.3) to be a notable feature of the MRe case. Video animations (figure 2.12 a-c) revealed that patches of negative vorticity run down the face of the cylinder in a nearly uninterrupted fashion. They are advected on top of the continuous layer of positive vorticity that emerges very close to the cylinder's face as a result of fluid–structure interactions. Occasionally, two counter-rotating blobs of vorticity emerge and run side-by-side downwards (figure 2.12a). These structures do not have a single origin: some of them had previously traveled with the incoming boundary layer flow, others entered through the upper part of field of view, and finally, a third category formed right at the cylinder's face when horizontal flow impinged on the obstacle. Once fluid parcels of negative vorticity approach the bed, they join the return flow directed upstream (figure 2.12c). This change of direction is accompanied with the generation of positive vorticity very close to the wall. From this point on, the positive patch of vorticity moves in parallel to the negative patch of vorticity and towards the upstream. Eventually, they merge with the core of HV1 (negative vorticity) and the elongated patch of positive vorticity below HV1, strengthening the rotationality of these flow features. This demonstrates that the eruptions of near-wall fluid do not originate exclusively from the interaction between

HV1 and the wall. Some of them are simply high-vorticity fluid masses making their way towards HV1 through the jet of return flow.

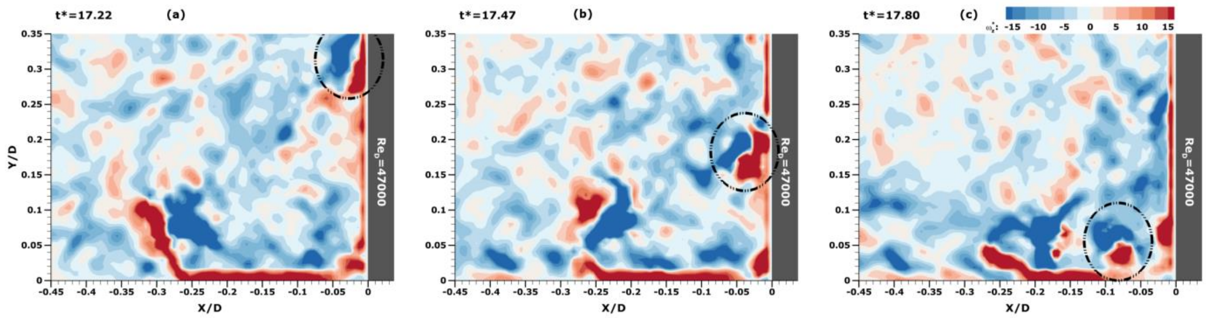

Figure 2.12-Sequence of frames illustrating the transport of two patches of opposite spanwise vorticity within the junction.

The dynamics of the tertiary vortex can be more clearly tracked within the cinematography of the MRe case. As shown in figure 2.13(a), the tertiary vortex originates from two sources: the approach boundary layer and the return flow of fluid that had previously impinged on the cylinder. In agreement with findings from the time-averaged analysis, the relevant positions of HV1 and HV2 also play a role in the formation of HV3. The dynamic interplay of these flow structures determines the location of the tertiary vortex in time. In particular, in figure 2.13(b), HV3 is stretched and acts as a barrier separating the primary vortex and the reverse flow jet from the incoming flow. The tertiary vortex also traps the positive vorticity that is transported with the reverse flow jet (figure 2.13c). This modifies the wall-eruption mechanism (Paik *et al.* 2007), resulting in weaker extractions of near-wall fluid compared to those observed for the HRe case. Nevertheless, occasionally these events can bring about the disintegration of the tertiary vortex within the MRe experiment (figure 2.13d).

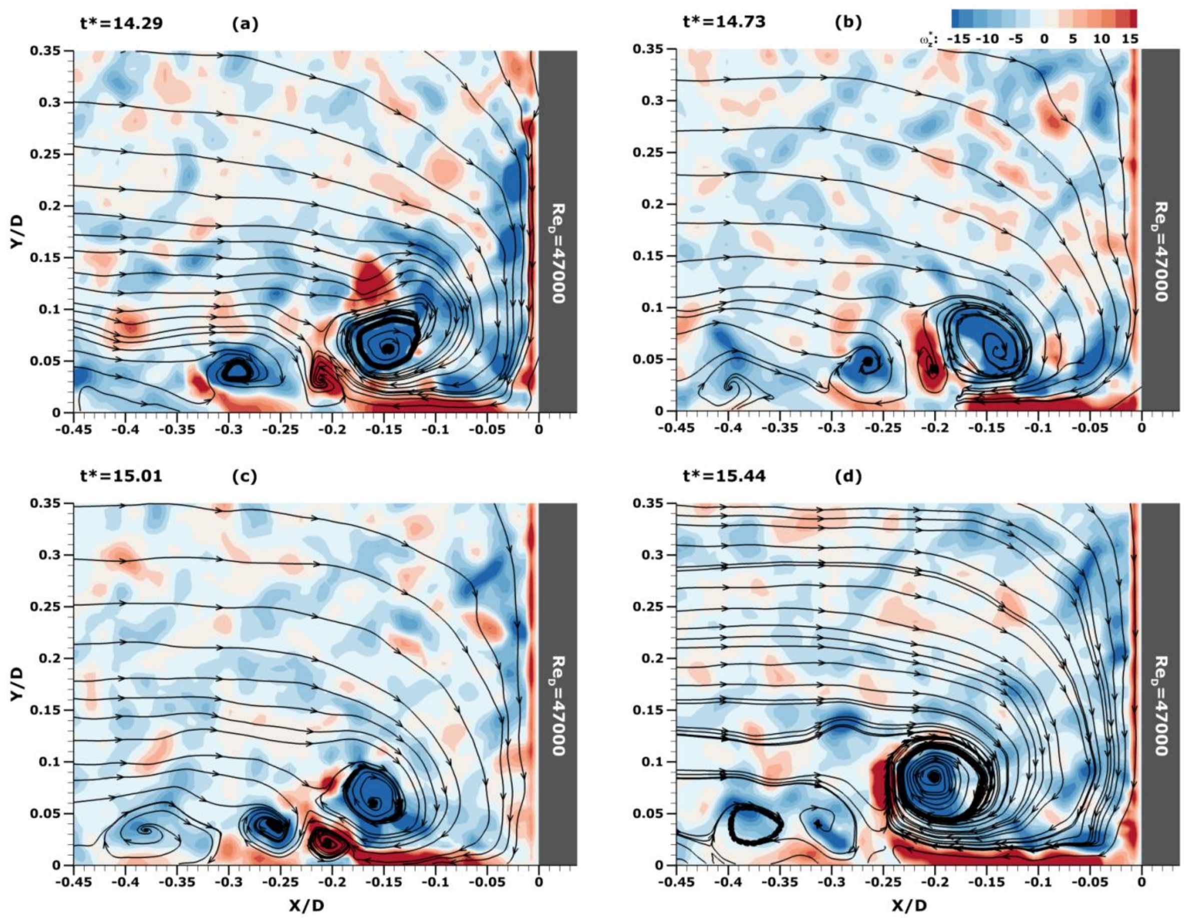

Figure 2.13-Dynamics of tertiary horseshoe vortex (HV3). The background displays the instantaneous magnitude of out-of-plane vorticity.

This sub-subsection concludes with information regarding the characteristic flow modes. Time-wise, they are nearly equivalent for the MRe case. In particular, the percentages of time for which the zeroflow, the intermediate, and the backflow modes appear on the instantaneous flow snapshots are respectively: 31.7%, 36.1%, and 32.3%. The dimensionless frequencies of appearance reveal a slightly different picture and measure: 0.91 for the zeroflow, 0.96 for the intermediate, and 0.72 for the backflow mode. Here, the intermediate mode is the one appearing more frequently and for a longer duration compared to the other two modes.

2.3.2.3 **Case of Re_D=12.3×10^4 (HRe)**

Video animations revealed qualitative similarities between the instantaneous topologies of the HRe and the other two Re_D cases. The number of vortices with properly closed streamlines that were identified simultaneously on each snapshot ranges between one and five (figure 2.14b). The primary vortex was present in all frames, in agreement with the results reported by Agui & Andreopoulos (1992) for a flow with Re_D=10×10^4. Except for the well-defined topologies mentioned previously, however, smaller vortical structures appear intermittently on the flow field (figure 14a). Their manifestations in a coherent form are particularly short-lived. Due to their fleeting nature, it is not possible to draw concrete conclusions about their origin or their final destination. Occasionally they appear to merge with larger vortices to increase their coherence. In other instances, their abrupt disappearance from the imaged flow plane could be attributed to the action of cross-stream pressure gradients. The concentration of vorticity within the non-coherent flow structures is very low. This fact, in conjunction with their relatively low momentum, could possibly explain why these structures are vulnerable to lateral pressure gradients and vanish from the field of view. In any case, these transient flow patterns seem to uniquely characterize the HRe experiment.

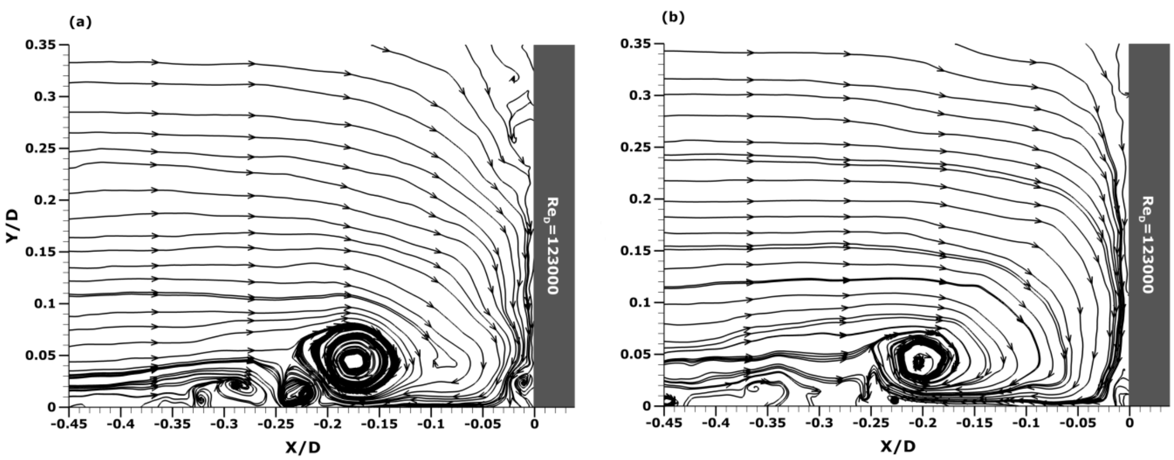

Figure 2.14-(a) Instantaneous flow topology with five vortices and (b) expression of non-coherent flow structures.

Another feature identified exclusively in the cinematography of this experiment refers to the primary vortex. In three flow episodes, an unusually rapid upstream motion of HV1, away from the cylinder, was observed. This feature originated from a mechanism common in every episode: an influx of momentum from the boundary layer feeding HV1 directly (figure 2.15a). The incoming fluid patch is trapped within the left and upper periphery of the vortex. In contrast to multiple other similar interactions between boundary layer flow and HV1, the decisive parameter here is the combination of high-momentum and low-vorticity of the patch. The vortex engulfs this fluid parcel, but fails to impart rotational motion on it. The parcel completes half a revolution within the vortex core until its direction of motion is reversed (figure 2.15b). From that point on, the linear momentum of the fluid patch is superimposed on the rotational motion of the vortex. The composite flow structure is advected rapidly to the upstream, riding on top of the near-wall jet of reverse flow (figure 2.15c). This migration is eventually impeded either by the emergence of a tertiary vortex at the left toe of HV1, or by the collision with incoming flow (figure 2.15d). In both cases, the momentum of the vortex is dissipated and flow topology assumes again a more conventional expression. Throughout this episode, the large velocity gradients developing close to the wall change rapidly in space and time. In total, all three episodes characterized by the swift motion of HV1 to the upstream, lasted for 322 ms with a frequency of appearance equal to 0.92 Hz.

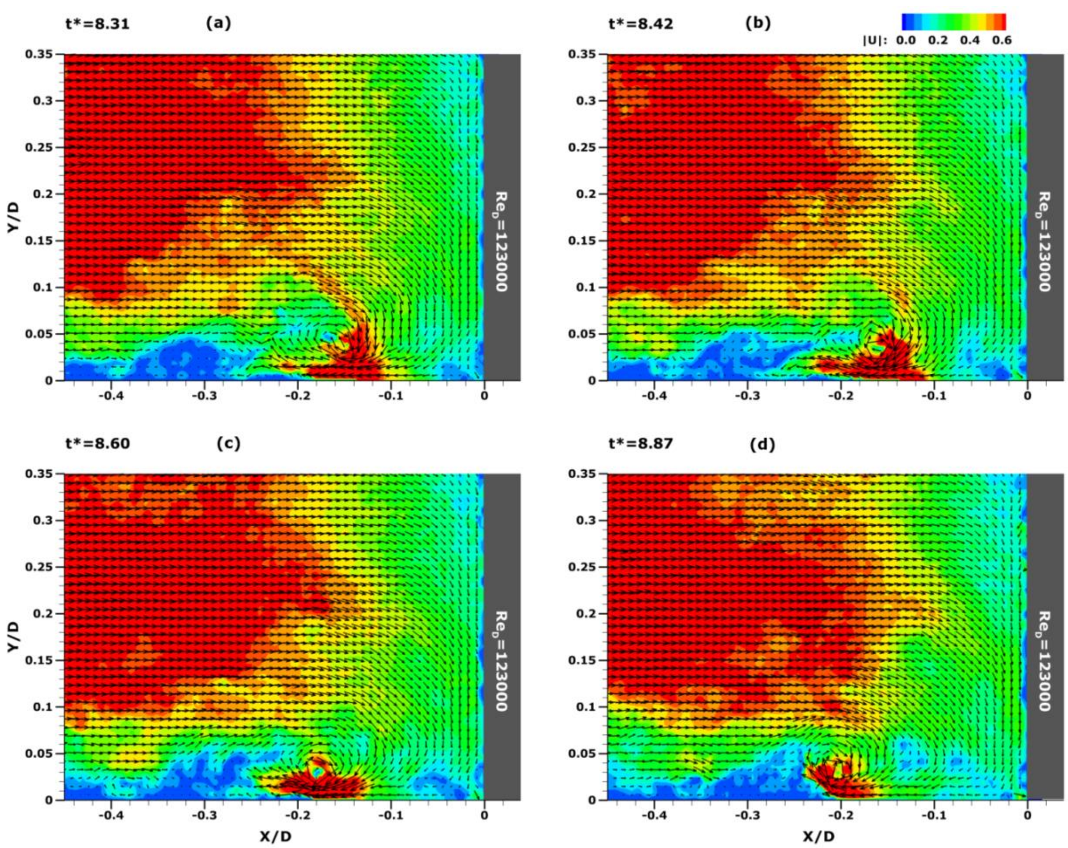

Figure 2.15-Episode of rapid advection of the primary vortex to the upstream. Contour maps are flooded with the non-dimensionalized velocity magnitude, |U|.

Additional interactions of the horseshoe vortex system with other flow components and the wall also constitute integral parts of the junction flow mechanism for HRe. In general, many of the characteristics that were described in previous cases (LRe, MRe) apply here too and need not to be repeated. An important difference, however, is noticed with respect to the elevated levels of momentum that characterize the horizontal boundary layer flow. Large-scale pulses of high velocity penetrate deeper into the flow stagnation region (figure 2.16a). They get very close to the face of the cylinder; however, (and unlike what was reported for the MRe case) they cannot establish a downward jet of high momentum. These flow elements energize the general downwash flow, the reverse near-wall jet, and occasionally the primary vortex (as described previously). A stronger return flow, which at most times assumes velocities as high as $0.6U_o$, signals the transition to the backflow mode (figure 2.16b). This becomes possible only when the incoming near-wall flow gets weaker due to a reduction of its momentum. It is therefore demonstrated that fluctuations in momentum of the incoming boundary layer indeed influence the switching of the flow between its modes (Devenport & Simpson 1990).

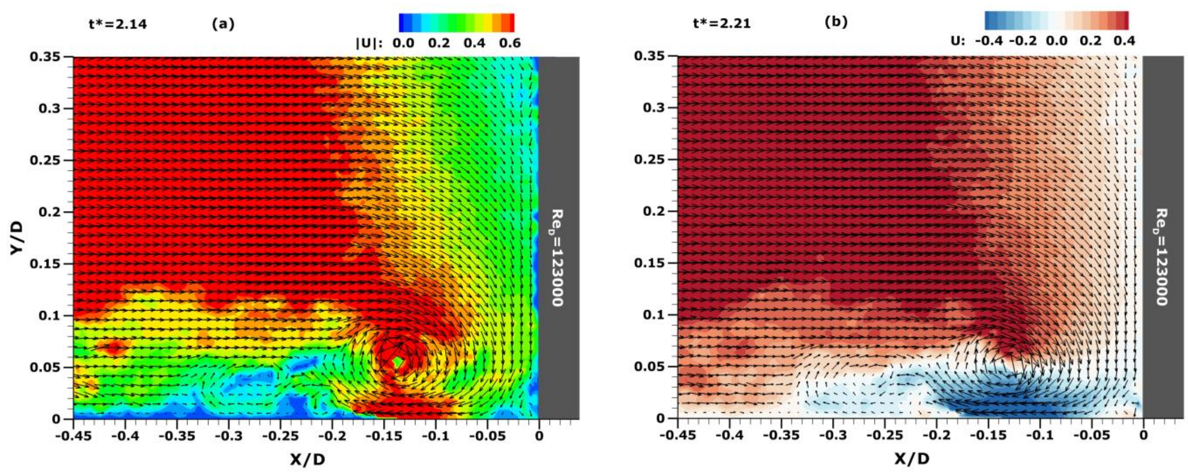

Figure 2.16-(a) Pulse of high-momentum approaching the face of the cylinder and (b) backflow mode. Contour maps are flooded with (a) the non-dimensionalized velocity magnitude, |U| and (b) the streamwise velocity component.

In addition to high momentum, the return flow for the HRe case is rich in vorticity. The presence of the layer of positive vorticity (evident in figure 2.4c) is continuous.

Regardless of the flow mode, this feature is displayed in every snapshot of the flow cinematography. Video animations also reveal that the return flow is fed with positive vorticity emanating from the interaction of the downwash flow with the cylinder. The connection between these two flow structures is intermittent and this explains why it is not manifested in the time-averaged results (figure 2.4c). Another feature that is brought to prominence through time-resolved analysis is the vortical content of the approaching boundary layer. Multiple patches of vorticity comprise the incoming flow. Negative vorticity dominates the separated flow close to the wall and feeds HV1 and HV2. On the contrary, the content of the mid and upper parts of the flow domain is mixed. Negative and positive vorticity clusters alternate in a seemingly random manner. The opposite signs cancel out when a time-averaging operator is applied. The resulting flow appears to be nearly irrotational (figure 2.4). Nevertheless, as demonstrated here (figure 2.17 a-d), this can be misleading. Not only is there a significant vorticity influx with the incoming flow, but also a portion of this vorticity merges with the horseshoe vortex and the return flow. Collectively, the increased momentum and vorticity levels justify the elevated intensity of eruptions of near-wall fluid (figure 2.17 a-d) observed exclusively for this HRe experiment. The sequence of snapshots in figure 2.17 (a-d) describes the ejection of near-wall vorticity that occurs simultaneously with the disintegration of the pre-existing HV3. As the bottom of the primary vortex approaches the wall, it displaces fluid masses of lower momentum (figure 2.17a). HV3 blocks the horizontal motion of the displaced fluid and directs it upwards at an angle with the wall. This forms a jet characterized by high momentum, which was imparted by the horseshoe vortex and possibly augmented by an instantaneous increment in the velocity of the return flow(figure 2.17b). The violent collision of this jet with HV3 causes the disintegration of the latter (figure 2.17c). Remnants of the coherent vorticity of the tertiary vortex in the form of small packets are trapped in the rotational motion of the primary vortex. Some of them are diffused within the surrounding flow. The rest make it through a full revolution and join again the horizontal layer of positive vorticity that characterizes the return flow (figure 2.17d). The whole process repeats again at irregular time intervals.

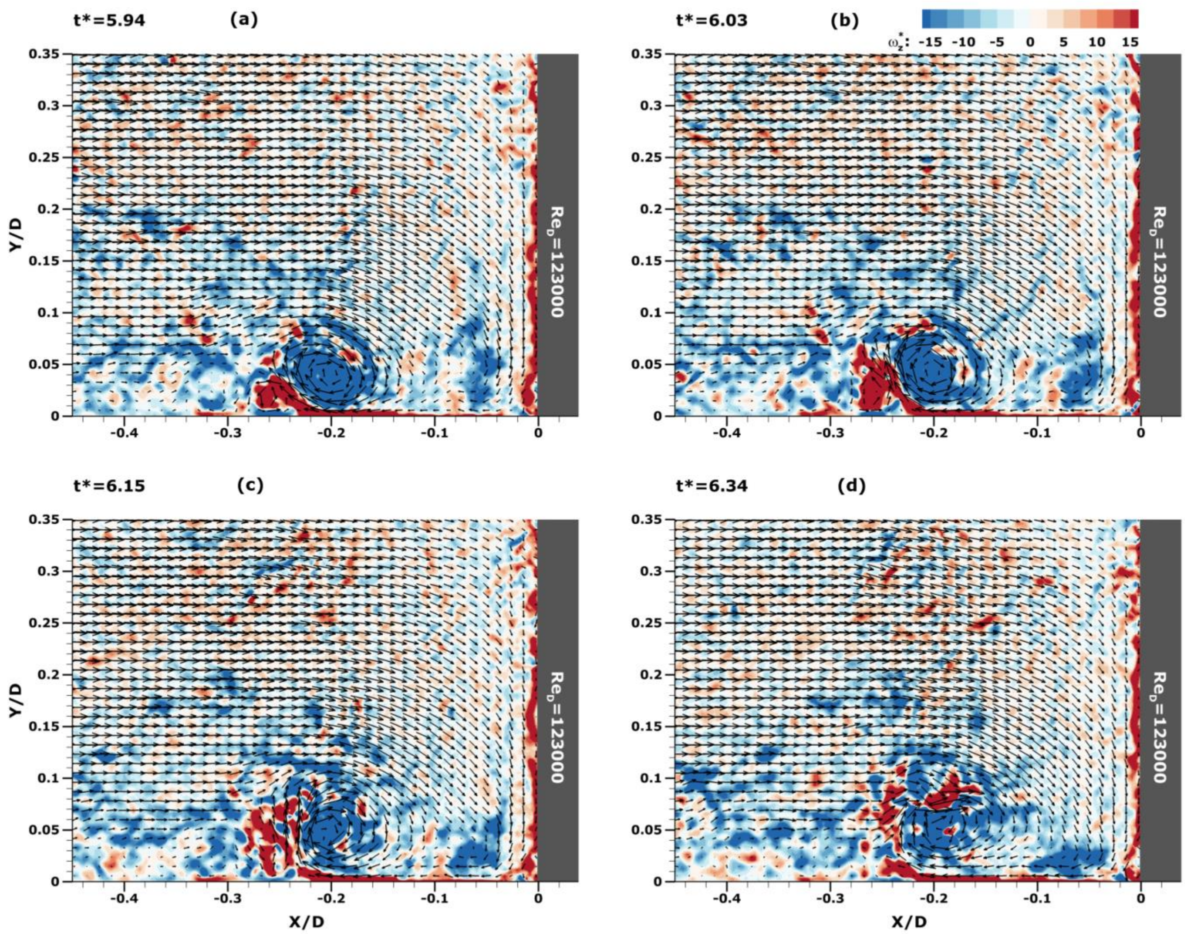

Figure 2.17-Sequence of snapshots illustrating the eruptions of near-wall fluid for the HRe case. Flood contour maps express the magnitude of the out-of-plane vorticity, ω_Z.

Finally, we refer to the statistics describing the modal dynamics of the junction flow for the HRe case. Again, all three modes mentioned in the analysis of the LRe and MRe cases are present here too. Quantitatively, the HRe case is at zeroflow mode 31.3% of time. The percentage for the intermediate mode is 39.6% and for the backflow mode is 19.3%. For the remaining 9.8% of time, episodes characterized by the rapid motion of the primary vortex to the upstream dominate flow dynamics. The calculation of the average dimensionless frequencies yielded the following results: 0.69 for zeroflow, 0.77 for intermediate, and 0.40 for backflow mode. The frequencies observed at this high level of Reynolds number are lower than those recorded for the other two experiments. Furthermore, and in agreement with the MRe case, the intermediate flow mode is the prevalent one here.

2.3.3 Statistical investigation of flow unsteadiness

2.3.3.1 **Spatial and temporal dynamics of primary horseshoe vortex**

Two-dimensional probability density functions of the location of the primary horseshoe vortex complement the understanding of the complex dynamics of junction flows. They provide a concise way to map the topology of this major flow pattern simultaneously in time and space. The exact position of the vortex core is identified using the so-called Q-criterion (Hunt, Wray & Moin 1988). The quantity Q is defined as: $Q = \frac{1}{2}(\boldsymbol{\Omega}^2 - \boldsymbol{S}^2)$, where **Ω** is the rate of rotation and **S** is the rate of flow strain. When Q assumes positive values, rotation dominates. The higher the value of Q at specific locations of the flow field, the more confidence there is for the appearance of a coherent vortical structure at these locations. Here, we assume that the position of the primary horseshoe vortex coincides with that of maxQ for every flow snapshot (we excluded from this calculation instants for the LRe case where HV1 was not present). This assumption was tested for numerous instantaneous flow fields against an alternative methodology. The latter used minimum vorticity and streamline curvature to identify the position of HV1 core. Compared results were in good agreement and validated the initial assumption.

The outcomes of the Q-criterion analysis are mapped on the two-dimensional flow domains for each Re_D case in figure 2.18 (a-c). Regardless of Re_D, the orbits of the HV1 core form shapes with roughly elliptical outlines. The horizontal extents of these topologies are 0.15D for LRe, 0.17D for MRe, and 0.14D for HRe. The corresponding vertical extents are 0.07D, 0.06D, and 0.06D. Therefore, the horizontal amplitude of wandering is higher for the MRe case and the vertical one is higher for the LRe case. Differences were identified with respect to the magnitude of the probability density functions (p.d.f.s) for each case. It is reminded that p.d.f.s are indirect indicators of the amount of time that HV1 spent at each location throughout the duration of each experiment. In particular, the most probable locations for the center of the primary vortex cover a continuous region for the LRe case (figure 2.18a). The shape of the region approximates an ellipse with a major axis of 0.09D and a minor axis equal to 0.03D. For the MRe case the position of HV1 at most times falls within a smaller region that consists of two peaks (prominent locations). Both peaks have a common ordinate of 0.05D. The distances between each of them and the leading edge of the cylinder are 0.21D and 0.18D. On the other hand, figure 2.18(c) corresponding to the HRe case shows multiple locations with high values of p.d.f.s regarding the position of HV1.

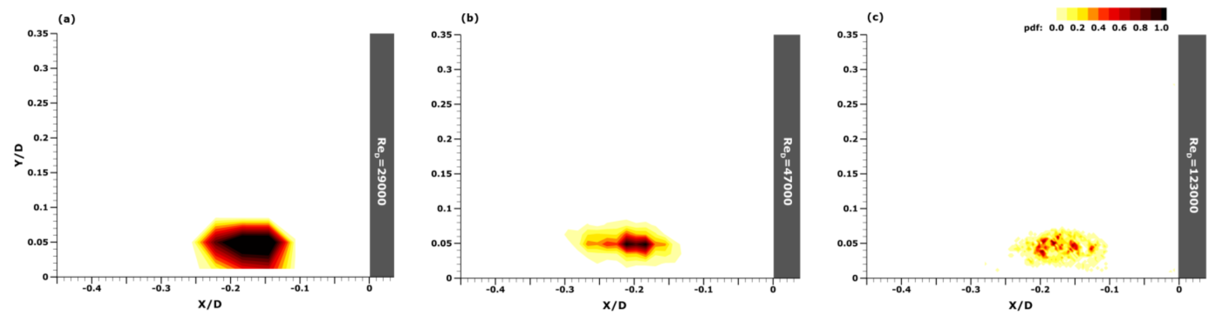

Figure 2.18-Maps of probability density functions for the location of the core of HV1 based on the Q-criterion for the identification of the vortex core.

A comparison between the results discussed in this section and those reported in past studies provides additional perspective regarding the unsteady behaviour of HV1. Agui & Andreopoulos (1992) using flow visualizations and wall-pressure measurements, argued that the amplitude of wandering of the primary vortex scales with the thickness of the incoming boundary layer. Although not stated explicitly, it is likely that they referred to wandering that occurred exclusively along the horizontal direction. Our data do not support this statement. The amplitudes of horizontal wandering (0.15D for LRe, 0.17D for MRe, and 0.14D for HRe) differ significantly from the boundary layer thicknesses, which were respectively 0.90D, 0.86D, and 0.52D. A somewhat better agreement was found between the amplitude of wandering along the wall-normal direction (0.07D for LRe, 0.06D for MRe, and 0.06D for HRe) and the displacement thickness of the boundary layer for each case measured 0.07D, 0.09D, and 0.04D. Nevertheless, the discrepancies with respect to the MRe and HRe cases still preclude the deduction of a more general conclusion on this subject. In another study, Sabatino & Smith (2009) published a map of p.d.f.s for the location of the primary vortex measured for a junction flow of $Re_D=1.9\times10^4$. The comparison with results from our LRe case with $Re_D=2.9\times10^4$ reveals strong similarities regarding the spatial extent of the two topologies. Both studies map a nearly identical region within which the core of the primary vortex wanders. Nevertheless, Sabatino & Smith (2009) highlighted the existence of two prominent positions for the location of vortex (instead of a single continuous region reported here). This discrepancy is likely due to the different numerical levels that were selected to plot the p.d.f. contours.

2.3.3.2 **Bimodality of velocity probability density functions**

Probability density functions of flow velocities have been widely used as a rigorous means to establish the bimodal dynamics of the horseshoe vortex system (Paik *et al.* 2007; Kirkil & Constantinescu 2009). Here, we follow the methodology introduced by Devenport & Simpson (1990). Namely, we plot probability density functions of velocity fluctuations non-dimensionalized by their root mean square value. The position of zero instantaneous velocity is marked on the horizontal axis with an asterisk. Without this important detail, it is not possible to establish meaningful links between the p.d.f.s peaks and the modes of interest (zeroflow, backflow, and intermediate flow). Figure 2.19 (a-d) provides additional insight on this statement. In particular, both subfigures (a) and (b) display probability density functions of streamwise velocity fluctuations with two distinct peaks. Nevertheless, only (a) manifests the zeroflow and backflow modes that characterize the behavior of the primary horseshoe vortex. There, the first peak centers approximately on zero instantaneous velocity as marked on the figure by the asterisk. The second is located at a region where instantaneous velocities are negative, which indicates consistency with backflow mode. On the contrary, the two peaks shown on subplot (b) are both in regions of positive instantaneous velocities. Whereas the behavior of flow at this location is also bimodal, the bimodality is not to be interpreted as a manifestation of the zeroflow−backflow phenomenon. Similar findings are reported from the statistical analysis of the instantaneous wall-normal velocity signals. The typical behavior of the zeroflow−backflow mode mechanism is evidenced in plots with characteristics similar to figure 2.19(c). When backflow mode is on, the reverse flow jet is nearly parallel to the bed, so the wall-normal velocities are close to zero (left peak). Once zeroflow mode kicks in, wall-normal velocities assume positive values and result in another peak emerging on the right of the first one. In contrast, figure 2.19(d) displays a double-peak structure with both peaks located at areas of negative wall-normal velocities. Again, these two peaks are not linked to the bimodal dynamics of the primary vortex, at least not in a way similar to that described by Devenport & Simpson (1990). As far as the intermediate flow mode is concerned, it is not straightforward to determine its expression on the p.d.f. plots. It could be postulated that it corresponds to those parts of the graph not belonging to the peaks. Alternatively, the intermediate mode may be prevalent at locations where the p.d.f.s do not exhibit prominent peaks. In any case, subsequent analysis will focus on the dynamics of the two extreme modes (zeroflow, backflow) that have been shown to significantly affect junction flow-related phenomena (Agui & Andreopoulos 1992; Olcmen & Simpson 1994; Praisner *et al.* 1997; Kirkil & Constantinescu 2009; Escauriaza & Sotiropoulos 2011b; Escauriaza & Sotiropoulos 2011a).

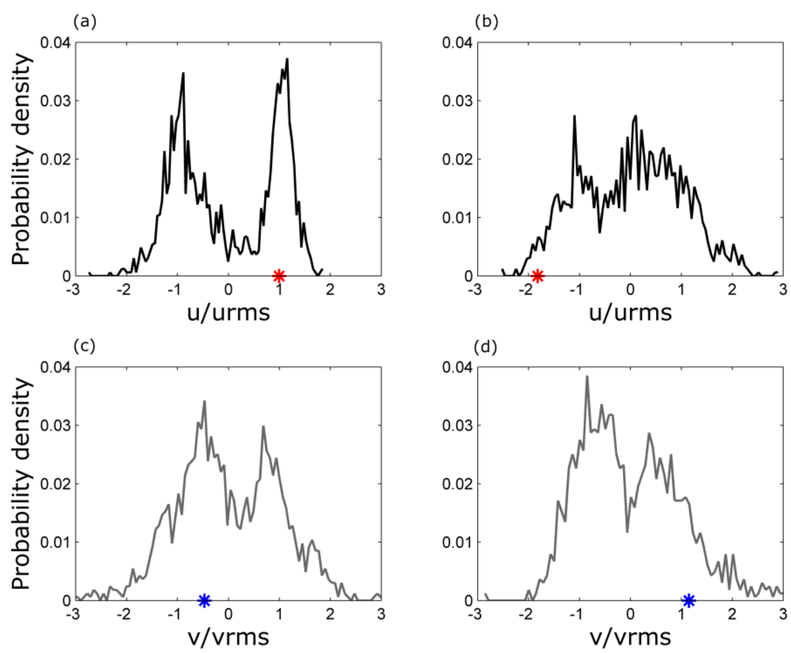

Figure 2.19-Characteristic plots of probability density functions for the non-dimensionalized fluctuations of the streamwise (a and b) and wall-normal (c and d) velocity components. The plots refer to HRe case and their location in the flow domain is described by the coordinates (X/D, Y/D): (a) (−0.181, 0.002), (b) (−0.323, 0.038), (c) (−0.175, 0.014), and (d) (−0.160, 0.104).

The appearance of two distinct peaks shown in the probability density functions of figure 2.19(a) and figure 2.19(c) is a typical feature of the horseshoe vortex dynamics. There are other characteristics, however, that these p.d.f.s do not share in common. For example, the relative size of the two peaks, which is an indirect indication of the prominence of each one of the extreme modes, varies to a degree that in some cases one peak has twice the height of the other. In addition, while one of the peaks is always centered on zero velocities, its distance from the second peak ranges from one to three standard deviations of non-dimensionalized velocity fluctuations. Finally, the shape of the p.d.f.s in the majority of measurement points is highly irregular. Velocity data in general did not follow the normal distribution, even in areas of the flow field where bimodality is not present. The hypothesis of normality was tested at all points of the measuring grid and for all cases Re_D using the *Kolmogorov−Smirnov* test. Results showed that at the 0.05 significance level the percentages of locations in the flow domains where the streamwise velocity signals fitted the normal distribution were: 11.26% for LRe, 25.16% for MRe, and 17.85% for HRe. These numbers do not indicate a consistent trend between normality and Re_D. Similarly, the test results for the wall-normal velocities were: 21.31% for LRe, 15.56% for MRe, and 9.45% for HRe. For this velocity component, we observe a trend of decreasing normality with the increase of Reynolds number. Spatial maps of skewness for both velocity components (although not presented here) corroborated the deviations from normal distribution.

Having revisited the interpretation and the characteristics of double-peaked p.d.f.s within the frame of horseshoe vortex dynamics, we now focus on the effect of Re_D. Figure 2.20 (a-c) shows the exact locations in the flow domains where the probability density functions exhibit bimodal features. The presence of bimodality in all three Re_D cases confirms the findings of the previous discussion on time-resolved results. The two characteristic flow modes are indeed a common feature of the junction flows investigated here. Bimodality of streamwise velocity fluctuations is exhibited primarily below HV1. The unsteady regions coincide with the path of the near-wall jet of reversed fluid. Of interest is the orientation of these regions. While for LRe and MRe they are nearly parallel to the bed, for the HRe case the orientation is oblique. This is reminiscent of the characteristic pattern observed in the time-averaged maps of vorticity (figure 2.4 a-c), TKE (figure 2.5 a-c), and streamwise turbulence intensity (figure 2.6 a-c). Note, also, that for the MRe and HRe cases a second bimodal region exists in the area of action of the secondary vortex. This finding underscores that HV2 assumes a more energetic role within higher Re_D flows. The extent of bimodal regions for the wall-normal velocity component is, on the other hand, smaller than that of the streamwise velocity component for the LRe case (figure 2.20a). Bimodality of wall-normal velocities occupies larger areas for the MRe and HRe cases (figure 2.20a, b). These areas coincide with the core and the outer edges of the time-averaged primary vortex. A notable exception occurs for MRe. For this case, a second bimodal region exists just upstream of HV2. It is possible though, that the existence of this region is also attributed to the behavior of HV1. As demonstrated both in the time-resolved section and in figure 2.20 (a-c), the orbiting motion of HV1 envelops a larger area, which stretches beyond 0.3D upstream of the origin. When at its remote upstream position, the left edge of the primary vortex overlaps with the bimodal region under consideration. This is another testimony to the fact that time-averaged analysis only partially describes the complex dynamics of junction flows.

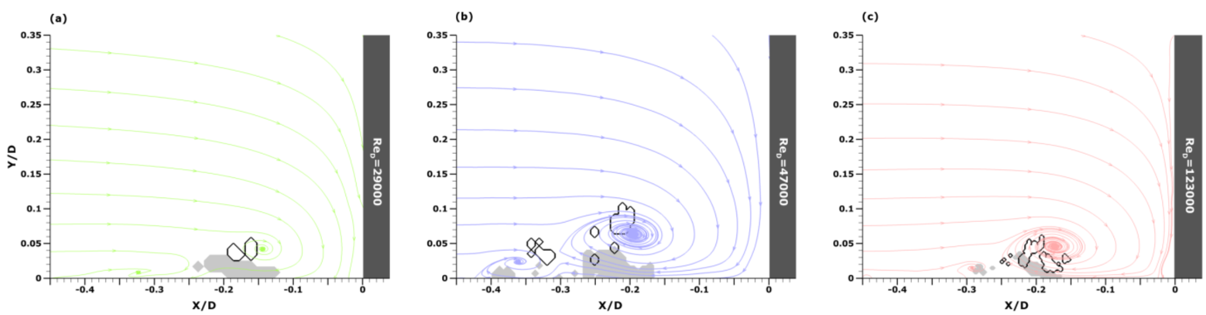

Figure 2.20-Bimodal regions of the streamwise (solid grey areas) and wall-normal (areas bounded by black lines) fluctuating velocity components. Time-averaged streamlines are superimposed.

Devenport & Simpson (1990) were the only ones that documented in detail bimodal regions for the streamwise and wall-normal velocity components. We attempt here a comparison between their maps and those of the HRe case. Notwithstanding existing differences between the two studies (working fluid, boundary layer thickness, shape of obstacle, measuring technique), the levels of the main parameter of interest, namely the Reynolds number, render this comparison meaningful. According to their results, bimodal p.d.f.s of streamwise velocity characterized a continuous region. Its shape was nearly elliptical and was bounded between $-0.13<X/D<-0.37$ in the horizontal direction and between $0.00<Y/D<0.09$ in the vertical direction. Similarly, the area of bimodal p.d.f.s for wall-normal velocities occupied a continuous elliptic-shaped region. Slight differences were reported regarding its extent: the horizontal limits were $-0.12<X/D<-0.36$ and the vertical ones were $0.00<Y/D<0.10$. These numbers indicate a significant overlap between the bimodal regions of each velocity component. Our analysis does not corroborate this feature (figure 2.20 a-c). Additional discrepancies exist with respect to the overall extent of the bimodal regions. According to the PIV data presented here, the bimodality is exhibited at smaller and non-continuous areas of the flow domain. These areas, however, fall within the limits provided in the mentioned study. It is therefore concluded that the findings of the two studies are not contradictory. Our results can be regarded as a refinement in the spatial extent of the bimodal regions of junction flows that complements the original findings of Devenport & Simpson (1990).

2.3.3.3 **Flow unsteadiness and velocity probability density functions**

To further investigate junction flow unsteadiness, we examine the probability density functions of velocity fluctuations along vertical transits of the flow field. Five locations are selected. These are representative of the following flow features: a) incoming boundary layer flow, b) secondary vortex, c) saddle region in between HV1 and HV2, d) primary vortex, and e) downwash/return flow. Figure 2.21 depicts the exact locations for the HRe case. As indicated previously, the time-averaged flow topologies were not identical for the three Re_D experiments. Therefore, to render comparisons between cases meaningful, we ensured that for LRe and MRe, transits b and d crossed the core of HV2 and HV1. Then, the locations a, c, and e were selected to have the same dimensionless distances upstream or downstream of b and d as those shown in figure 2.21 for the HRe case.

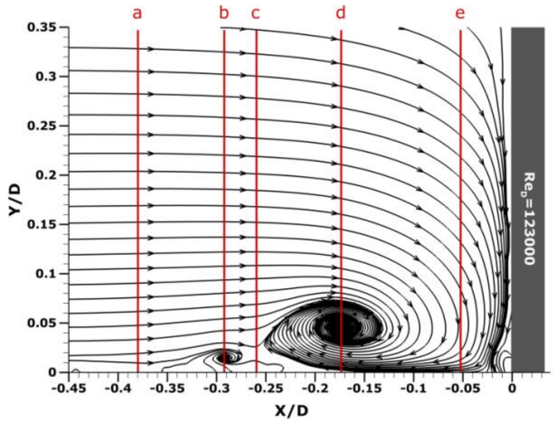

Figure 2.21-Locations of vertical transits along which instantaneous velocities were extracted and probability density functions were calculated.

Figure 2.22 (a-e) through figure 2.24 (a-e) depict the variation of the probability density functions of streamwise velocity fluctuations along the mentioned transits and for each Re_D case. Solid black lines correspond to the time-averaged velocities and allow for a direct comparison between the time-averaged and unsteady flow dynamics. For the incoming boundary layer flow (subfigures a), the results from both analyses are in good agreement: the velocity profile overlaps with locations where the p.d.f.s obtain their highest values. The width of the colored band is approximately 0.5 dimensionless units of U/U_o and remains relatively constant along the transit for all three cases. Incoming flow exhibits, therefore, a steady behavior in both time and space. The first signs of unsteadiness are found within the system of horseshoe vortices. For example, observe that the width of p.d.f contour plots increases significantly for transit b of figure 2.24. The increase takes place within and above the time-averaged footprint of the secondary horseshoe vortex. The same trend characterizes p.d.f.s of transits c, which are located in the saddle region in between the two vortices. The phenomenon is particularly pronounced for the LRe case (figure 2.22 a-e). A wide range of values characterizes the instantaneous velocities at vertical locations from near the bed, up to 0.12D. Besides flow unsteadiness, a closer inspection of subfigures (c) reveals discrepancies between most probable and time-averaged velocities. This feature is most evident in the near-wall regions. There, the no-slip condition results in the retardation of flow with velocities obtaining close-to-zero magnitudes. In this region, time-averaged velocities do not necessarily coincide with the most probable velocity values, because their estimated values become sensitive to the wide range of positive and negative fluctuations of the unsteady flow. In this way, it is demonstrated that mean streamwise velocities in a time-averaged sense are not always good estimators of the flow field in the particular regions of the juncture. Furthermore, wide-banded p.d.f.s and strong inflection points in the velocity profiles characterize transits d, which cross the core of the primary vortex. These features are manifestations of the flow unsteadiness that has been described in detail within the time-resolved analysis. In addition, they are common features for every Re_D case examined here. Overall, a junction flow consistently becomes more unsteady at the saddle region and at the area of action of the primary vortex. Subfigures (e) verify this conclusion. With the exception of LRe case, the width of the p.d.f. contours in (e) is of the same order as that of subfigures (a) and (b). Nevertheless, the unsteadiness of LRe for the downwash/return flow is more significant and extends throughout the height of the transit (figure 2.22 a-e). Note also that the p.d.f. contours within the same subplot are skewed negatively, indicating a departure from the normal distribution for the streamwise velocity component.

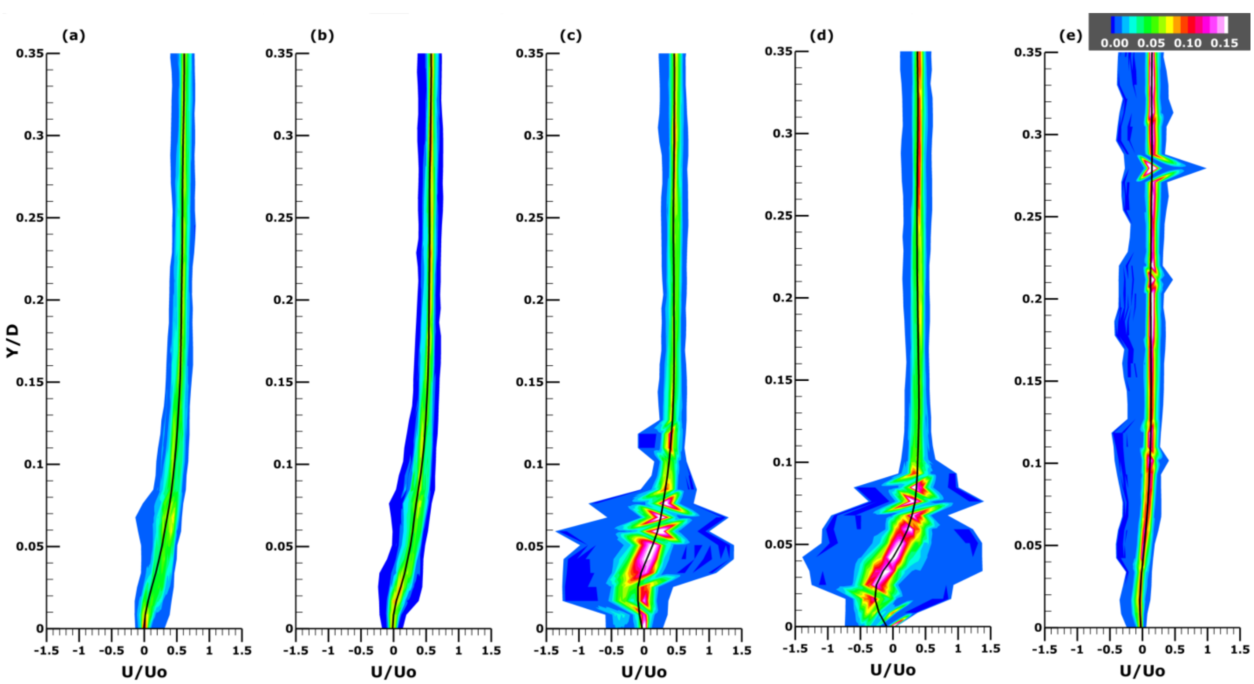

Figure 2.22-Mean streamwise velocity profiles (black lines) superimposed on probability density function contours for LRe case.

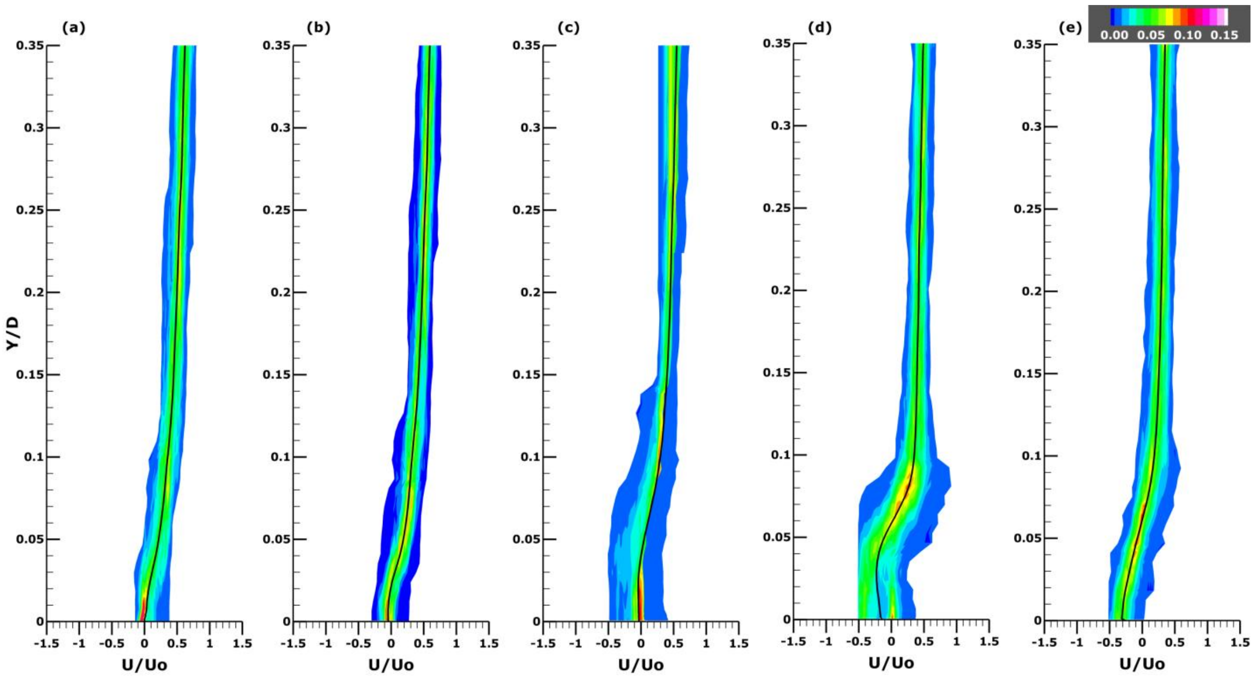

Figure 2.23-Mean streamwise velocity profiles (black lines) superimposed on probability density function contours for MRe case.

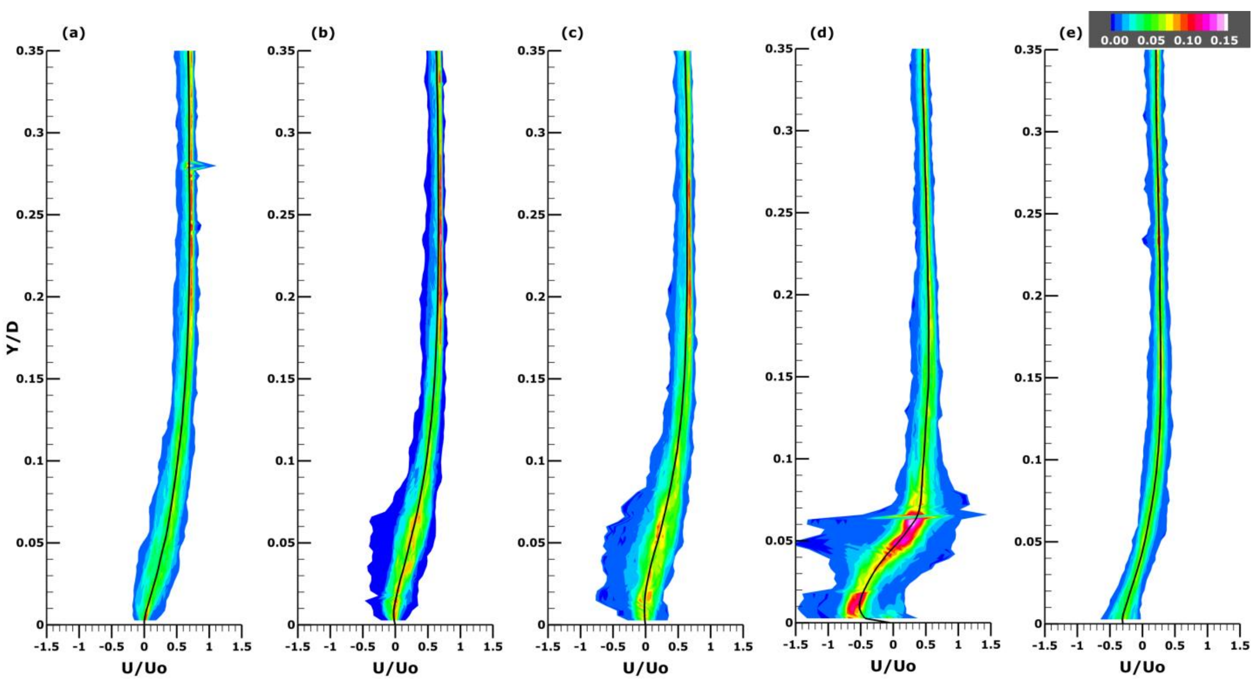

Figure 2.24-Mean streamwise velocity profiles (black lines) superimposed on probability density function contours for HRe case.

The combined analysis of the probability density functions and time-averaged velocities along the prescribed transits of figure 2.21 is extended to include the wall-normal component. Compared to the streamwise profiles, we observe that the variation of wall-normal velocities with height is consistently smaller (figure 2.25 − figure 2.27). More specifically, at locations a and b the near-zero, wall-normal velocities are accompanied with narrow-banded p.d.f.s contours. Furthermore, inflection points in the velocity profiles are limited to transits d and e. Nevertheless, similarities also exist. One is with respect to disparities between the time-averaged velocity profile and the maxima of the p.d.f. contours. Figure 2.25(d) and figure 2.27(d) support this statement. A second similarity is that flow unsteadiness characterizes primarily regions immediately upstream (transits c) and at the time-averaged location of HV1 (transits d). It is only for LRe case that the p.d.f.s of the wall-normal fluctuations imply unsteady flow behavior for the downwash/return flow closer to the obstacle (figure 2.25e). The characteristic peaks in the p.d.f. contours located at 0.1D, 0.185D, 0.21D, and 0.28D above the bed are signs of irregular flow throughout the height of the transit. Recall that the time-averaged results of wall-normal velocities for the MRe case (figure 2.3b) revealed a strong downwash of fluid running down the face of the cylinder. Apparently, and despite its high-momentum content, this jet exhibits a rather steady behavior as indicated by the relatively narrow band of p.d.f. contours, especially in locations above 0.15D (figure 2.26e).

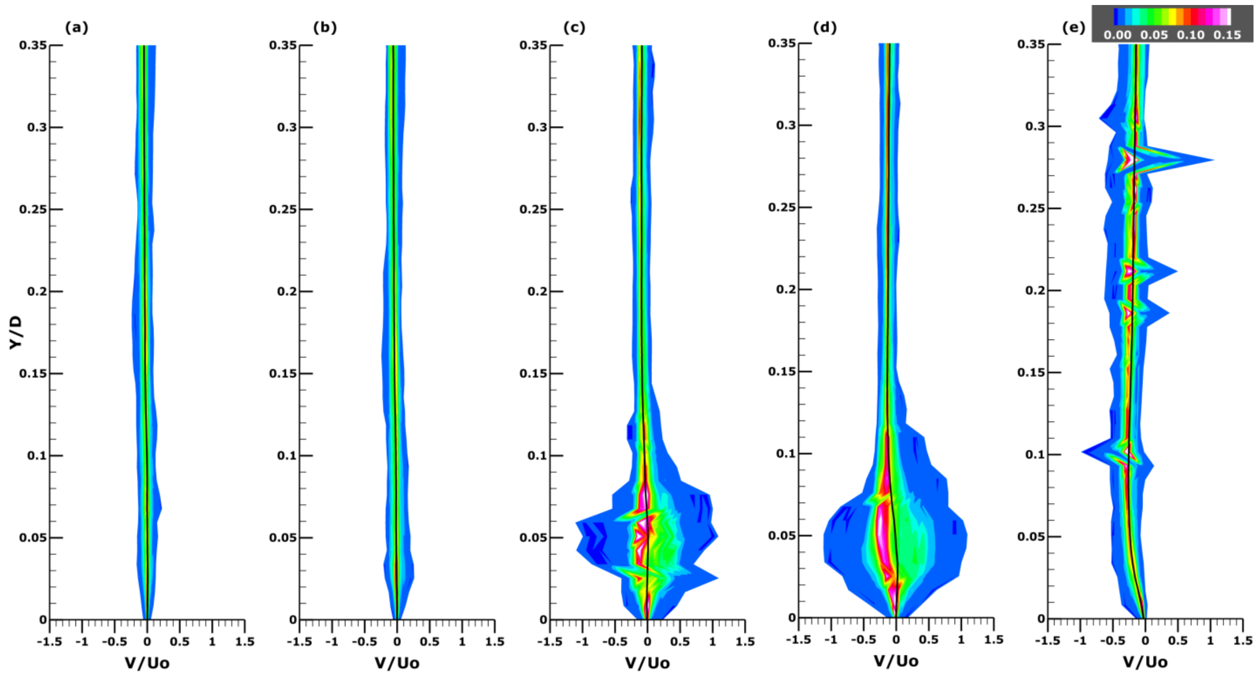

Figure 2.25-Mean wall-normal velocity profiles (black lines) superimposed on probability density function contours for LRe case.

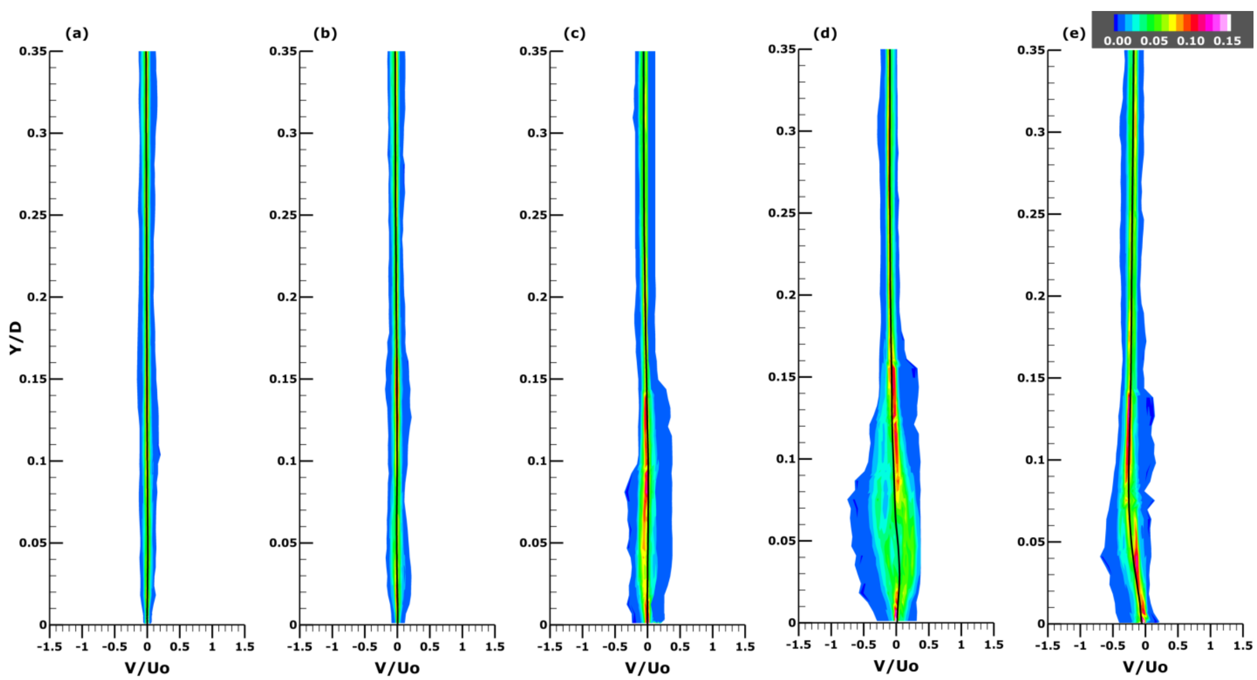

Figure 2.26-Mean wall-normal velocity profiles (black lines) superimposed on probability density function contours for MRe case.

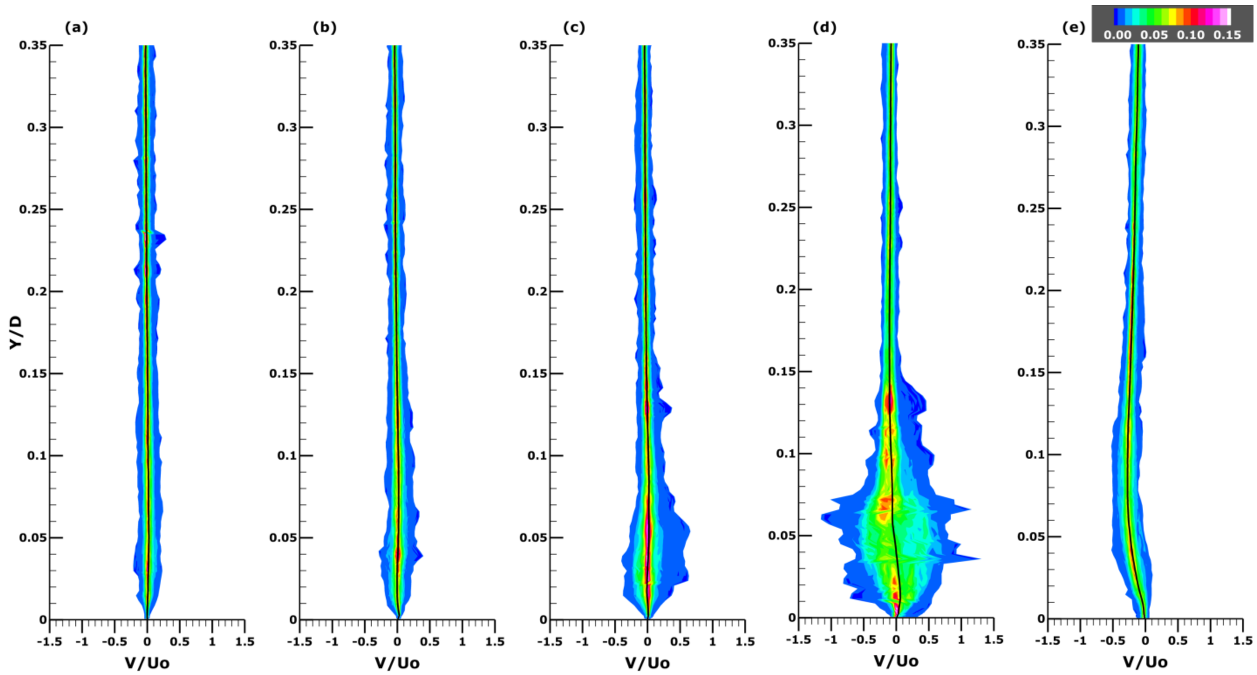

Figure 2.27-Mean wall-normal velocity profiles (black lines) superimposed on probability density function contours for HRe case.

2.4 Summary and conclusions

The turbulent flow upstream of a vertical circular cylinder mounted on a smooth flat wall was investigated experimentally. The cylindrical obstacle was installed vertically and at the mid-width of an open channel with its upper part piercing the free surface of the flow. This idealized setup is prototype to a number of engineering applications. Knowledge of flow structure at the wall−cylinder junction is of paramount importance for the design and operation of these systems. Emphasis was placed on the effects of scale on the physics of the flow as expressed with variations in Reynolds number. Particle Image Velocimetry measurements resolved the time-averaged and instantaneous flow fields at three levels of Re_D. Statistical analyses and quantitative flow visualizations elucidated the dynamics that govern fluid−structure interactions in this fundamental junction flow configuration.

The time-averaged topology is Re_D-invariant regarding its basic features: the presence of two organized vortical structures (HV1, HV2) and the absence of two others (HV3, CV) that have been included in previous topological models. On the contrary, the absolute and relative locations of the primary and secondary vortex vary with Re_D, but without following any apparent trend. Flow streamlines are focused into larger and more coherent vortex cores for the MRe and HRe experimental runs. The more prominent role of the HV1 in the dynamics of the junction flow for the HRe case is also inferred from streamline topology. In general, negative vorticity is concentrated in elliptical blobs marking the cores of the primary vortices. Positive vorticity characterizes two elongated patches, which develop near the wall and close to the cylinder. Elevated levels of the kinetic energy and intensity of turbulence measured below HV1 for the HRe case are suggestive of a stronger wall−vortex interaction at this high level of Re_D.

The instantaneous flow fields for HRe compared to those of the other two cases (LRe and MRe, which were characterized by Reynolds numbers an order of magnitude smaller) differ in that: 1) for specific flow episodes the primary horseshoe vortex is advected rapidly upstream, 2) the vorticity and momentum of the incoming flow assume higher levels, 3) the eruptions of near-wall fluid below HV1 are more violent, 4) secondary vortical structures (HV2, HV3 etc.) are smaller, more intermittent, and less coherent, 5) all flow modes are characterized by lower frequencies of appearance. In addition, a unique feature of the MRe case was the high-momentum patch of fluid running down the face of the cylinder. LRe experiment, on the other hand, was the only one during which flow episodes showing the disintegration of HV1 occurred. It was also characterized by the prominence of the zeroflow mode in both duration and frequency of appearance. Besides, reasonable agreement existed between our results and the instantaneous characteristics of published junction flows. The most outstanding differences were detected with respect to: 1) the presence of a third flow mode of intermediate characteristics between the zeroflow and the backflow, 2) the origin of the return flow and the mechanism of near-wall eruptions, 3) the topologies of the zeroflow and backflow modes, 4) the relatively constant number (four to five) of properly closed vortices that was observed in our tests, independent of Re_D.

Coherent structure analysis and statistical tools were also used to probe into the physics of the turbulent junction flows. It was demonstrated that the non-uniformity and unsteadiness characterizing the trajectories of the primary vortex increases with Reynolds number. The need for a deeper investigation on the unsteady dynamics of the turbulent horseshoe vortex motivated our efforts to establish a rigorous explanation of the link between the modal instability and the double-peaked velocity p.d.f.s. We showed that the bimodal behavior is a common characteristic of all three experimental cases studied here. Nevertheless, detailed maps quantified the differences regarding the extent of the bimodal regions for every Re_D case and every velocity component measured. A closer inspection of the flow field at selected vertical transits identified the onset of flow instability at the saddle region between the time-averaged locations of HV1 and HV2. Regardless of Re_D, the unsteadiness is more pronounced in the near wall region (Y<0.1D), which is characterized by inflection points in the velocity profiles. Furthermore, differences were highlighted between the time-averaged velocity magnitudes and their most probable values, as extracted from the probability density functions. Finally, the documented departures from the normal distribution for the measured velocity signals further demonstrated the complexity of the junction flows irrespective of the level of the Reynolds number.

The results presented in this paper could be potentially used as a first guide to control the characteristics of turbulent junction flows at comparable setups. Depending on the desired outcome (heat transfer enhancement, drag reduction, or mitigation of scouring) the emphasis should be on particular flow features, their frequencies of appearance, and their interaction in both space and time. The aforementioned conclusions provide a good starting point for the identification of regions and flow mechanisms of interest.

Viewed from a different perspective, our results could claim additional merit in enhancing the physical justification of theoretical (Hunt *et al.* 1978) or numerical models of junction flows (Rodi 1997). Recent attempts to develop robust computational tools for the prediction of separated junction flows have met with a good deal of success (Paik *et al.* 2007; Kirkil & Constantinescu 2009). The data and analyses included here provide the much needed physical insight to incorporate effects of scale on the computational modelling/simulation of the phenomenon under study and, thus, extend the capabilities of these tools.

The conclusions of this work should be considered within the context of its limitations, the most important of which are: the blockage effects for the HRe case, the (inherent in PIV) ambiguity regarding the accuracy of data near the solid boundaries, out-of-plane particle motion, and the fact that the effect of the boundary layer could have possibly become confounded within the results. Our work covers three Re_D cases at levels representative of real-life engineering applications. These levels fall within the range of Re_D that has been typically reported in experimental and numerical studies. Nevertheless, we disclaim any attempt to extend our conclusions to any other Re_D, outside the investigated range.

2.5 Acknowledgements

This study was supported by the National Science Foundation (EAR 0738759) and the Research Office of the U.S. Army Corps of Engineers (ARO 53512-EV). The first author would like to acknowledge the generous support he received from the Academy of Athens (Argyropoulos fellowship) and the Gerondelis Foundation. We thank Professor P. P. Vlachos and Dr. S. Raben for their invaluable assistance with the PIV experiments.

2.6 References

ADRIAN, R. J. 1997 Dynamic ranges of velocity and spatial resolution of particle image velocimetry. *Meas. Sci. Technol.* **8**, 1393–1398.

ADRIAN, R. J. & WESTERWEEL, J. 2011 *Particle Image Velocimetry*. Cambridge University Press.

AGUI, J. H. & ANDREOPOULOS, J. 1992 Experimental investigation of a three-dimensional boundary layer flow in the vicinity of an upright wall mounted cylinder. *J. Fluids Engng* **114**, 566-576.

ALI, K. H. M. & KARIM, O. 2002 Simulation of flow around piers. *J. Hydraul. Res.* **40**, 161-174.

ALLEN, J. J. & NAITOH, T. 2007 Scaling and instability of a junction vortex. *J. Fluid Mech.* **574**, 1-23.

BAKER, C. J. 1979 The turbulent horseshoe vortex. *J. Wind. Engng Ind. Aerod.* **6**, 9-23.

BALLIO, F., BETTONI, C. & FRANZETTI, S. 1998 Survey of time-averaged characteristics of laminar and turbulent horseshoe vortices (Data bank contribution). *J. Fluids Engng* **120**, 233-242.

CHARONKO, J. & VLACHOS, P. P. 2013 Estimation of uncertainty bounds for individual particle image velocimetry measurements from cross-correlation peak ratio. *Meas. Sci. Technol.* **24**, 065301.

DARGAHI, B. 1989 The turbulent flow field around a circular cylinder. *Exp. Fluids* **8**, 1-12.

DEVENPORT, W. J. & SIMPSON, R. L. 1990 Time-dependent and time-averaged turbulence structure near the nose of a wing–body junction. *J. Fluid Mech.* **210**, 23-55.

ECKERLE, W. A. & AWAD, J. K. 1991 Effect of freestream velocity on the 3-dimensional separated flow region in front of a cylinder. *J. Fluids Engng* **113**, 37-44.

ECKSTEIN, A., CHARONKO, J. & VLACHOS, P. P. 2008 Phase correlation processing for DPIV measurements. *Exp. Fluids* **45**, 485-500.

ECKSTEIN, A. & VLACHOS, P. P. 2009a Assessment of advanced windowing techniques for digital particle image velocimetry (DPIV). *Meas. Sci. Technol.* **20**, 075402.

ECKSTEIN, A. & VLACHOS, P. P. 2009b Digital particle image velocimetry (DPIV) robust phase correlation. *Meas. Sci. Technol.* **20**, 055401.

ESCAURIAZA, C. & SOTIROPOULOS, F. 2011a Initial stages of erosion and bed form development in a turbulent flow around a cylindrical pier. *J. Geophys. Res.* **116**, F03007.

ESCAURIAZA, C. & SOTIROPOULOS, F. 2011b Lagrangian model of bed-load transport in turbulent junction flows. *J. Fluid Mech.* **666**, 36-76.

ESCAURIAZA, C. & SOTIROPOULOS, F. 2011c Reynolds number effects on the coherent dynamics of the turbulent horseshoe vortex system. *Flow Turbul. Combust.* **86**, 231-262.

ETEBARI, A. & VLACHOS, P. P. 2005 Improvements on the accuracy of derivative estimation from DPIV velocity measurements. *Exp. Fluids* **39**, 1040-1050.

FLEMING, J. L., SIMPSON, R. L., COWLING, J. E. & DEVENPORT, W. J. 1993 An experimental study of a turbulent wing body junction and wake flow. *Exp. Fluids* **14**, 366-378.

FOUCAUT, J. M. & STANISLAS, M. 2002 Some considerations on the accuracy and frequency response of some derivative filters applied to particle image velocimetry vector fields. *Meas. Sci. Technol.* **13**, 1058.

GAND, F., DECK, S., BRUNET, V. & SAGAUT, P. 2010 Flow dynamics past a simplified wing body junction. *Phys. Fluids* **22**, 115111.

HONKANEN, M. & NOBACH, H. 2005 Background extraction from double-frame PIV images. *Exp. Fluids* **38**, 348-362.

HUNT, J. C. R., ABELL, C. J., PETERKA, J. A. & WOO, H. 1978 Kinematical studies of flows around free or surface-mounted obstacles - Applying topology to flow visualization. *J. Fluid Mech.* **86**, 179-200.

HUNT, J. C. R., WRAY, A. A. & MOIN, P. 1988 Eddies, streams, and convergence zones in turbulent flows. In *Proceedings of the Summer Program*, Center for Turbulence Research, NASA, 193-208.

ISHII, J. & HONAMI, S. 1986 A three-dimensional turbulent detached flow with a horseshoe vortex. *J. Engng Gas Turb. Power* **108**, 125-130.

KIRKIL, G. & CONSTANTINESCU, G. 2009 Nature of flow and turbulence structure around an in-stream vertical plate in a shallow channel and the implications for sediment erosion. *Water Resour. Res.* **45**, W06412.

KIRKIL, G. & CONSTANTINESCU, G. 2010 Flow and turbulence structure around an in-stream rectangular cylinder with scour hole. *Water Resour. Res.* **46**, W11549.

KIRKIL, G., CONSTANTINESCU, G. & ETTEMA, R. 2006 Investigation of the velocity and pressure fluctuations distributions inside the turbulent horseshoe vortex system around a circular bridge pier. In: R. M. L. Ferreira, E. Alves, J. Leal & A. H. Cardoso eds. *River Flow 2006. pp.* 709-718. Balkema, Lisbon.

KOKEN, M. & CONSTANTINESCU, G. 2009 An investigation of the dynamics of coherent structures in a turbulent channel flow with a vertical sidewall obstruction. *Phys. Fluids* **21**, 085104.

NEZU, I. & NAKAGAWA, H. 1993 *Turbulence in open-channel flows*. Balkema.

OLCMEN, S. M. & SIMPSON, R. L. 1994 Influence of wing shapes on surface pressure fluctuations at wing-body junctions. *AIAA Journal* **32**, 6-15.

PAIK, J., ESCAURIAZA, C. & SOTIROPOULOS, F. 2007 On the bimodal dynamics of the turbulent horseshoe vortex system in a wing-body junction. *Phys. Fluids* **19**, 115104.

PRAISNER, T. J., SEAL, C. V., TAKMAZ, L. & SMITH, C. R. 1997 Spatial-temporal turbulent flow-field and heat transfer behavior in end-wall junctions. *Int. J. Heat Fluid Flow* **18**, 142-151.

PRAISNER, T. J. & SMITH, C. R. 2006a The dynamics of the horseshoe vortex and associated endwall heat transfer - Part I: Temporal behavior. *J. Turbomach.* **128**, 747-754.

PRAISNER, T. J. & SMITH, C. R. 2006b The dynamics of the horseshoe vortex and associated endwall heat transfer - Part II: Time-mean results. *J. Turbomach.* **128**, 755-762.

RAFFEL, M., WILLERT, C. E., WERELEY, S. T. & KOMPENHANS, J. 2007 *Particle Image Velocimetry-A practical guide*. Springer.

RODI, W. 1997 Comparison of LES and RANS calculations of the flow around bluff bodies. *J. Wind. Engng Ind. Aerod.* **69-71**, 55-75.

ROULUND, A., SUMER, B. M., FREDSOE, J. & MICHELSEN, J. 2005 Numerical and experimental investigation of flow and scour around a circular pile. *J. Fluid Mech.* **534**, 351-401.

SABATINO, D. R. & SMITH, C. R. 2009 Boundary layer influence on the unsteady horseshoe vortex flow and surface heat transfer. *J. Turbomach.* **131**, 011015.

SCARANO, F. 2002 Iterative image deformation methods in PIV. *Meas. Sci. Technol.* **13**, R1-R19.

SHAVIT, U., LOWE, R. & STEINBUCK, J. 2007 Intensity Capping: a simple method to improve cross-correlation PIV results. *Exp. Fluids* **42**, 225-240.

SIMPSON, R. L. 2001 Junction flows. *Annu. Rev. Fluid Mech.* **33**, 415-443.

TIMMINS, B., WILSON, B., SMITH, B. & VLACHOS, P. P. 2012 A method for automatic estimation of instantaneous local uncertainty in particle image velocimetry measurements. *Exp. Fluids* **53**, 1133-1147.

VLACHOS, P. P. 2000 An experimental spatio-temporal analysis of seperated flows over bluff bodies. PhD thesis, Virginia Tech.

WALLACE, J. M. & FOSS, J. F. 1995 The measurement of vorticity in turbulent flows. *Annu. Rev. Fluid Mech.* **27**, 469-514.

WESTERWEEL, J. 1997 Fundamentals of digital particle image velocimetry. *Meas. Sci. Technol.* **8**, 1379-1392.

WESTERWEEL, J. & SCARANO, F. 2005 Universal outlier detection for PIV data. *Exp. Fluids* **39**, 1096-1100.

WILSON, B. M. & SMITH, B. L. 2013 Uncertainty on PIV mean and fluctuating velocity due to bias and random errors. *Meas. Sci. Technol.* **24**, 035302.

3 Effects of wall roughness on turbulent junction flow characteristics

Nikolaos Apsilidis, Panayiotis Diplas, Clinton L. Dancey, Polydefkis Bouratsis

ABSTRACT: Global measurements of turbulent flows at wall−cylinder junctions are employed to quantify the effects of wall roughness on the behavior of the horseshoe vortex system (HVS). Two laboratory setups were considered: one with an impermeable smooth wall and a second characterized by a porous hydraulically-rough bed. The measurements were obtained using planar Particle Image Velocimetry. Time-averaged flow topology, turbulence statistics, and instantaneous fields associated with the streamwise and wall-normal velocity components are emphasized. Proper Orthogonal Decomposition (POD) is also applied on the velocity signals to probe into the characteristics of the energetic flow structures. For the Reynolds numbers studied here and the specific differences in the roughness geometry of the bed, a clear trend for increase in flow incoherence due to the rough wall is documented. It is also demonstrated that, in the presence of roughness, vorticity and turbulence spread more evenly throughout the junction. On the other hand, qualitative and quantitative agreement between the smooth and rough bed tests is found in the structure of the downflow and the near-wall jet opposing the bulk flow. The efficiency of POD in analyzing turbulent junction flows is justified based on its results and metrics of modal energy distribution. POD verified in an objective way the role of integral parts of the HVS dynamics such as the vortices comprising the system and their interplay with the wall. The decomposition furnishes new evidence about energetic structures that were not captured with the other data analysis methodologies. It also confirms the aperiodic behavior of the HVS for the investigated Reynolds numbers.

3.1 Introduction

Wall−body junctures are integral components of systems encountered in a number of engineering fields such as aerodynamics, turbomachinery, electronics, and infrastructure hydraulics. Understanding the transport phenomena at these regions is of paramount importance for design, construction, and maintenance purposes. The dynamics of transport processes largely depends on the physics of the flows at the junction. Due to the characteristic geometry, the incoming flow undergoes structural transformations at the neighborhood of the body. The moving fluid decelerates, separates from the wall, and changes directions. This activity gives birth to organized and self-sustained flow patterns, which comprise the so-called horseshoe vortex system (HVS).

The behavior of HVS over a smooth wall has received significant research attention. The reader is referred to the review of Simpson (2001) for a meticulous presentation of the state of knowledge on junction flows until the late 90's. This work summarized the effects of factors related to flow and geometry characteristics and elaborated on the difficulties in modeling the unsteady behavior of the HVS. Subsequent studies capitalized on recent strides in experimental techniques (Westerweel, Elsinga & Adrian 2013) and computational methods (Sagaut 2006; Spalart 2009). The focus has been on the study of turbulent HVSs. The prevalent topology of such flows consists of two to four vortices of varying sizes (Praisner & Smith 2006b; Paik, Escauriaza & Sotiropoulos 2007; Kirkil & Constantinescu 2009). Wall−vortex and vortex−vortex interactions amplify turbulence intensity and bed shear stresses within the junction region. Such phenomena have been attributed to the quasi-organized activity of the HVS manifested in the form of the characteristic zeroflow and backflow modes (introduced by Devenport & Simpson (1990)). These flow features appear in a number of model studies (Kirkil, Constantinescu & Ettema 2006; Praisner & Smith 2006a; Paik et al. 2007; Kirkil & Constantinescu 2009; Sabatino & Smith 2009; Gand et al. 2010; Escauriaza & Sotiropoulos 2011), hence they constitute an established characteristic of turbulent junction flows. Additional research has emphasized the role of smaller flow structures (hairpin vortices) in the destabilization of the HVS and the switching between the dominant flow-modes (Paik et al. 2007). The number and intensity of hairpins appear to increase with Reynolds number (Escauriaza & Sotiropoulos 2011). Finally, evidence has been furnished that links HVS dynamics with phenomena occurring outside the juncture, such as the turbulent bursting in the incoming boundary layer (Sabatino & Smith 2009) and corner separation at the flanks of the body (Gand et al. 2010).

In contrast to the well-documented case of junction flows developing over smooth and impermeable walls, there is a paucity of investigations on the (more realistic) rough-bed paradigm. In a joint experimental−computational study, Roulund et al. (2005) used Laser Doppler Velocimetry data to train a numerical code in modeling junction flows under a variety of conditions. One of them was bed roughness, in the form of a layer of crushed stones. Computed results revealed a limited influence of this factor on the HVS, expressed primarily as a mild trend of reduction in the flow recirculation area with the increase of roughness. Some caution should be exercised on the interpretation of these findings, however, because of deficiencies of the experimental technique to conclusively resolve the dynamics of the HVS. Ahmed & Rajaratnam (1998) measured amplified shear stresses at the junction of a body with a wall made of sand glued on a wooden board. They also found that the footprint of high shear was increased compared to the benchmark, smooth bed case. The elevated uncertainty in the velocity measurements (obtained with a Prandtl tube) precluded the extraction of concrete conclusions about the impact of bed roughness on the junction flow field. Tsikata & Tachie (2013) studied the combined effects of roughness and adverse pressure gradient on a turbulent boundary layer. Although the adverse pressure gradient was not the result of flow blockage from a surface-mounted obstacle (instead, a diverging section of the channel was employed) the results could still be relevant to junction flows. In particular, it was demonstrated that the structure of the boundary layer flow was altered both near and away from the wall. Furthermore, increased turbulence kinetic energies (TKE) and Reynolds stresses were attributed to the rough wall and the pressure field.

For the sake of completeness, it is mentioned that a plethora of studies have investigated the effect of roughness on wall-bounded flows at zero-pressure gradients and in the absence of a junction geometry. It is neither intended nor is it possible to summarize here the state-of-the-art on canonical flows over rough walls. It suffices to underscore the consensus about the limited understanding we have on the subject

(Patel 1998; Jimenez 2004; Flack & Schultz 2010). An enhanced physical insight is, therefore, sought for modeling and controlling of these flows.

The objective of this investigation is to examine the effects of a fully rough and porous bed on the physics of junction flows. Particular emphasis was placed on the behavior of the large-scale, energetic flow structures comprising the HVS. This was pursued experimentally through comparisons of Particle Image Velocimetry (PIV) data. Two wall−cylinder junction setups were considered. The first one consisted of a hydraulically smooth, impermeable bed and is referred as the SB test. For the second setup, gravel grains made for a fully rough, irregular, porous, and immobile bed surface. This experiment will be mentioned from now on as the RB test.

The paper is organized as follows. First, the experimental investigation is described in details. Next, the mechanics of Particle Image Velocimetry data analysis and post-processing based on Proper Orthogonal Decomposition (POD) are presented. The focus is then shifted on the results, where time-averaged flow and turbulence statistics are discussed. This is followed by the analysis of the instantaneous velocity fields. Subsequently, the most energetic POD modes and their contribution to the phenomenon are examined. Finally, an outline of the major findings of this study concludes the paper.

3.2 Experimental setup

3.2.1 Facilities and physical models

Experiments were carried out at Virginia Tech and more specifically at the premises of the Advanced Experimental Thermofluid Research Laboratory and the Baker Environmental Hydraulics Laboratory. For the SB test, a water tunnel with a test section of 1.81 m (length) × 0.61 m (width) × 0.61 m (height) was used. The RB experiment took place in a recirculating flume with corresponding dimensions of 15.00 m × 1.20 m × 0.40 m. The length of the flume and the roughness of the bed material (crushed limestone with median particle size diameter of d_{50}=3.6 mm) allowed for the full development of the flow. This was not the case for the water tunnel with the smooth wall. To compensate for this discrepancy, a sand strip comprised of distributed roughness elements of 1 mm was installed at the inlet of the test section. In this way, it was intended to generate as thick a boundary layer as possible. Past studies (Paik et al. 2007; Koken & Constantinescu 2009; Escauriaza & Sotiropoulos 2011) have advocated that the effect of boundary thickness, δ_{99}, on the dynamics of junction flows is rather limited for the case of relatively thick boundary layers (i.e. those for which $\delta_{99}>0.2D$, where δ_{99} is the boundary layer thickness based on the 99% of the free-stream velocity, Uo, and D is the diameter of the cylinder). Here, for the smooth bed test, the diameter of diameter was D=15.2 cm and the flow depth H=18.0 cm. The respective numbers for the RB test were D=8.90 cm and H=16.5 cm.

The schematic description of the physical models and the basic parts of the PIV systems is presented in figure 3.1. A major goal was to take full advantage of the non-intrusive nature of the PIV technique. For the SB test, the transparent wall conveniently allowed for the delivery of the light from the bottom of the channel (figure 3.1a). On the contrary, the opaque sediment layer of the RB experiment dictated an alternative setup. Two options were considered for the path of laser light through the junction region: a) to penetrate the free surface of the flow and b) to cross the interior of the cylinder. Solution a) would entail the additional installation of a transparent lid (or a floating window) on the free surface to suppress refraction effects. This configuration could possibly jeopardize the non-intrusive nature of the setup. As shown in figure 3.1(b), it was decided to use a hollow cylinder made of Plexiglass and implement solution b).

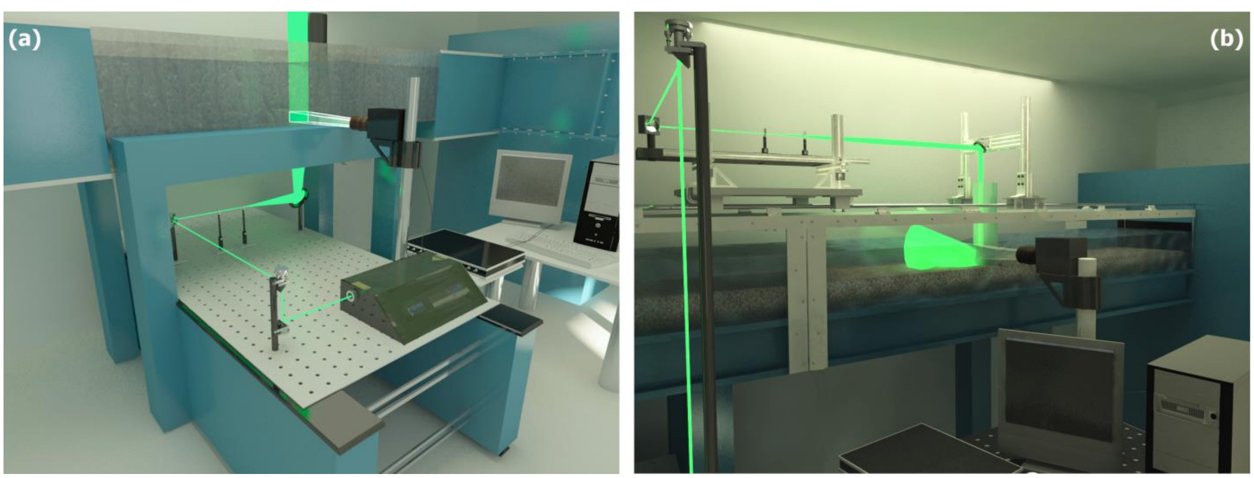

Figure 3.1-Physical model and basic parts of the non-intrusive PIV setup for: (a) smooth and (b) rough bed tests. Water flows from left to right in both cases.

In addition to the streamwise−wall-normal plane at the centerline junction, flow measurements were performed at a second station located five cylinder diameters upstream of the cylinder. These data were used to characterize the free-stream flow. Table 3.1 summarizes the results as well as other important information related to the identity of the tests. For the RB case, U_o was substantially lower than the critical velocity for the inception of sediment motion. Therefore, and in the absence of suspended sediments, an immobile and porous boundary comprised the roughness layer. It is possible that for the flow blockage ratios of 14.5% (SB) and 12.7% (RB) the sidewalls had a small effect on the flow at the centerline junction (Sumer & Fredsøe 2006). For both tests, glass thermometer measurements showed that the water temperature (T) remained practically constant (±0.1^{o}C) throughout data acquisition. Finally, the levels of Froude ($Fr_H = \frac{U_o}{\sqrt{gH}}$, where g is the gravitational acceleration) and Reynolds ($Re_D = \frac{U_o D}{\nu}$, where ν is the kinematic viscosity of water) numbers for the two tests are reasonably close for practical engineering purposes, allowing for meaningful comparisons (table 3.1). Overall, the good agreement between results reported herein and replication runs (one for each test) validated the consistency of experimental setups and methods.

Table 3.1-Major geometric and flow characteristics of experiments

Test	U_o (m/s)	D (m)	H (m)	δ_{99} (m)	T (^{o}C)	Fr_H	δ_{99}/D	H/D	Re_D
SB	0.486	0.089	0.180	0.077	23.5	0.36	0.87	2.02	4.7×10^4
RB	0.332	0.152	0.165	−	19.7	0.26	1.08	1.08	5.0×10^4

3.2.2 Flow diagnostics

Digital Particle Image Velocimetry was used to probe into the flow physics. Due to limitations in the availability of hardware, different PIV systems were assembled for each case. Measurements for SB were obtained with planar Time-Resolved Particle Image Velocimetry (TRPIV). On the other hand, a standard PIV (sPIV) system was employed for the RB test. The validity of the comparison between results from the two systems is discussed in the Appendix. The next paragraphs highlight similarities and differences between each PIV configuration. Regardless of the characteristics and capabilities of each system, best practices of PIV application (as documented in PIV literature (Raffel et al. 2007; Adrian & Westerweel 2011)) were enforced for both cases.

A high-speed CMOS camera and a high-repetition rate Nd: YLF laser were the basic parts of the TRPIV system. Their frequency of operation was set to 1,000 Hz, so that images could be recorded according to the continuous-rate mode. The maximum available image size at this frequency was 1,280 pixel × 1,040 pixel. For the given frequency/image size combination, the 4 GB-buffer of the camera was filled in 3.27 s. A magnification factor of 63.52 μm/pixel balanced the conflicting goals of probing a sizeable field of view at high spatial resolution. This resulted in a maximum error of 1.35% affecting regions at the outer edges of the images due to deviations of the viewing angle from the optimum of 90^o. Hollow glass spheres with an average diameter of 35 μm, specific gravity of 1.08 and Stokes number of 0.0051 were used to trace flow trajectories. Homogeneous seeding was obtained by mixing water and particles into the storage tank of the water tunnel. Out-of-plane motion of the seeding particles was mitigated by adjusting the thickness of the laser sheet to 2.0±0.2 mm. A convex lens with a focal length of 50 mm and a spherical lens with a focal length of 300 mm were used for this purpose. Inside the cylinder, a custom-designed convex mirror with a focal length of 23 mm was installed to expand the width of the laser sheet. The final product was a set of 3270 diffraction-limited images of white particles on a black background, with average particle diameter of 2.3±0.5 pixel and density equal to 0.043 particles/pixel^2.

The sPIV system consisted of a machine vision-type camera equipped with a CCD sensor and an Nd: Yag laser. The maximum operating frequency of the camera was limited to 15 Hz. Therefore, the frame-straddling mode was selected to ensure optimum particle displacements between successive exposures. The downside of the low sampling rate was counterbalanced by the fact that measurements were statistically independent (time autocorrelation coefficients for velocity signals were consistently less than 15% throughout the flow domain for the time lag of 133 ms) and the data acquisition lasted for 448.8 s. The increased sampling period was due to the capability of the camera to log recorded images directly on the hard drive of the computer. In this fashion, 3,366 image pairs were stored and used to generate an equal number of instantaneous flow fields. The size of each photo was 1,600 pixel × 1,200 pixel. The increased distance between the laser plane and the camera axis for this test (due to the greater width of the flume) entailed several changes in the setup compared to that of the SB test. In particular, the magnification factor was 43.47 μm/pixel, which reduced the error due to divergence from the optical axis down to 0.98%. Silver-coated, hollow glass spheres (average diameter: 85 μm, specific gravity: 1.1, Stokes number 0.0067) were used to increase the intensity of reflected light. The laser beam was manipulated into a 3.0±0.2 mm- thick sheet using a convex lens with a focal length of 75 mm and a spherical lens with a focal length of 1,000 mm. The average particle image diameter was 2.1±0.5 pixel and the imaged particle density was 0.035 particles/pixel^2.

3.3 Methods of data analysis

3.3.1 Particle Image Velocimetry

Despite the differences between TRPIV and sPIV systems, data from both cases were analyzed using common techniques. A number of image preconditioning operations were applied to raw images such as: intensity capping and gradient-based edge detection, masking of stationary objects, and subtraction of time-averaged image (Honkanen & Nobach 2005; Shavit, Lowe & Steinbuck 2007). Instantaneous velocity fields were extracted from successive PIV images using software that implements a Robust Phase Correlation kernel (Eckstein, Charonko & Vlachos 2008; Eckstein & Vlachos 2009). Multigrid iterative deformable windows (Scarano 2002) were used to probe the turbulent shear flows under investigation. Three passes with two iterations in each and 75% overlap between the interrogation windows were applied. To mitigate the adverse effects of excessive in-plane particle motion on the spatial correlation signal, discrete window offsetting (Westerweel 1997) was used for the second and third pass. Spurious velocity vectors were identified through a combination of velocity thresholding and Universal Outlier Detection (Westerweel & Scarano 2005). For these unacceptable measurements, “corrected” values were obtained through the application of nearest-neighbor algorithms on an eight-point stencil. Snapshots of instantaneous flow fields comprised of 26,742 velocity vectors for SB and 35,781 data points for RB test. The total number of measurements collected for both experiments was 207,865,660.

3.3.2 Proper Orthogonal Decomposition

The vast amounts of data typically obtained in PIV experiments are amenable to further analysis using post-processing techniques. One major objective is to extract information about the underlying physical mechanisms by reducing the dimensionality of the data set. This is frequently achieved using modal decomposition (Jolliffe 2002). Whereas an a priori selection of the modes (or basis functions) is possible, it has been suggested that, for the analysis of turbulent flows, ad hoc functions might be a better alternative (Lumley 1967). The decisive criterion for the optimality of the process requires that the empirical modes have the largest projection to the original data set.

Proper Orthogonal Decomposition (POD) is an analytically-founded statistical technique, which reduces complex flow fields using energetically-optimum basis functions (Berkooz, Holmes & Lumley 1993). Considering that the energy content of a moving fluid is proportional to the square of its velocity, POD delivers the smallest number of modes necessary to approximate the original flow field with the smallest possible error (in a least square sense). In other words, the POD-generated basis functions capture more of the kinetic energy of the system than any other decomposition. This makes the technique ideally-suited for the study of flows where large-scale, energetic flow structures dominate.

The general expression for the decomposition of a discrete velocity signal u, measured in M realizations varying in the two-dimensional space x(x, y) and in time t, is:

$$u(\boldsymbol{x}, t) = \sum_{m=1}^{M} a_m(t)\varphi_m(\boldsymbol{x})\,. \qquad (3.1)$$

Here, φ is the m-th basis function (or mode) and α is a coefficient. Each mode is a deterministic function in space, whereas the coefficients are stochastic variables in time. Although Eq. (3.1) expresses essentially a linear operation, there is no restriction for extending its application to non-linear systems. Note also that several types of basis functions could potentially comprise the partial sums of Eq. (3.1). Two additional conditions need to be satisfied, however, in order Eq. (3.1) to exclusively express Proper Orthogonal Decomposition (Holmes 2012).

The first condition imposes the orthonormality of the basis functions:

$$\iint \varphi_m(\boldsymbol{x})\, \varphi_n(\boldsymbol{x})\, dx\, dy = \delta_{mn}\,, \tag{3.2}$$

where δmn stands for Kronecker's delta. In this case, the m-th coefficient is uniquely related to the m-th mode through the following relationship:

$$a_m(t) = \iint u(\boldsymbol{x}, t)\, \varphi_m(\boldsymbol{x})\, dx\, dy\,. \tag{3.3}$$

The second condition ensures the optimality of the decomposition regarding the energy content of the signal. This is achieved when the basis functions are the eigenfunction solutions of the Fredholm integral equation of the second kind:

$$\iint R(\boldsymbol{x}, \boldsymbol{x}')\, \varphi_m(\boldsymbol{x}')\, dx\, dy = \lambda_m \varphi_m(\boldsymbol{x})\;, \tag{3.4}$$

where R(x, x′) is the kernel of spatial cross-correlation and λ is the m-th eigenvalue of the corresponding basis function. The aggregate of the eigenvalues expresses the total energy of the flow field. The contribution of each mode to the total energy of the system is the relative fraction of its corresponding eigenvalue as described in Eq. (3.5). It is customary in POD to arrange modes in descending order so that the first modes become the ones that capture the most energetic flow patterns (large-scale, coherent structures).

$$Energy\ Fraction\ (EF)_i = \frac{\lambda_i}{\sum_{j=1}^{M} \lambda_j}\ . \tag{3.5}$$

The methodology described so far constitutes the standard version of POD, also known as direct POD. Sirovich (1987) introduced a variation, which is particularly attractive for the decomposition of PIV data. Essentially, he suggested to substitute the spatial cross-correlation kernel R(x, x′) in Eq. (3.4) with the temporal cross-correlation kernel C(t, t′), defined for the total sampling time (ST) as:

$$C(t,t') = \frac{1}{ST} \iint u(\boldsymbol{x},t)\, u(\boldsymbol{x},t')\, dx\, dy \ . \tag{3.6}$$

This change reduces the computational cost, if the total number of instantaneous data snapshots is smaller than that of measurements contained within each field. Hence, the method is known as snapshot POD.

For this study, we applied snapshot POD on the fluctuating signals (time-averaged values subtracted) characterizing the streamwise and wall-normal velocity components for SB and RB tests. The reduced computational cost of this method compared to direct POD allowed us to take advantage of the maximum spatial and temporal resolution of the PIV data.

3.4 Results and discussion

PIV data favor the presentation of results in 2D-maps. Non-dimensionalization of the results is performed using characteristic quantities for length (D), time (D/U_o), and velocity (U_o). Since flow enters the domain from the left, a rectangular is drawn on the right of every map to indicate the location of the cylindrical obstacle. The origin of the coordinate system is the intersection of the leading edge of the obstacle with the wall. The horizontal axis (x) is aligned with the direction of the approach flow, y-axis is parallel to the cylinder, and z-axis is perpendicular to the measurement plane. The velocities in the x and y directions are u and v, respectively.

3.4.1 Time-averaged flow and turbulence statistics

Reynolds decomposition is employed to extract the time-averaged streamlines from PIV data (figure 3.2). The topology of the SB case is dominated by two foci of closed streamlines organized in an elliptical or spiral pattern (figure 3.2a). In the literature (Simpson 2001), the flow structure on the right is known as the primary vortex (HV1) and the one on the left as the secondary vortex (HV2). Both vortices gain strength through the same sources, namely the separated boundary layer flow and the reverse flux of fluid that had previously stagnated at the face of the obstacle. The close interaction between the HV1 and the HV2 is also inferred by their proximity. Note also the higher density of streamlines comprising the HV1, which in conjunction with its size, suggest its predominance on the dynamics of HVS. Overall, the two-vortex model presented here bears strong resemblance to those documented in published studies (Paik et al. 2007; Koken & Constantinescu 2009; Sabatino & Smith 2009). On the contrary, measurements over the rough wall revealed a new topology (figure 3.2b). The absence of any structure manifested with closed streamlines is the most striking characteristic of this flow field. Whereas streamline curvature is evident in the stagnation region, it appears that reversed fluid does not exhibit rotational motion, suggestive of a vortex. It is plausible that time-averaging filters out vortical structures with highly unsteady behavior in time. Past studies have documented a tertiary vortex (HV3) in instantaneous flow fields, even when no evidence was provided for such a structure in the time-averaged topology (Praisner & Smith 2006a, b). A closer inspection of the streamlines near the rough wall allows for additional hypotheses. In particular, the path of these streamlines seems to terminate at the wall. This could be suggestive of fluid infiltration into the porous layer. Alternatively, the irregular shape and random orientation of the gravel could deflect fluid elements away from the thin measurement plane. This would entail a continuous wandering of the vortex along the z (spanwise) direction. Additional work is required to test these hypotheses, because planar PIV precludes flow measurements within the hyporheic zone or outside the laser light plane.

The comparison is then focused on the spatial distribution of the velocity magnitude of the flow. There is a notable similarity regarding the levels and patterns of momentum entering the domain. In both tests, the maximum influx occurs at the upper left corner contributing some 65% − 70% of the freestream momentum. The nearly parallel shape of contours indicates a uniform retardation of flow as it approaches the solid boundaries and experiences stronger pressure gradients. Two exceptions to this trend are identified. The first occurs near the face of the cylinder, where masses of downward-deflected fluid form a jet-like structure that propagates towards the wall. The second exception is found close to the horizontal bed, where fluid of high velocity is moving opposite to the direction of the bulk flow. Nevertheless, the magnitude and extent of this latter flow pattern differs between the two experiments. For the RB test, high velocities are limited to a thin strip, which is surrounded by flow of lower velocity (figure 3.2b). On the contrary, for the SB test the reversed jet is wider and becomes part of the lower HV1 (figure 3.2a). Here, another connection with the HV1 is evidenced on its upper side, where a thin vertical band of high-velocity fluid feeds directly the vortex core. This infusion of momentum within a vortical structure could have important implications on the vortex−wall interaction mechanism (Paik et al. 2007).

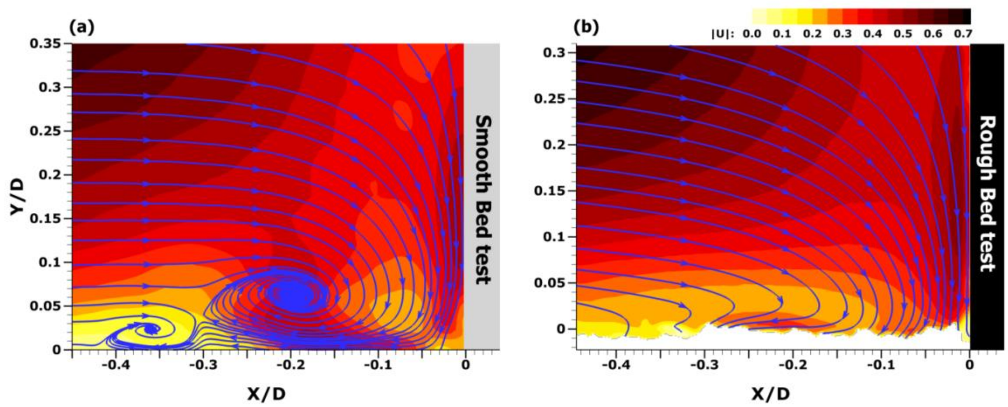

Figure 3.2-Time-averaged streamlines drawn on top of flood contours of non-dimensionalized velocity magnitude, |U| for: (a) smooth and (b) rough bed case.

The rotational content of the junction flows is further investigated through maps of spanwise vorticity (figure 3.3). Vorticity of negative sign is prevalent in both junctions. For the SB case, however, high concentration areas coincide with the locations of the primary and secondary vortex (figure 3.3a). In addition, an elongated patch of negative vorticity emanates from the downflow at the face of the cylinder and stretches all the way to the HV1. This is indicative of the strong interplay between these two flow structures (downflow and primary vortex). Streaks of positive vorticity appear in the immediate vicinity of the wall and the cylinder. At their ends, the thin streaks are transformed to elliptical or circular blobs of vorticity, which imply the sporadic presence of a tertiary and a corner vortex (CV).

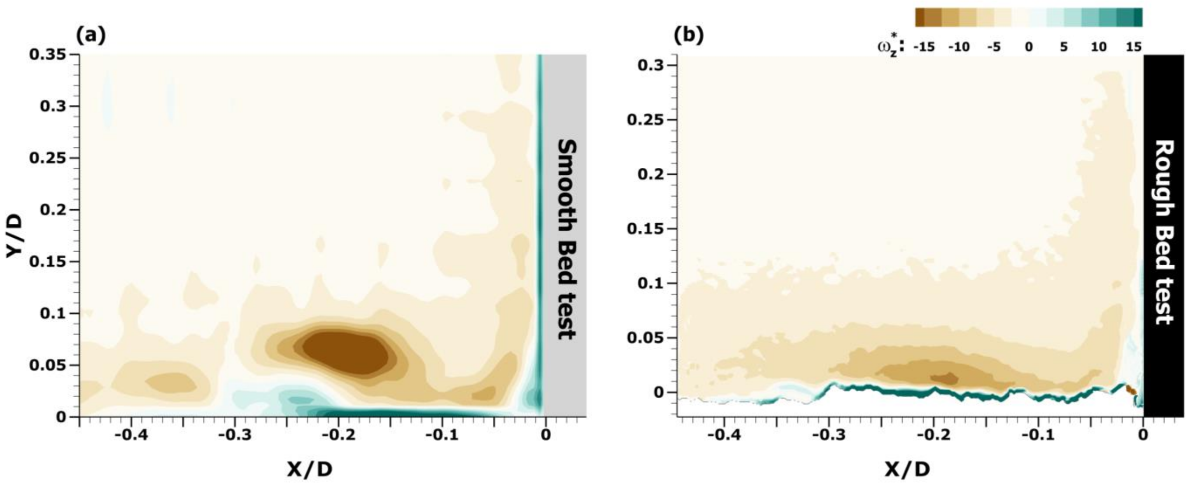

Figure 3.3-Spatial distribution of non-dimensional spanwise vorticity. (a) SB test, (b) RB test.

On the other hand, the rotational characteristics of the RB flow are more subtle (figure 3.3b). The overall levels of negative vorticity are lower compared to those calculated for the SB test. This parameter peaks at a single blob centered on dimensionless x, y coordinates: (−0.18, 0.01). The particular location could potentially be home to a vortex. Nevertheless, the origin of such a structure could possibly differ from that of the HV1 (or HV2) as manifested in the SB test. In the presence of roughness (and due to the proximity to the bed) the formation of a vortex could be attributed to flow separation at the edges of sediments that protrude into the flow field. Regardless of the origin of the elevated vorticity, this parameter diffuses gradually and in a relatively uniform fashion with height. Eventually, it assumes near-zero values above the average threshold of Y/D≈0.1. Finally, positive vorticity for the RB case is concentrated exclusively within a thin layer that develops on top of the crests of roughness elements (figure 3.3b). The time-averaged analysis does not support spatial connections between this layer and other flow structures.

Figures 3.4 and 3.5 elaborate the turbulent characteristics of the flows under investigation. The turbulence kinetic energy obtains its highest levels within the core and the periphery of the HV1 (figure 3.4a). Overall, however, TKE retains higher values throughout the RB junction (figure 3.4b) compared to those of the SB case. Differences also exist with respect to specific flow characteristics.

Focusing initially on the SB results, the increased turbulence energy is not confined within the locus of the HV1 (figure 3.4a). Observe that a band of high TKE emanates from the wall at an oblique angle and extends to the lower part of the HV1. The energy contained in the band is contributed by the fluctuations of the streamwise velocity component (figure 3.5a). These fluctuations establish the unsteady behavior of the near-well jet of reversed fluid. The combined impact of the unsteadiness of the jet and its interplay with the HV1 play a pivotal role on the HVS destabilization mechanism proposed based on the episodic extraction of near-wall fluid (Paik et al. 2007). Furthermore, increased TKE close to the origin of the coordinate system further supports the hypothesis for the intermittent presence of a CV.

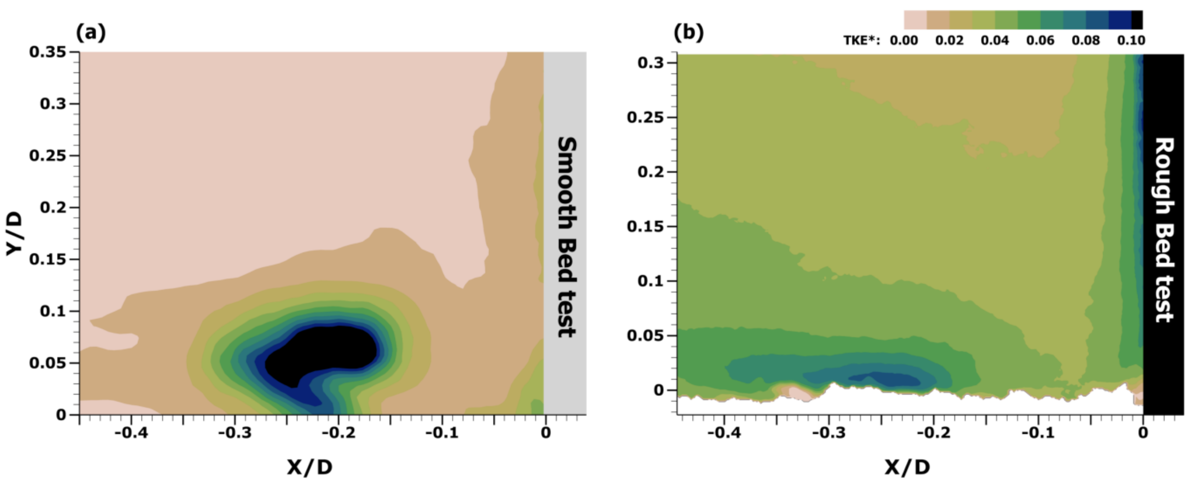

Figure 3.4-Non-dimensionalized turbulence kinetic energies (TKE) for: (a) smooth and (b) rough bed case.

Two prominent flow features dominate the turbulence kinetic energy field of the RB junction: the downflow adjacent to the cylinder and the horizontal, near-wall jet (figure 3.4b). Recall that these were also evident on the velocity map (figure 3.2b). It is shown here that the structures under consideration are rich in both momentum and turbulence. In support of this statement, turbulence intensity contours in figure 3.5(b) highlight the contribution of each velocity component. Near the cylinder, the turbulent content is expressed almost exclusively through fluctuations in the wall-normal velocity. The dark flood contours versus the blue line contours disclose a difference of nearly an order of magnitude. On the other hand, near the rough wall the disparity is not as pronounced.

Whereas the streamwise fluctuations (red line contours) predominate, fluctuations of the wall-normal velocity component remain relevant (gray flood contours). Besides, of interest is the gradual transformation of the turbulence intensity in the central region of the domain, which bridges the two characteristic features elaborated here. The velocity fluctuations vary in a nearly uniform fashion (figure 3.5b), without exhibiting the intricacy and the spatial inhomogeneity documented at the SB junction (figure 3.5a).

At a smaller scale, the effects of the microtopography of the wall are evidenced just upstream of a sediment grain protruding from the average bed level (x=−0.3D). A pocket of low turbulence energy and intensity is resolved at the stoss side of this bed irregularity. This “sheltered” area is also characterized by low levels of vorticity (figure 3.3b) and possibly of flow recirculation (figure 3.2b).

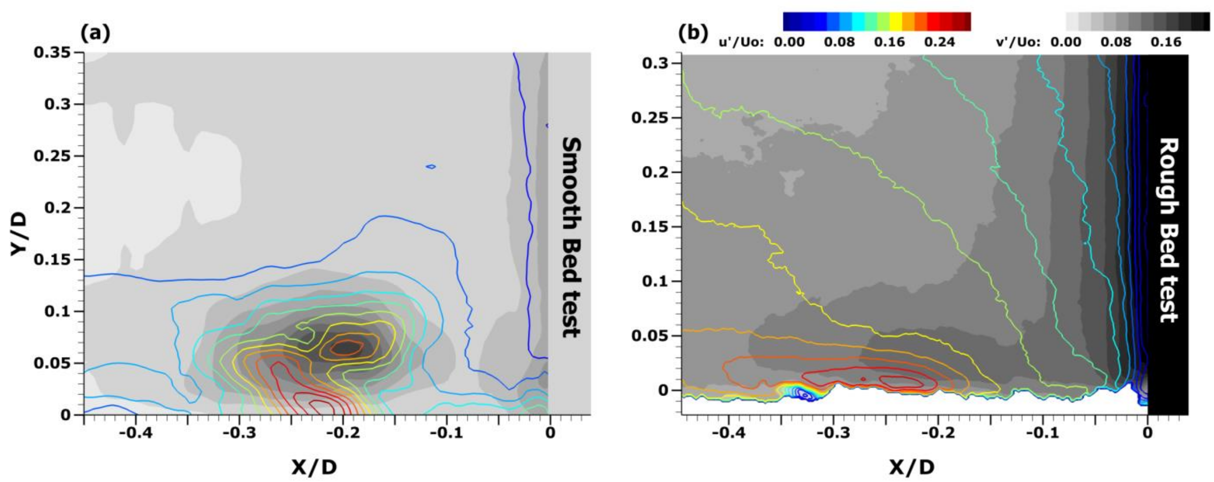

Figure 3.5-Contour lines of streamwise turbulence intensity drawn on top of flood contour maps of wall-normal turbulence intensity. (a) SB test, (b) RB test.

3.4.2 Instantaneous velocity fields

To take full advantage of the information contained within PIV data, a meticulous, frame-by-frame analysis of the resolved flow fields was performed. The cinematography was constructed using every instantaneous PIV snapshot and using the full spatial resolution of measurements. TRPIV data maximized the benefits from such an analysis. For the sPIV data, the identification of meaningful patterns posed a greater challenge. Nonetheless, it was still possible to shed insights on the physics of junction flows that were not detectable in the time-averaged analysis.

The number of vortices and their interactions defined the dynamics of the HVS for the SB case. Every flow field (frame) comprised of at least one vortex. The maximum number of vortices resolved in the junction region was five. Therefore, the topologies observed on a frame-by-frame basis were more complex compared to their time-averaged representation (figure 3.2a). Although seemingly random at a first glance, the behavior of the HVS was not devoid of organized patterns. For example, the well-known modes for junction flows (zeroflow and backflow) were identified on a number of frames. It was also found that for a significant amount of time the flow characteristics did not comply with those of the mentioned modes: the strong near-wall jet of reverse flow that extends to the far upstream of the junction (backflow, see figure 3.6a) or the blockage of this jet and its vertical ejection (zeroflow, shown in figure 3.6c). Many of the topologies describing a novel flow model were actually intermediate states of flow between the extreme modes (figure 3.6b). Hence, the introduced mode is referred to as intermediate. Due to its presence at approximately 1/3 of the total time, the direct switching between zeroflow and backflow was not always the case. The implications of this modification could potentially stretch to a number of phenomena that have been attributed to the mode-switching mechanism (Simpson 2001).

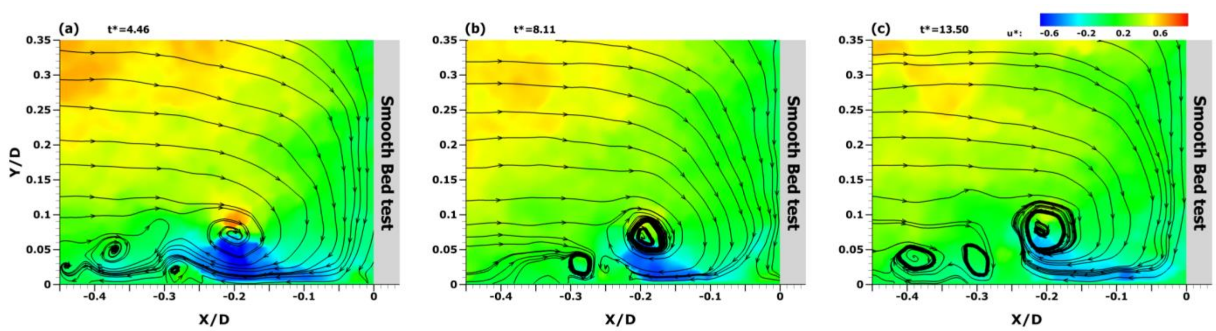

Figure 3.6-Illustration of characteristic flow modes for SB test: (a) backflow, (b) intermediate, and (c) zeroflow. Instantaneous streamlines are drawn on top of instantaneous streamwise velocity (non-dimensionalized). The dimensionless time of each frame is indicated with t*.

Time-resolved analysis revealed additional details about the wall-vortex interactions, which were introduced in the previous section. Figure 3.7 consists of two episodes indicative of this mechanism. The first one describes the extraction of positive vorticity from the wall, resulting from the complex interplay between the HV1, the reverse near-wall jet, and incoming flow that has leapfrogged the HV2 (figure 3.7a). The extracted vorticity does not diffuse into the flow field. Instead, it is captured and recirculates within the HV3. Recall that time-averaged analysis furnished scant direct evidence for the existence of this vortex. Figure 3.7(a) also suggests that the high vortical contents of the HV1 and the reverse near-wall jet are instrumental in shaping the dynamics of a new vortex (HV3). This is justified by the absence of a quaternary vortex (HV4) upstream of the HV2. Although the flow features around HV1 and HV2 are topologically similar, the reduced levels of vorticity within the HV2 and the jet underneath prevent the creation of HV4. On the other hand, the second episode of figure 3.7(b) demonstrates that in the absence of secondary vortices, wall-ejected fluid penetrates deeper into the junction flow. In subsequent frames, these vortical patches will diffuse or become advected by the outer streamlines of the HV1, until they join the near-wall jet and start a new cycle of activity.

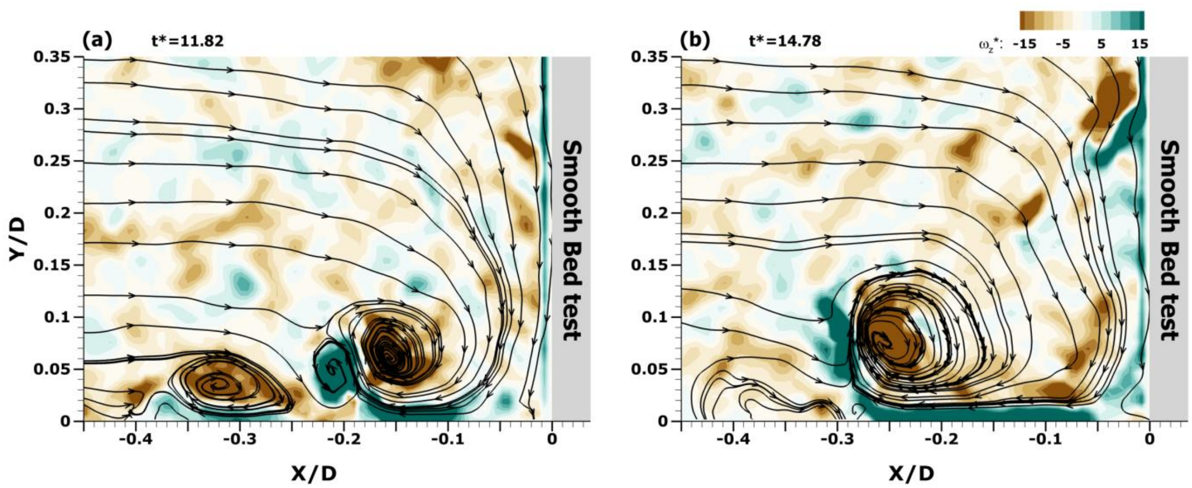

Figure 3.7-Instantaneous flow topologies for SB case demonstrating wall-vortex interactions: (a) HV1, HV2, and HV3 are present. (b) HV1 is dominant. Flow streamlines are superimposed on flood contours of the magnitude of non-dimensionalized, spanwise vorticity.

Fundamentally different were the results of the instantaneous flow analysis for the RB case. Video animations revealed a highly unsteady flow field, which was more difficult to interpret compared to that of the SB experiment. In several frames, there was little evidence of organized flow activity in the form of vortices with properly closed streamlines. Figure 3.8(a) is such an example. It is shown here that the near-wall region is home to small-scale structures, which do not exhibit the large-scale behavior of the HVS described in the SB test. Occasionally, separated flow at the junction would reorganize into patterns that are more coherent. The maximum number of vortices detected for the rough HVS system is two (figure 3.8b). These structures are of similar magnitude in size and coherence. As such, they do not comply with the characteristics of the smooth HVS model, according to which the HV1 consistently overwhelmed the other vortices in size (figure 3.6, figure 3.7). Furthermore, the fleeting presence of these flow patterns renders any effort to decipher vortex-to-vortex interactions unrealistic. This intermittency, which often results in an erratic character of flow changes between frames, is also evidenced in the form of open streamlines. Three of them were identified at various locations of the domain in figure 3.8(b). Finally, two characteristic topologies are reported for the downflow at the face of the cylinder. The first, which occurs in 96% of time, consists of a downward-deflected jet similar to the one observed in the SB test. The second topology (present in the remaining 4% of time) is characterized by small vortices. These run down the face of the cylinder, rotate in a counterclockwise sense, and disappear from the field of view just as they are about to encounter the rough bed.

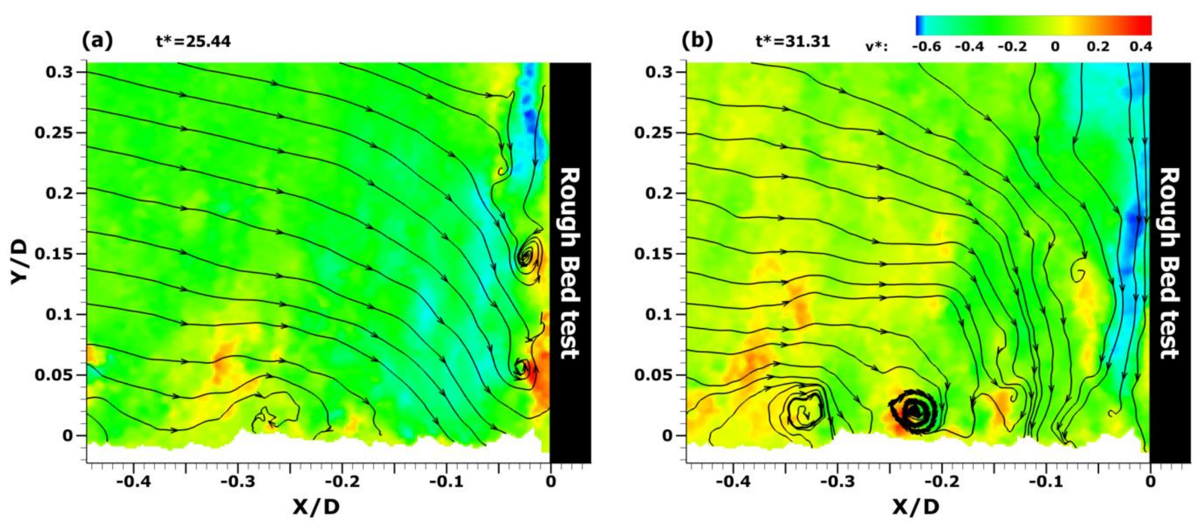

Figure 3.8-Characteristic snapshots of the RB flow field: (a) vortices running down the face of the cylinder, (b) vortices developing along the rough wall. Flood contours display instantaneous wall-normal velocity.

The discussion on the dynamics of the junction flow over a rough wall concludes with the description of an organized flow episode. This is illustrated with a sequence of four instantaneous flow field snapshots comprising figure 3.9 (a-d). The focus is on the larger-scale flow pattern that enters the junction domain from the left bottom at the dimensionless time of t*=111.64 (figure 3.9a). The development of a single vortex so far upstream was not observed in any frame of the video animations for the SB flow. In the presence of a rough bed, the vortex progressively moves closer to the cylinder, despite the strong near-wall jet propagating in the opposite direction (figure 3.9b). It is possible that the propulsion of the vortex is facilitated by the influx of high-momentum fluid at the mid and top of the domain (areas colored in orange and red). The footprint of the vortex does not remain constant. It is subject to expansion (figure 3.9b) and contraction (figure 3.9c). Eventually, this flow structure is disintegrated at t*=120.40 (figure 3.9d). The loss of its coherence coincides with the retreat of high-momentum fluid.

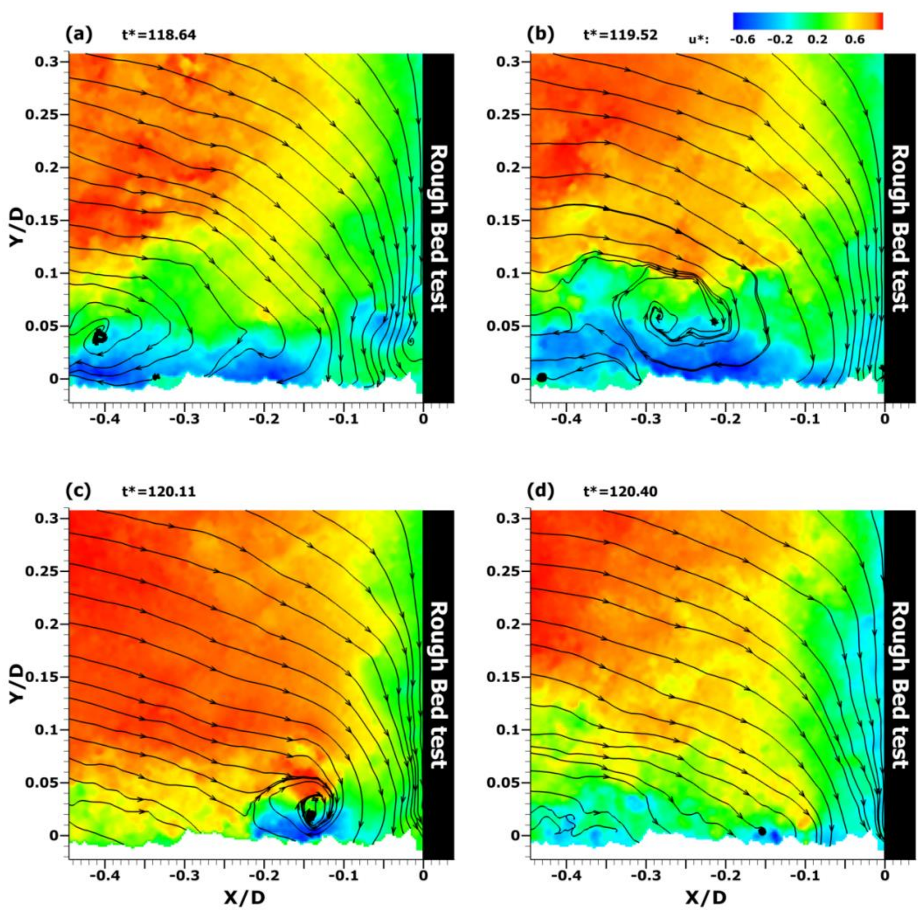

Figure 3.9-Sequence of snapshots displaying the unsteady vortex dynamics for the RB test. Background contours are colored with the instantaneous streamwise velocity.

3.4.3 POD modes

The number of POD modes necessary to reconstruct the original signal to a predetermined -though generally arbitrary- degree indicates the level of flow organization. Regular flows, with periodic characteristics in space and time require relatively few modes (low dimensionality). On the other hand, POD yields an increased number of modes for highly unsteady and inhomogeneous flows (high dimensionality). Figure 3.10 displays the energy content of the POD modes for the SB and RB tests. For both cases, most of the energy is contained in the first two modes. The energy fraction for modes 1 and 2 is 13.98% and 9.42% for the SB case. The corresponding EFs for the RB test suggest more energetic modes, measuring 28.78% and 15.24%. Nonetheless, all these numbers fall in the low range of values reported in the literature. It is not uncommon the first few modes of turbulent processes describing other systems to capture more than 80% of the total energy (Cruz et al. 2005; El Hassan & Meslem 2010; Nguyen et al. 2010). In our study, it required 10 modes for the SB case and 4 modes for the RB case to capture 50% of the total kinetic energy. For the level of 90%, the numbers of modes are 145 and 140 respectively. Due to the elevated energy content of the first two modes, energy convergence for the RB case is faster than that of the SB case for the first 160 modes. At this threshold, the cumulative energies assume nearly identical values and, from this point on, their convergence continues at practically equal rates until 100% is recovered.

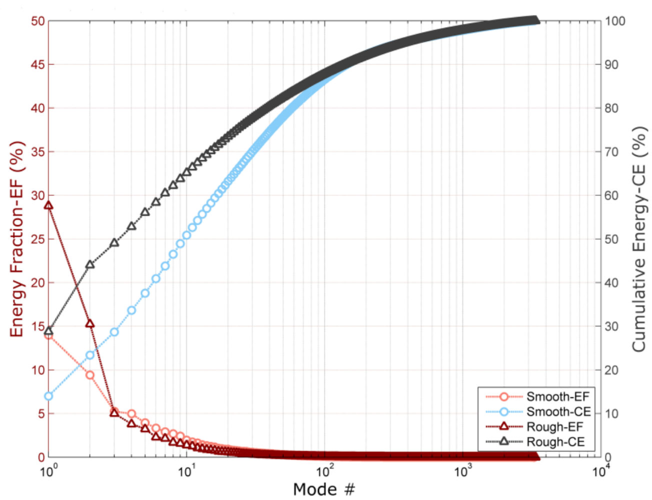

Figure 3.10-Energy fraction (EF) and cumulative energy (CE) distribution of the POD modes.

Prior to the analysis of the dominant POD modes, it is reminded that they are projections of the most energetic flow patterns on the spatial domain. The mechanics of POD ascribe a deterministic character to these spatial structures. Therefore, POD modes are not to be interpreted similarly to typical flow fields (§3.4.1). For this reason, they are drawn as continuous lines that are reminiscent to streamlines (pseudostreamlines), but contain no information about the direction of flow motion. Furthermore, the POD modes are superimposed on flood contour maps of their Euclidean norm, which has the following general form for the m-th mode:

$$\|\varphi_m(\boldsymbol{x})\|^2 = \varphi_{um}^2(\boldsymbol{x}) + \varphi_{vm}^2(\boldsymbol{x}). \qquad (3.7)$$

Based on the rapid decay of modal energy (figure 3.10), the analysis focuses on the leading four eigenmodes.

Modes 1 through 4 for the SB experiment are shown in figure 3.11 (a-d). Four structures characterize the most energetic mode (figure 3.11a). Three of them appear close to the bed and are, logically, related to the HVS. In particular, the two structures closer to the cylinder could express the preferable locations of HV1 in an energy-wise sense. The third one, further upstream, manifests in the area of action of HV2. The interpretation of the fourth structure appearing at the left top of the domain is not straightforward. It is conjectured that it cumulatively conveys the high-energy content of the incoming flow. Of interest are also the areas flooded in red color, where the Euclidean norm peaks. The one with the round shape expresses the kinetic energy of the HV1. The second provides additional evidence to support the mechanism discussed in previous sections and consists in the near-wall extraction of fluid resulting from the interaction of the lower part of the HV1 with the bed. Mode 2 is described with only one characteristic structure representative of a HV1 topology, which was also observed in several frames of the flow cinematography (figure 3.11b). The Euclidean norm of the u and v POD submodes is again higher at the neighborhood of the HVS, but is characterized by lower concentrations compared to those of mode 1. This parameter regains high values on the third most energetic decomposition (figure 3.11c). There is a striking similarity between the areas of increased $||\varphi||^2$ shown here with those of mode

1. Most likely, these express the same flow mechanism and their re-appearance in a subsequent mode underscores the importance of their role. Pseudostreamlines of mode 3 allude to a train of organized structures at the HVS region (four in number). Here, for the first time POD resolves a flow structure that is candidate for expressing the CV. The last mode examined for the SB test consists of three patterns worth commenting on (figure 3.11d). The ones close to the wall most likely represent the same physical processes in the HVS examined in previous modes. In this case, however, they are shifted spatially to the upstream of the junction. Regarding the larger structure near the cylinder, it is postulated that together with the adjacent vertical band of high $||\varphi||^2$ indicate the energetic content of the downflow.

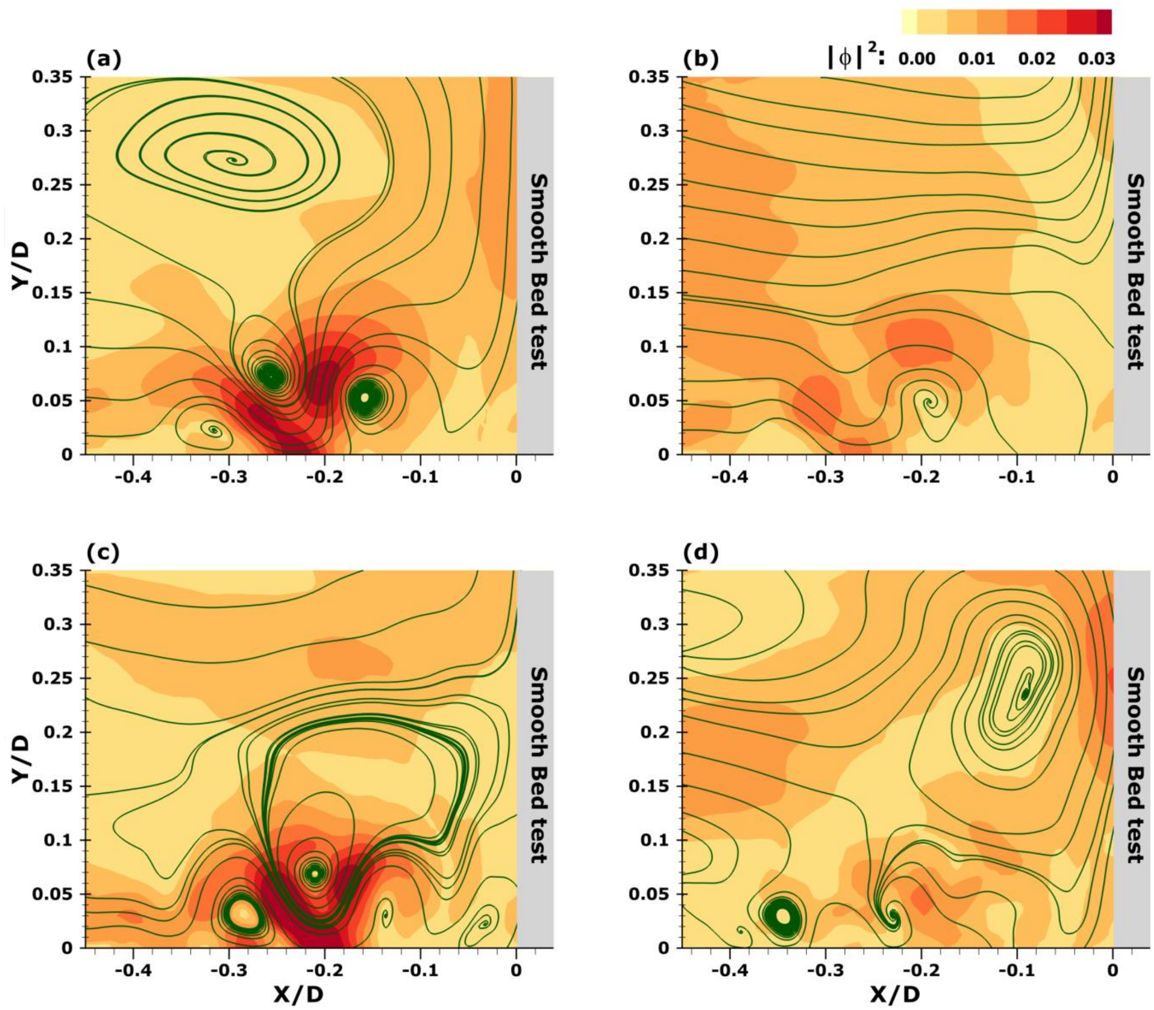

Figure 3.11-(a) First, (b) second, (c) third, and (d) fourth POD mode (pseudostreamlines) for the SB test. In the background, flood contour plots map the distribution of the Euclidean norm of the decomposition for the streamwise and wall-normal velocity.

The examination of the corresponding POD modes for the RB test disclosed significant differences compared to the SB experiment (figure 3.12). To begin with, the energy of the first mode is not distributed to any structure reminiscent of those typically found in junction flows (figure 3.12a). Pseudostreamlines are organized in a nearly parallel fashion. In addition, the concentration of the Euclidean norm suggests the higher energy content of the incoming flow (left) as opposed to that of the stagnation region (right). Mode 2, on the other hand, is characterized by a dominant structure centered on (−0.29, 0.12). The distance from the rough boundary casts doubts about the connection of this feature with the HVS (figure 3.12b). Besides, a trail of higher concentrations of $||\varphi||^2$ crosses different areas of the flow field, such as the upper part of the incoming flow, the downflow at the face of the cylinder, and the reversed flow jet near the bed. For the latter, an increment in the concentration at a narrow band between −0.20D and −0.32D complements the time-averaged analysis and establishes the importance of the jet in terms of energy content. This is further justified by the presence of this feature in the third POD mode (figure 3.12c). The role of the two dominant structures shown on this map, however, is not as clear. In particular, the structure on the right top consists of numerous pseudostreamlines that organize around their center. It could be plausible that such a pattern focuses the kinetic energy of fluid in the stagnation region. On the other hand, there is more confidence that the other structure (the one located closer to the bed) expresses one of the positions assumed by the intermittent vortices of the HVS. Another position is suggested on the map of mode 4 (figure 3.12d). In this case, the energetic structure is located closer to the cylinder. Due to its size, it is most likely to represent the HV1 (instead of the CV, which is typically smaller). Finally, the small-scale structure resolved at (−0.40, 0.12) eludes a straightforward interpretation. The same holds for similar structures that increase in number and appear more often as the rank of modes increases.

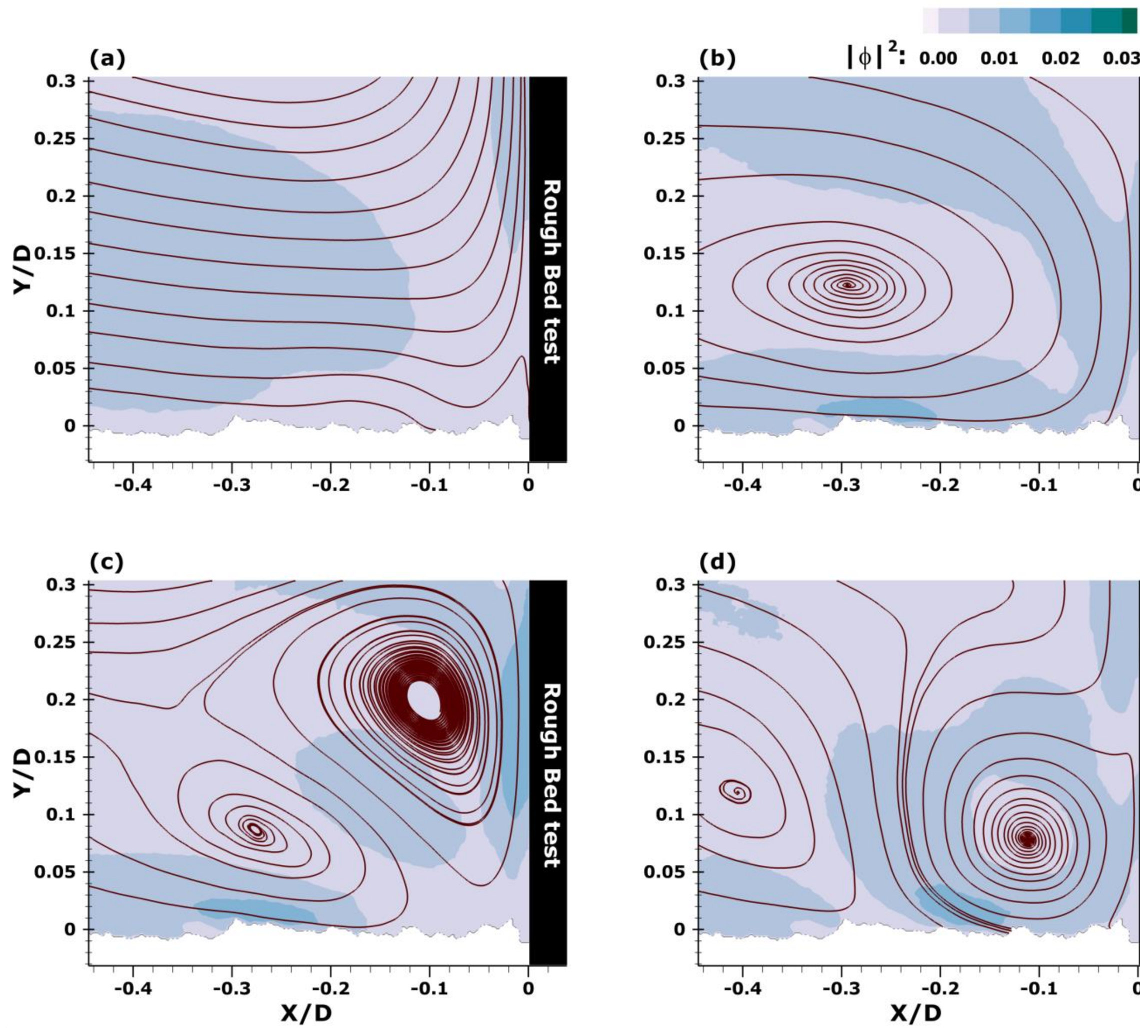

Figure 3.12-Most energetic POD modes (pseudostreamlines) for the RB test: (a) first, (b) second, (c) third, and (d) fourth. The flood contour maps represent the Euclidean norm of the decomposition for the streamwise and wall-normal velocity signals.

3.5 Conclusions

Time-averaged flow maps and turbulence statistics provided a first approximation on the effects of wall roughness. The most striking finding was the roughness-induced modulation on the large-scale characteristics of junction flow, manifested with the absence of properly closed vortical structures. The RB flow also experienced extensive diffusion of vorticity, turbulence intensity, and turbulence kinetic energy throughout the domain. On the smaller scales, bed surface irregularities modified the local streamline curvature. This induced pockets of low turbulence (stoss side) alternating with more energetic flow patterns (lee side). Nevertheless, qualitative and quantitative similarities also existed regarding the levels of momentum entering the junction, the prevalent sign of vorticity for the incoming flow, the reverse near-wall jet, and the downflow.

The instantaneous analysis elucidated the dynamics of two phenomena unique to the SB test: the presence of an intermediate flow mode and the ejection of wall fluid due to wall−vortex interactions. The well-defined flow topologies resolved in this test enabled the presentation of the unsteady dynamics of the HVS in an organized fashion. On the contrary, the rough wall entailed modifications to the degree of coherence of the flow. The smaller number of vortices, their seemingly erratic behavior, and their focus on new areas of action suggested a radically different HVS model for the RB test compared to that of the SB one. Important discrepancies also characterized the incoming flow: whereas for the latter test a key role for this flow feature was to impart momentum and energy directly on the HV1, for the former its main contribution consisted in the advection of the HV1 towards the cylinder.

Proper Orthogonal Decomposition proved to be a useful tool for the analysis of junction flows. For the SB test, the decomposition confirmed the major flow patterns derived from the time-averaged and time-resolved analyses. It also yielded information about new energetic structures present in the incoming flow and the downflow. Finally, POD rigorously established the wall−vortex interaction mechanism, which manifested with the ejection of near-wall fluid. For the RB data, spatial POD modes mostly revealed structures for which no indication had been provided through methodologies based on Reynolds decomposition. Although the role of these new structures is not always obvious, they are still worth considering within the frames of reduced order modeling. Regarding the mechanics of POD, the concentration of kinetic energy was higher for the leading modes of the RB experiment compared to those of the SB test. Nevertheless, for the relatively high Reynolds numbers investigated here, the energy contribution of these modes is not as great compared to that typically recovered in systems characterized by periodic flow elements. This finding confirms the aperiodic behavior of the HVS at the particular levels of Re. The convergence of modal energy was qualitatively and quantitatively similar for both cases, alluding to the minor impact that the smaller flow scales (introduced by the presence of roughness) have on the effectiveness on POD.

The results and conclusions of this work apply to the junction flow parameters and roughness geometry characterizing the specific experimental setups under consideration. Any effort for generalization should consider the limitations of the study, such as the use of different Particle Image Velocimetry systems and degree of development of the incoming flow. Upon consideration of these facts, the findings presented here could enhance the performance of generic models for junction flows based on theoretical arguments or numerical analysis. Benefits could also arise on the design of engineering applications, especially those characterized by irregular surface topographies (bridge pier scour, aerodynamics of damaged wing−fuselage junctions).

3.6 Acknowledgements

We thank Professor P. P. Vlachos and Dr. S. Raben for their help and insights regarding the application of Particle Image Velocimetry in turbulent flows. National Science Foundation (EAR 0738759) and the Research Office of the U.S. Army Corps of Engineers (ARO 53512-EV) funded this project. Nikolaos Apsilidis acknowledges the generous support he received towards the completion of the study from: Academy of Athens (Argyropoulos fellowship), Gerondelis Foundation, Geological Society of America, and Sigma Xi: The Scientific Research Society.

3.7 Appendix: Effect of sampling frequency on results

The comparison between two experimental configurations for junction flows is the backbone of this research project. The two setups shared similarities, but had also differences. As discussed previously, the major discrepancy that could potentially cast doubts on the validity of the results is with respect to the sampling rates of the PIV systems. According to what has been reported in junction flow literature (Devenport & Simpson 1990; Agui & Andreopoulos 1992; Kirkil & Constantinescu 2009), the low sampling rate of sPIV (7.5 Hz) should still suffice to resolve the behavior of the large-scale flow structures comprising the turbulent horseshoe vortex. Nevertheless, the nearly two orders of magnitude difference compared to the sampling rate of the TRPIV system (1,000 Hz) calls for further investigation. Towards this direction, downsampling on the TRPIV data was performed. Figure 3.13 (a-d) illustrates the effects of reduced sampling frequency on the time-averaged streamlines and vorticity field. The operation was extended to the intermediate frequencies of 250 Hz and 50 Hz for completeness. It is shown that the basic features of the HVS topology remain essentially the same. Reasonable agreement is found with respect to the vorticity magnitudes. Namely, the same structures are resolved in every subfigure. As expected, the fidelity of the spatial resolution degrades somewhat with the reduction of the sampling rate (maps appear more “noisy”), but only to a negligible degree considering the scope of this work. Similar analyses were performed for every other flow characteristic included in this paper, but not presented here to preserve the economy of writing space. Results verified again the validity of the adopted approach.

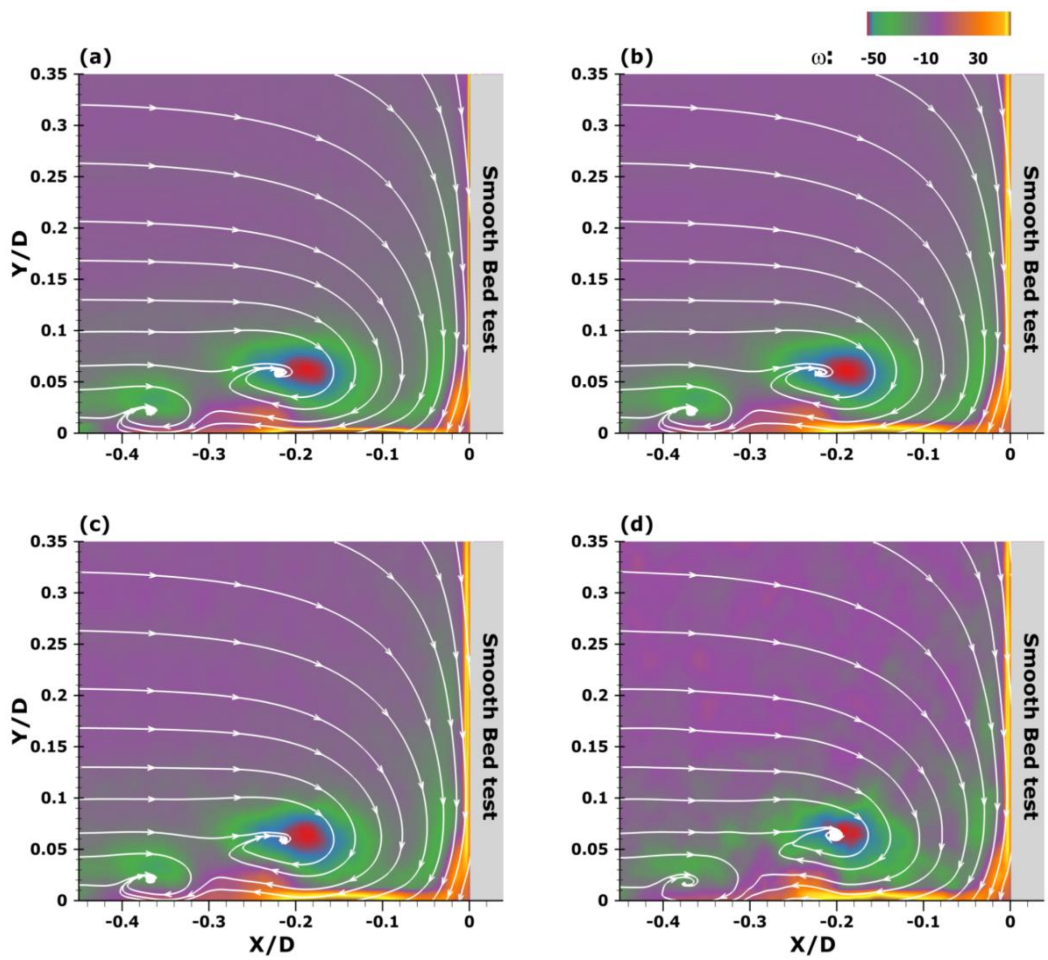

Figure 3.13-Time-averaged streamlines and spanwise vorticity resolved from measurements with sampling frequencies of: (a) 1,000 Hz, (b) 250 Hz, (c) 50 Hz, (d) 7.5 Hz.

3.8 References

ADRIAN, R. J. & WESTERWEEL, J. 2011 *Particle Image Velocimetry*. Cambridge University Press.

AGUI, J. H. & ANDREOPOULOS, J. 1992 Experimental investigation of a three-dimensional boundary layer flow in the vicinity of an upright wall mounted cylinder. *J. Fluids Engng* **114**, 566-576.

AHMED, F. & RAJARATNAM, N. 1998 Flow around bridge piers. *J. Hydraul. Eng.* **124**, 288-300.

BERKOOZ, G., HOLMES, P. & LUMLEY, J. L. 1993 The proper orthogonal decomposition in the analysis of turbulent flows. *Annu. Rev. Fluid Mech.* **25**, 539-575.

CRUZ, A., DAVID, L., PÉCHEUX, J. & TEXIER, A. 2005 Characterization by proper-orthogonal-decomposition of the passive controlled wake flow downstream of a half cylinder. *Exp. Fluids* **39**, 730-742.

DEVENPORT, W. J. & SIMPSON, R. L. 1990 Time-dependent and time-averaged turbulence structure near the nose of a wing–body junction. *J. Fluid Mech.* **210**, 23-55.

ECKSTEIN, A., CHARONKO, J. & VLACHOS, P. P. 2008 Phase correlation processing for DPIV measurements. *Exp. Fluids* **45**, 485-500.

ECKSTEIN, A. & VLACHOS, P. P. 2009 Digital particle image velocimetry (DPIV) robust phase correlation. *Meas. Sci. Technol.* **20**, 055401.

EL HASSAN, M. & MESLEM, A. 2010 Time-resolved stereoscopic particle image velocimetry investigation of the entrainment in the near field of circular and daisy-shaped orifice jets. *Phys. Fluids* **22**, 035107.

ESCAURIAZA, C. & SOTIROPOULOS, F. 2011 Reynolds number effects on the coherent dynamics of the turbulent horseshoe vortex system. *Flow Turbul. Combust.* **86**, 231-262.

FLACK, K. A. & SCHULTZ, M. P. 2010 Review of hydraulic roughness scales in the fully rough regime. *J. Fluids Engng* **132**, 041203.

GAND, F., DECK, S., BRUNET, V. & SAGAUT, P. 2010 Flow dynamics past a simplified wing body junction. *Phys. Fluids* **22**, 115111.

HOLMES, P. 2012 *Turbulence, coherent structures, dynamical systems and symmetry*. Cambridge University Press.

HONKANEN, M. & NOBACH, H. 2005 Background extraction from double-frame PIV images. *Exp. Fluids* **38**, 348-362.

JIMENEZ, J. 2004 Turbulent flows over rough walls. *Annu. Rev. Fluid Mech.* **36**, 173-196.

JOLLIFFE, I. T. 2002 *Principal component analysis*. Springer.

KIRKIL, G. & CONSTANTINESCU, G. 2009 Nature of flow and turbulence structure around an in-stream vertical plate in a shallow channel and the implications for sediment erosion. *Water Resour. Res.* **45**, W06412.

KIRKIL, G., CONSTANTINESCU, G. & ETTEMA, R. 2006 Investigation of the velocity and pressure fluctuations distributions inside the turbulent horseshoe vortex system around a circular bridge pier. In: R. M. L. Ferreira, E. Alves, J. Leal & A. H. Cardoso eds. *River Flow 2006. pp.* 709-718. Balkema, Lisbon.

KOKEN, M. & CONSTANTINESCU, G. 2009 An investigation of the dynamics of coherent structures in a turbulent channel flow with a vertical sidewall obstruction. *Phys. Fluids* **21**, 085104.

LUMLEY, J. L. 1967 The structure of inhomogeneous turbulent flows. In: A. M. Yaglom & V. I. Tatarski eds. *Atmospheric turbulence and radio propagation. pp.* 166-178. Nauka.

NGUYEN, T. D., WELLS, J. C., MOKHASI, P. & REMPFER, D. 2010 Proper orthogonal decomposition-based estimations of the flow field from particle image velocimetry wall-gradient measurements in the backward-facing step flow. *Meas. Sci. Technol.* **21**, 115406.

PAIK, J., ESCAURIAZA, C. & SOTIROPOULOS, F. 2007 On the bimodal dynamics of the turbulent horseshoe vortex system in a wing-body junction. *Phys. Fluids* **19**, 115104.

PATEL, V. C. 1998 Perspective: Flow at high Reynolds number and over rough surfaces-Achilles heel of CFD. *J. Fluids Engng* **120**, 434-444.

PRAISNER, T. J. & SMITH, C. R. 2006a The dynamics of the horseshoe vortex and associated endwall heat transfer - Part I: Temporal behavior. *J. Turbomach.* **128**, 747-754.

PRAISNER, T. J. & SMITH, C. R. 2006b The dynamics of the horseshoe vortex and associated endwall heat transfer - Part II: Time-mean results. *J. Turbomach.* **128**, 755-762.

RAFFEL, M., WILLERT, C. E., WERELEY, S. T. & KOMPENHANS, J. 2007 *Particle Image Velocimetry-A practical guide*. Springer.

ROULUND, A., SUMER, B. M., FREDSOE, J. & MICHELSEN, J. 2005 Numerical and experimental investigation of flow and scour around a circular pile. *J. Fluid Mech.* **534**, 351-401.

SABATINO, D. R. & SMITH, C. R. 2009 Boundary layer influence on the unsteady horseshoe vortex flow and surface heat transfer. *J. Turbomach.* **131**, 011015.

SAGAUT, P. 2006 *Large eddy simulation for incompressible flows: An introduction*. Springer-Verlag.

SCARANO, F. 2002 Iterative image deformation methods in PIV. *Meas. Sci. Technol.* **13**, R1-R19.

SHAVIT, U., LOWE, R. & STEINBUCK, J. 2007 Intensity capping: a simple method to improve cross-correlation PIV results. *Exp. Fluids* **42**, 225-240.

SIMPSON, R. L. 2001 Junction flows. *Annu. Rev. Fluid Mech.* **33**, 415-443.

SIROVICH, L. 1987 Turbulence and the dynamics of coherent structures. 1. Coherent structures. *Quarterly of Applied Mathematics* **45**, 561-571.

SPALART, P. R. 2009 Detached-Eddy Simulation. *Annu. Rev. Fluid Mech.* **41**, 181-202.

SUMER, B. M. & FREDSØE, J. 2006 *Hydrodynamics around cylindrical structures*. World Scientific Publishing.

TSIKATA, J. M. & TACHIE, M. F. 2013 Adverse pressure gradient turbulent flows over rough walls. *Int. J. Heat Fluid Flow* **39**, 127-145.

WESTERWEEL, J. 1997 Fundamentals of digital particle image velocimetry. *Meas. Sci. Technol.* **8**, 1379-1392.

WESTERWEEL, J., ELSINGA, G. E. & ADRIAN, R. J. 2013 Particle image velocimetry for complex and turbulent flows. *Annu. Rev. Fluid Mech.* **45**, 409-436.

WESTERWEEL, J. & SCARANO, F. 2005 Universal outlier detection for PIV data. *Exp. Fluids* **39**, 1096-1100.

4 Junction flow dynamics inside a developing scour hole

Nikolaos Apsilidis, Panayiotis Diplas, Clinton L. Dancey, and Polydefkis Bouratsis

ABSTRACT: Coherent flow structures play an important role in the onset of sediment transport and the development of scour holes around bridge piers. Point-wise velocity measuring techniques cannot resolve the spatial characteristics of these flow patterns in a conclusive way. Global flow diagnostic tools -such as the Particle Image Velocimetry (PIV)- are better suited for this purpose, but their application entails several technical challenges. We addressed these difficulties to a satisfactory degree by integrating custom-built equipment, sophisticated data processing software and state-of-the-art hardware into an in-house PIV system. PIV images captured the dynamic evolution of both flow and scouring at the upstream junction of a cylindrical pier in the presence of a mobile gravel bed. Based on the spatial distributions of the flow's momentum, energy, and vorticity it is demonstrated that the downwash jet along the leading edge of the pier is the dominant flow pattern. The absence of a horseshoe vortex suggests a modified mechanism for the initial stages of scouring around a bridge pier.

4.1 Introduction

In-stream structures affect the passage of water in rivers. The dynamic interaction between the structure, the flow, and the loose riverbed induces changes on local bed morphology. For example, as moving water approaches the junction between a bridge pier and the streambed, it encounters a buildup in pressure due to the presence of the obstacle. Consequently, the fluid's momentum and vorticity reorganize into a system of new flow patterns. These unsteady flow structures -horseshoe and wake vortices, fluid downwash at the front and accelerated flow at the sides of the pier- extend over an appreciable size of the flow domain. Their combined action increases locally the sediment entrainment rates and creates a scour hole around the pier. Engineering interest in the study of local erosion stems directly from the potential of these scour holes to compromise the serviceability and safety of the supported bridge.

Laboratory investigations have advanced our knowledge on the bridge scour phenomenon (Melville & Coleman 2000; Sotiropoulos, Diplas & Khosronejad 2012). Based on the application of dimensional analysis, experimentalists have been studying how scouring is influenced by factors related to the fluid flow, the sediment properties, and the geometry of the bridge foundations. Such results were typically incorporated into empirical equations for the prediction of scouring under a wide range of conditions (Sheppard, Melville & Demir 2013). These tools, however, have yet to meet global approval of engineers due to the unsatisfactory results obtained from field applications (Johnson 1995; Zevenbergen 2010). Other studies have focused on the physics of the phenomenon, in an effort to unveil its underlying mechanism (Dargahi 1990; Lee & Sturm 2009). These latter works furnished an enhanced understanding about bridge scour dynamics. Nevertheless, their findings were inherently constrained by the use of instrumentation that measured fluid velocities in a point-wise fashion and, therefore, did not allow the unambiguous characterization of the flow structures of interest.

Particle Image Velocimetry (PIV), is a global flow diagnostic technique capable of resolving the dynamics of large-scale flow patterns present in a number of fluid mechanics applications (Raffel *et al.* 2007; Adrian & Westerweel 2011). Its potential to contribute to scour-related research was recognized several years ago by Hill & Younkin (2006), but has yet to be fulfilled to a satisfactory extent. It is mostly technical challenges that have so far prevented the widespread use of PIV in bridge scour experiments. In particular, the options for the delivery of the laser light into the test section in a non-intrusive way are limited due to the presence of the opaque sediment layer and the pronounced fluctuations of the free surface close to the model. Another problem arises from the diffuse reflection of laser light on the sediment grains resulting in inferior PIV signals at near-wall regions. Finally, typical PIV systems are limited to continuous recording of data for a few seconds, which jeopardizes the convergence of turbulence statistics. All these difficulties explain the paucity of PIV studies in bridge pier scour (Unger & Hager 2007; Nogueira *et al.* 2008). They also justify why researchers who carried out these few studies resorted to important modifications in their setups to make PIV measurements possible (such as using a half-pier mounted at the sidewall of the channel, damping free surface oscillations with a transparent lid, and immobilizing the streambed in the neighborhood of the model pier).

Here, we present a laboratory experiment that overcomes the technical challenges of applying PIV in bridge pier scour, without the requirement to modify key characteristics of the physical model. The focus of this study is on the crucial phase at the beginning of the scouring activity. The objective is to provide a physics-based description of the phenomenon capitalizing on the high fidelity of a dataset obtained through non-intrusive measurements.

4.2 Experimental methods

4.2.1 Facilities, experimental materials and test parameters

The tests took place in a recirculating tilting flume with a 120 cm-wide cross section housed at the Baker Environmental Hydraulics Laboratory of Virginia Tech. A 16 cm-deep layer of crushed limestone comprised the channel's bed. To remove the very fine material from the gravel mixture, the aggregates were washed prior to their installation. The flume was filled progressively with gravel until the desired height was achieved. Soil compaction was not applied. The sediments were given the shape of a ramp with 29% at the beginning of the bed. The surface of the rest of the layer was leveled using a screed attached on an instrument trolley running along the rails of the flume’s sidewalls. The consistency of this methodology was verified through pointgauge measurements of the topography in the neighborhood of the model pier. The standard deviation of the bed elevation readings was 0.31 cm. Sediment granulometry (figure 4.1) was obtained through in-situ and bulk material sampling (ASTM Committee E-1 on Methods and Testing 1969). According to the results of the mechanical sieve analyses, the median grain size diameter was d_{50}= 0.364 cm and the geometric standard deviation of the particle size distribution $\sigma = \sqrt{\frac{d_{84.1}}{d_{15.9}}} = 1.34$. The non-cohesive material is, thus, classified as well-sorted, because it is characterized by a relatively uniform size distribution.

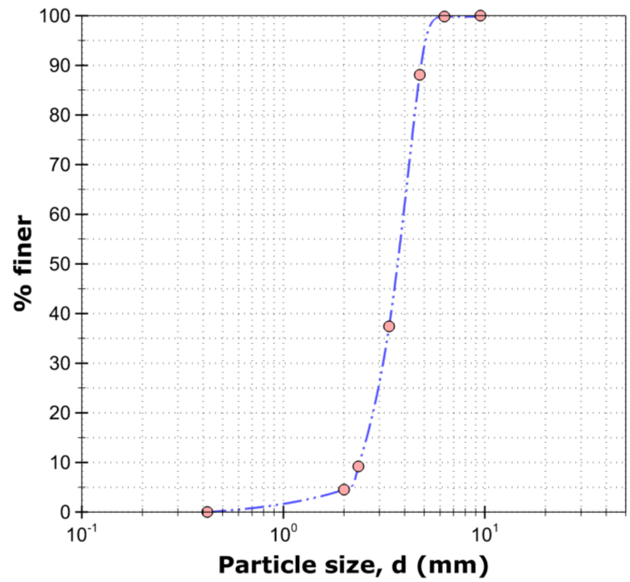

Figure 4.1-Grain size distribution of the sediments comprising the channel's bed.

A cylindrical model pier made of acrylic glass was installed on the mid-width of the channel and 8.25 m downstream of the end of the sediment ramp. The diameter of the pier was D=15.24 cm, the flow depth H=20.50 cm, and the depth-averaged velocity of the fully-developed flow U_o=54.70 cm/s. The levels of two dimensionless parameters frequently employed in bridge scour research, namely the Reynolds number based on the pier diameter (Re_D) and the Froude number based on the flow depth (Fr_H), were Re_D=81,900 and Fr_H=0.39.

4.2.2 Particle Image Velocimetry setup

Standard PIV (sPIV) was applied to yield two-component velocity measurements along a 2D-plane. The transparent pier allowed the delivery of the laser light through its interior (figure 4.2). A series of optics such as mirrors and lenses (cylindrical and spherical) transformed the laser beam into a thin sheet (figure 4.2a). The aggressive expansion of the light at the junction region was achieved by positioning a custom-designed, convex mirror with focal length of 23 mm inside the pier (figure 4.2b). The non-intrusive PIV setup also included a CCD camera (Pike F-505), which imaged the region of interest through the flume's sidewalls. The camera was tilted downwards at an angle of 24.7^o to capture flow within the scour hole. This introduced refraction and perspective errors in the PIV images. To account for these distortions, we took pictures of a precision-machined, calibration target immersed in running water. The black dots on the target's face were painted on a rectangular grid of 1.27 mm. A dewarping algorithm was used to rectify the geometry of the PIV images based on the location of the dots according to the procedure suggested by Soloff, Adrian & Liu (1997). Our system was capable of recording 1,600 pixel × 1,200 pixel images at a rate of 7.5 Hz. The images were transferred to a Mini-Mac computer equipped with a solid-state drive. This enabled the continuous imaging of the junction flow for 84 min. The fact that we did not interfere with the flow or immobilize the bed to facilitate data recording resulted in a physical model, which more accurately represented the actual phenomenon.

Additional PIV measurements were taken to characterize the approach flow and confirm that the boundary layer extended throughout the flow depth. In this case, the laser light was delivered through the free surface. In particular, a thin, streamlined window made of Plexiglass was suspended from the instrument trolley, so that it barely contacted the water's surface. The measurement area was stationed 50 cm upstream of the leading edge of the pier to ensure that flow was not affected by the obstacle. This distance satisfies criteria suggested from previous studies (Ahmed & Rajaratnam 1998; Unger & Hager 2006).

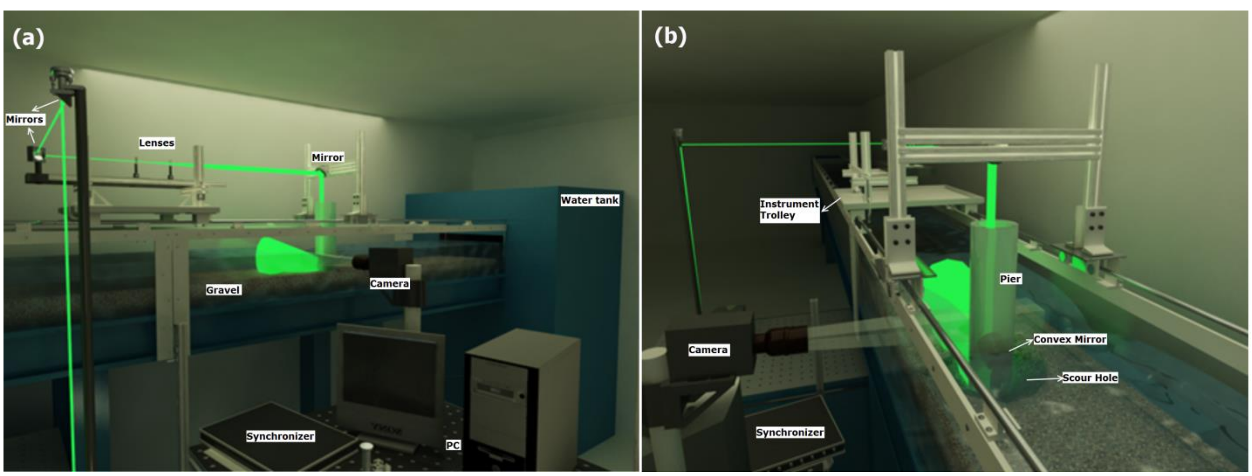

Figure 4.2-PIV setup. (a) General view, (b) detail close to the model.

4.2.3 Test procedures

Prior to the beginning of the test, water was recirculated in the flume until a relatively steady temperature of 21.0±0.2^{o}C was achieved. This value was very close to the room temperature of 20.5^{o}C, which was monitored using a thermocouple device and controlled throughout. This preliminary run also allowed water to “correct” possible irregularities of the sediment surface that could possibly exist at regions away of the test section. The flume was then carefully drained. The formal experimental procedure began shortly after seeding particles (silver-coated hollow glass spheres with a specific gravity of 1.1 and a median diameter of 85 μm) were added to the water stored in the tank up to a concentration of 7.82 g/m^3. The input hydrograph shown in figure 4.3 was applied. Flow discharge was increased progressively to the terminal rate of 151 l/s. Nevertheless, data acquisition had started earlier (at t=36 min), so that it coincided with the commencement of erosion at the flanks of the pier. We decided not to restrict scouring activity near the pier (for example, by temporarily installing a protective plate around it that would be removed once the terminal discharge had kicked in). This decision was based on results from extensive tests that had been performed to evaluate the effect of input hydrograph on the scour phenomenon. The first 24 min of data were recorded during the rising limb of the input hydrograph and the remaining 60 min were collected at steady inflow. The procedure was terminated as soon as approximately 90% of the hard disk’s capacity had been used.

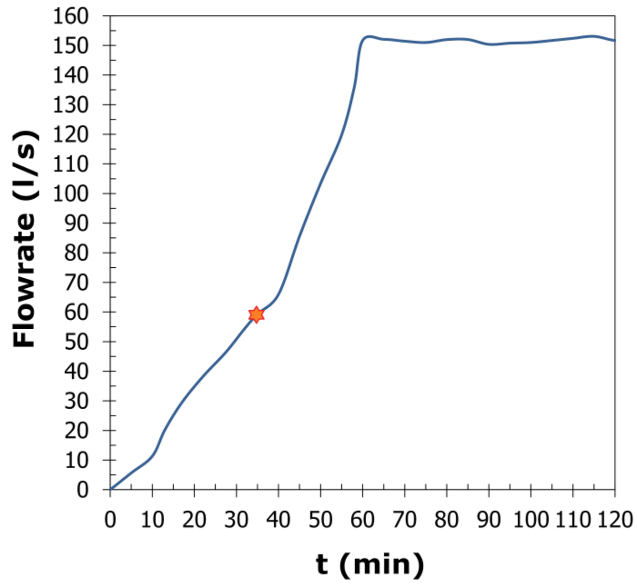

Figure 4.3-Input hydrograph. The star denotes the beginning of data acquisition, which ended at t=120 min.

4.2.4 PIV data processing

PIV images were processed in pairs with software that implements the Robust Phase Correlation (Eckstein, Charonko & Vlachos 2008; Eckstein & Vlachos 2009). As a result, the quality of resolved velocity fields should be considered superior compared to those derived from conventional cross-correlation algorithms. Signal-to-noise ratio of the PIV signal was enhanced through the application of several image pre-processing methodologies (Theunissen, Scarano & Riethmuller 2008; Mejia-Alvarez & Christensen 2013). Deformable interrogation windows with progressively smaller sizes were applied to scan paired photographs for correlated particle images (Scarano 2002). The optimum configuration consisted of three passes with two iterations in each. Well-established techniques, such as window offsetting (in passes two and three), overlapping (75%), and Universal Outlier Detection were applied to enhance the quality of the processed data (Westerweel 1997; Westerweel & Scarano 2005). A small number of spurious measurements (2.5% on average) had to be replaced using information from nearby velocity vectors. Bed elevations were also extracted from PIV images using in-house developed algorithms based on edge detection.

4.3 Results and discussion

The results presented herein refer to a flow episode during which the topography at the upstream bed−cylinder junction did not change. Although erosion was observed at other areas of the scour hole, the constant geometry along the centerline allowed the extraction of meaningful flow statistics. This analysis was also justified by the duration of the episode, which was 211.67t_{ch}, with $t_{ch}=D/U_o$ conservatively considered as the characteristic flow time. Therefore, Reynolds decomposition was applied on the streamwise (u) and wall-normal (v) velocity signals at the junction plane. In all figures, water flows from left to right. The origin of the coordinate system is the intersection of the leading edge of the pier with the unscoured bed. Illustrations depict flow and geometry properties made dimensionless using the appropriate characteristic length (D) and velocity (U_o).

Scouring occurred throughout the upstream centerline junction, but was more pronounced near the pier. There, the dislodgement of gravel created a cavity approximately 0.11D deep and 0.17D wide (figure 4.4). The streamlines superimposed on the flood contour plot reveal a constant inflow of water towards this cavity. Both direct freestream flow and flow that had been earlier deflected on the pier comprised the inflow stream. Observe that streamlines are open suggesting the absence of vortical structures from the time-averaged flow field. Furthermore, streamline curvature becomes noticeable for a small number of streamlines that encounter the bottom of the cavity and are deflected to the upstream due to local irregularities on the bed’s surface.

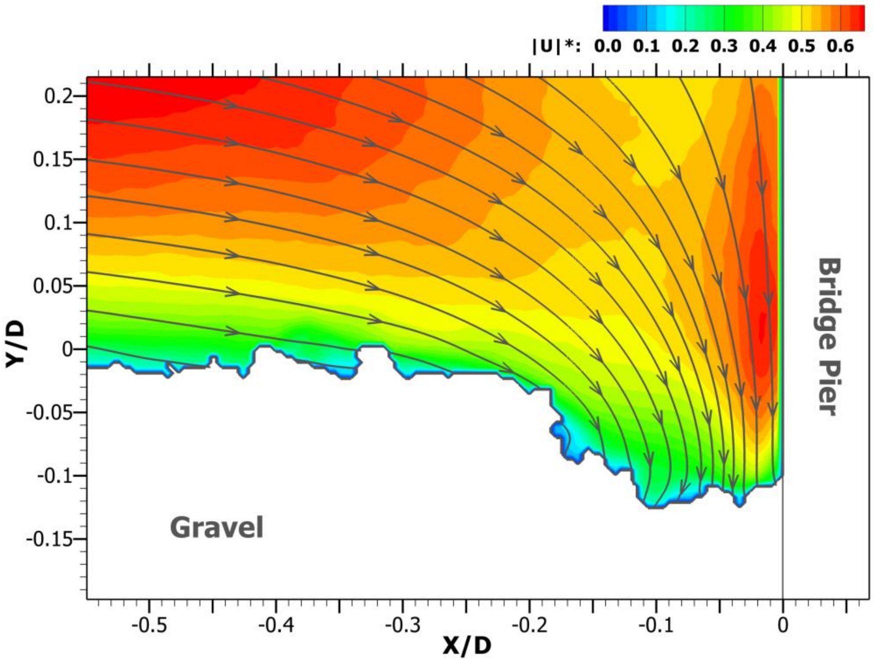

Figure 4.4-Flood contours of non-dimensionalized velocity magnitude and flow streamlines.

Different levels of momentum characterized these two inflow components. As evidenced from the colored contours of velocity magnitude, freestream fluid entered through the top left side of the junction region at velocities higher than 60% of U_o (figure 4.4). This flow experienced a gradual deceleration, due to mounting pressure imposed by the pier. Consequently, its velocity was reduced to 30% of U_o by the time it arrived into the scour hole. On the contrary, flow that had stagnated on the pier's face and was then directed downwards retained high levels of momentum. The rapid downwash of fluid manifests itself in the form of a vertical band of high velocities running down the face of the pier. Essentially, this characteristic flow pattern could be considered similar to a jet that impinges on the gravel bed and has the potential to amplify local scour rates. Noteworthy that the streamlines comprising this jet seem to end abruptly at the solid boundary. Due to the porous nature of the bed, some infiltration of the water into the sub-surface zone is plausible. Nevertheless, the relatively high flowrates of this test point at another interpretation. It is possible that fluid masses upon their contact with the bed are redirected towards the sides of the pier, where the scour hole is deeper. In other words, the geometry of the scour hole generates a favorable pressure gradient, which governs the trajectories of flow tracing particles. The sPIV technique stops short of resolving the third, out-of-plane velocity component. It is, therefore, not possible to test these assumptions using data from this experiment.

In addition to its high momentum, the downwash jet is characterized by increased levels of turbulence kinetic energy, TKE (figure 4.5). This quantity is defined as:

$$TKE = \frac{\overline{(u')^2} + \overline{(v')^2}}{2U_o^2}, \tag{4.1}$$

where u′ and v′ are the fluctuations of the streamwise and wall-normal velocity components. Again, a vertical band of elevated TKE distinguishes the downwash at the face of the pier from the freestream fluid reaching directly the scour hole. Furthermore, high turbulence energy underscores the unsteady character of this flow pattern. Additional data are required for a conclusive evaluation of the origin of the downwash jet and its characteristics. In particular, it is not clear whether the high energy and momentum content of the downwash jet originates from the approach flow or if it results from the favorable pressure gradient developing along the wall-normal direction due to the presence of the scour hole. Regardless of its origin though, the downwash of fluid at the pier's face is the dominant flow pattern at this phase of scouring.

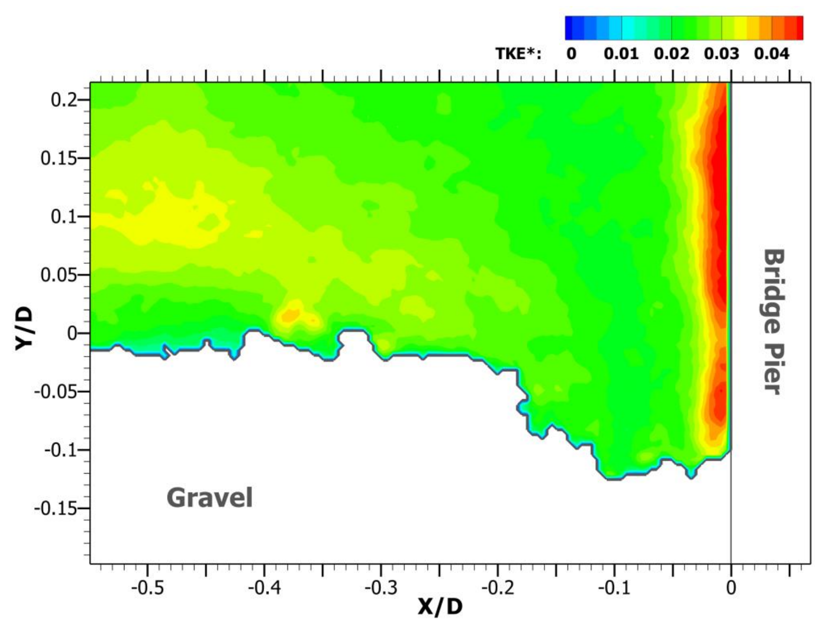

Figure 4.5-Flood contour plot of non-dimensionalized turbulence kinetic energy.

The presence of the downwash flow contrasts the absence of another characteristic flow pattern: the horseshoe vortex. The latter is a predominant feature of junction flows developing over smooth and impermeable walls (Simpson 2001). A horseshoe vortex is manifested in the form of closed streamlines organized in foci of elliptical or circular shapes. Vorticity at the vortex core is frequently one to two orders of magnitude higher than that measured in the surrounding flow (Apsilidis *et al.* 2010). The unsteady behavior of this coherent flow pattern results in elevated levels of TKE within and around its footprint (Devenport & Simpson 1990). In our study, the streamline topology does not indicate flow separation at the large scales that characterize the horseshoe vortex. Reversal of flow direction at similar scales does not occur either. Instead, fluid particles impinge directly on the gravel situated at the bottom of the scour hole. Furthermore, high levels of TKE were measured only in the immediate vicinity of the pier. This area is not likely to host a typical horseshoe vortex. Consequently, the increased TKE should be linked exclusively to the downwash fluid flow.

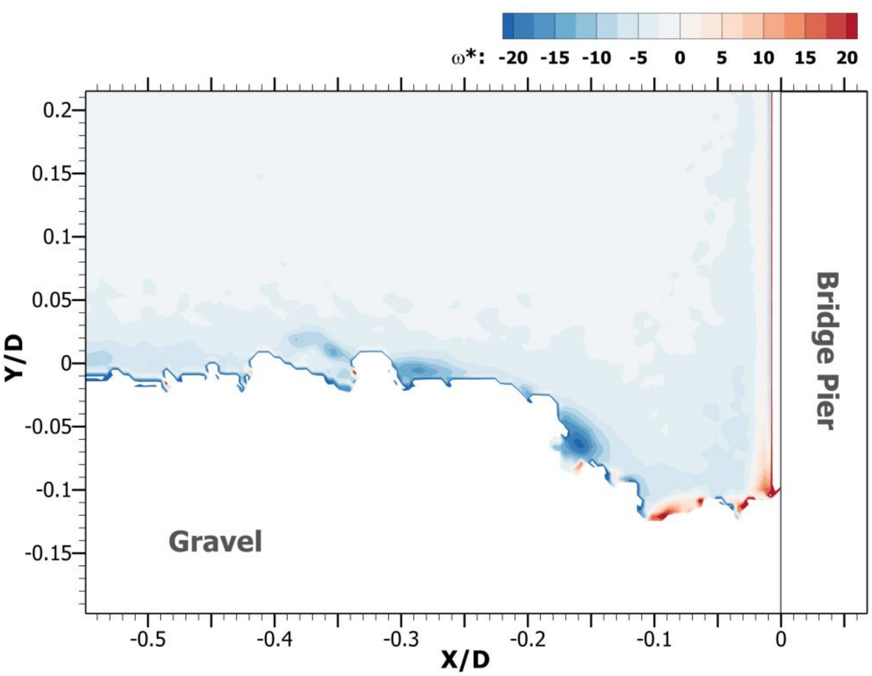

Figure 4.6-Non-dimensionalized spanwise vorticity plot.

The spanwise vorticity, ω, of the flow field is defined as:

$$\omega = \frac{\partial v}{\partial x} - \frac{\partial u}{\partial y}. \quad (4.2)$$

Its spatial distribution is mapped on figure 4.6. As expected for a wall-bounded flow, vorticity is concentrated near the solid boundaries and decays in the interior of the domain. Small patches of negative vorticity were found: 1) behind grains protruding from the bed, and 2) downstream of the rim of the scour cavity. The interpretation of these flow features is not obvious. Large velocity gradients in the near-wall region induce high shear, which could obscure the rotating motion of coherent structures. The so-called Q-criterion (Hunt, Wray & Moin 1988) was applied to address the dilemma of whether high-vorticity patches constitute coherent flow structures or are simply manifestations of intense shear. The mathematical formulation of this statement is given as:

$$Q = \frac{1}{2}(\boldsymbol{\Omega}^2 - \boldsymbol{S}^2), \tag{4.3}$$

with **Ω** expressing the rate of flow rotation and **S** the rate of strain. Higher Q-values establish stronger rotational motion and thus, the presence of coherent flow patterns. Colored contours on figure 4.7 identify regions where the rate of flow rotation overwhelms the rate of strain. While a generally accepted threshold has yet to be proposed, it is postulated that the high Q-values downstream of the rim of the scour hole indicate a small vortex created due to flow separation. The existence of additional flow patterns of similar nature in other regions is also demonstrated. Finally, note that areas of high Q (figure 4.7) are in good, but not in perfect agreement with areas of high ω (figure 4.6).

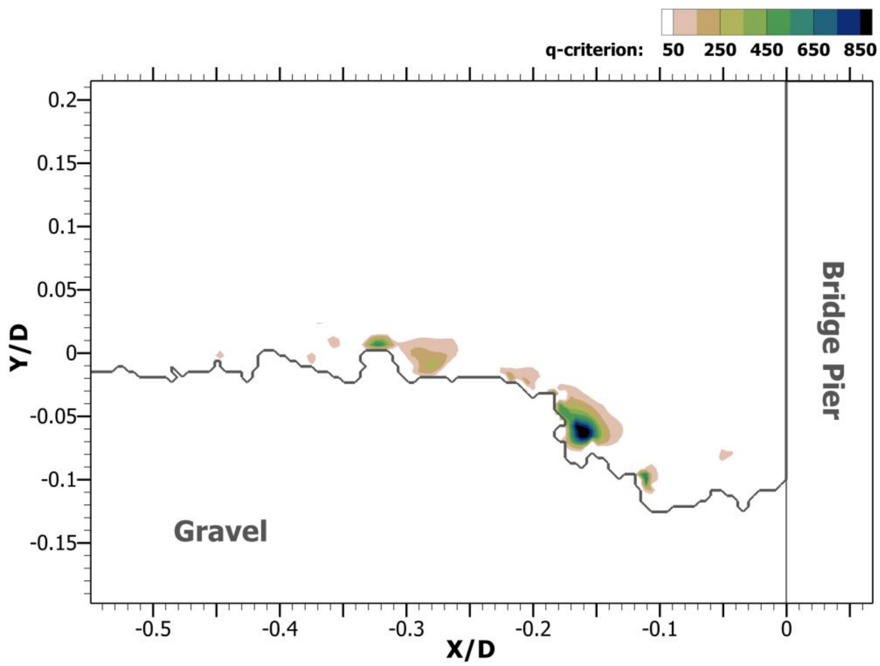

Figure 4.7-Results from vortex identification analysis based on the Q-criterion.

4.4 Conclusions

This study contributes a novel implementation of the state-of-the-art flow measuring technique of Particle Image Velocimetry within the frames of bridge scour research. Non-intrusive measurements resolved both the flow field and the bed topography at the upstream centerline plane of a sediment-embedded model pier. Through the analysis of high-quality experimental data, it was demonstrated that the downwash of fluid along the leading edge of the pier defined the flow topology. This flow, rich in momentum and energy, formed a scouring jet that impinged directly on the bed. Of importance is also the absence of a horseshoe vortex at these initial stages of the scouring activity. Instead, a number of small vortical structures were identified near the bed. These vortices formed downstream of bed irregularities due to flow separation, highlighting the effect of microtopography on the phenomenon. Scour countermeasures engineering could capitalize on the physical insight provided here, if the study's limitations are considered and the validity of results under a wider range of parameters is established. Nevertheless, -and to the best of our knowledge- this is the first non-intrusive study of bridge pier scour using the PIV technique and it is hoped that it lays the ground for future endeavors.

4.5 Acknowledgments

The National Science Foundation (EAR 0738759) and the Research Office of the U.S. Army Corps of Engineers (ARO 53512-EV) funded this study. Nikolaos Apsilidis gratefully acknowledges the support of the Academy of Athens, the American Society of Civil Engineers, the Geological Society of America, and Sigma Xi: The Scientific Research Society. Professor P. P. Vlachos kindly loaned the PIV instrumentation.

4.6 References

ADRIAN, R. J. & WESTERWEEL, J. 2011 *Particle Image Velocimetry*. Cambridge University Press.

AHMED, F. & RAJARATNAM, N. 1998 Flow around bridge piers. *J. Hydraul. Engng* **124**, 288-300.

APSILIDIS, N., DIPLAS, P., DANCEY, C. L., VLACHOS, P. P. & RABEN, S. G. 2010 Local scour at bridge piers: The role of Reynolds number on horseshoe vortex dynamics. In: S. E. Burns, S. K. Bhatia, C. M. C. Avila & B. E. Hunt eds. *5th International Conference on Scour and Erosion. pp.* 86-94. American Society of Civil Engineers, San Francisco.

ASTM COMMITTEE E-1 ON METHODS AND TESTING 1969 *Manual on test sieving methods*. American Society for Testing and Materials.

DARGAHI, B. 1990 Controlling mechanism of local scouring. *J. Hydraul. Engng* **116**, 1197-1214.

DEVENPORT, W. J. & SIMPSON, R. L. 1990 Time-dependent and time-averaged turbulence structure near the nose of a wing–body junction. *J. Fluid Mech.* **210**, 23-55.

ECKSTEIN, A., CHARONKO, J. & VLACHOS, P. P. 2008 Phase correlation processing for DPIV measurements. *Exp. Fluids* **45**, 485-500.

ECKSTEIN, A. & VLACHOS, P. P. 2009 Digital particle image velocimetry (DPIV) robust phase correlation. *Meas. Sci. Technol.* **20**, 055401.

HILL, D. & YOUNKIN, B. 2006 PIV measurements of flow in and around scour holes. *Exp. Fluids* **41**, 295-307.

HUNT, J. C. R., WRAY, A. A. & MOIN, P. 1988 Eddies, streams, and convergence zones in turbulent flows. In *Proceedings of the Summer Program*, Center for Turbulence Research, NASA, 193-208.

JOHNSON, P. A. 1995 Comparison of pier-scour equations using field data. *J. Hydraul. Engng* **121**, 626-629.

LEE, S. O. & STURM, T. W. 2009 Effect of sediment size scaling on physical modeling of bridge pier scour. *J. Hydraul. Engng* **135**, 793-802.

MEJIA-ALVAREZ, R. & CHRISTENSEN, K. T. 2013 Robust suppression of background reflections in PIV images. *Meas. Sci. Technol.* **24**, 027003.

MELVILLE, B. W. & COLEMAN, S. E. 2000 *Bridge scour*. Water Resources Publications, LLC.

NOGUEIRA, H., FRANCA, M. J., ADDUCE, C. & FERREIRA, R. M. L. 2008 Bridge piers in mobile beds: Visualization and characterization of the surrounding and approaching flows. In: M. S. Altinakar, M. A. Kokpinar, I. Aydin, S. Cokgor & M.S. Kirkgoz eds. *Riverflow 2008. pp.* 2397-2406. Balkema, Cesme/Izmir, Turkey.

RAFFEL, M., WILLERT, C. E., WERELEY, S. T. & KOMPENHANS, J. 2007 *Particle Image Velocimetry-A practical guide*. Springer.

SCARANO, F. 2002 Iterative image deformation methods in PIV. *Meas. Sci. Technol.* **13**, R1-R19.

SHEPPARD, D., MELVILLE, B. & DEMIR, H. 2013 Evaluation of existing equations for local scour at bridge piers Online. J. Hydraul. Engng doi: 10.1061/(ASCE)HY.1943-7900.0000800.

SIMPSON, R. L. 2001 Junction flows. *Annu. Rev. Fluid Mech.* **33**, 415-443.

SOLOFF, S. M., ADRIAN, R. J. & LIU, Z. C. 1997 Distortion compensation for generalized stereoscopic particle image velocimetry. *Meas. Sci. Technol.* **8**, 1441-1454.

SOTIROPOULOS, F., DIPLAS, P. & KHOSRONEJAD, A. 2012 Scour around hydraulic structures *Handbook of Environmental Fluid Dynamics. pp.* 69-84. CRC Press.

THEUNISSEN, R., SCARANO, F. & RIETHMULLER, M. 2008 On improvement of PIV image interrogation near stationary interfaces. *Exp. Fluids* **45**, 557-572.

UNGER, J. & HAGER, W. H. 2006 Temporal flow evolution of sediment embedded circular bridge piers. In: R. M. L. Ferreira, E. Alves, J. Leal & A. H. Cardoso eds. *River Flow 2006. pp.* 729-739. Balkema, Lisbon.

UNGER, J. & HAGER, W. H. 2007 Down-flow and horseshoe vortex characteristics of sediment embedded bridge piers. *Exp. Fluids* **42**, 1-19.

WESTERWEEL, J. 1997 Fundamentals of digital particle image velocimetry. *Meas. Sci. Technol.* **8**, 1379-1392.

WESTERWEEL, J. & SCARANO, F. 2005 Universal outlier detection for PIV data. *Exp. Fluids* **39**, 1096-1100.

ZEVENBERGEN, L. W. 2010 Comparison of the HEC-18, Melville and Sheppard Pier Scour Equations. In: S. E. Burns, S. K. Bhatia, C. M. C. Avila & B. E. Hunt eds. *5th International Conference on Scour and Erosion. pp.* 1074-1081. American Society of Civil Engineers, San Francisco.

5 Conclusions and future work

This study investigated junction flow phenomena through laboratory experiments. Particle Image Velocimetry resolved flow dynamics in a series of generic model configurations, characterized by increasing complexity. Whereas a fundamental approach was strategically adopted for this research, it is hoped that the findings are not devoid of merit for practical engineering designs. For this reason, it is reiterated here that the limitations of the models (explicitly stated previously) should be thoroughly considered prior to extending the results of this work to other models or prototypes.

The study on the classical smooth wall−cylinder configuration revealed a time-averaged topology for the HVS comprising of two major vortices, regardless of Re_D. It also underscored the importance of time-resolved analysis in deciphering the physics of junction flows. Using this tool, the topologies of well-established modes characterizing the behavior of the HVS (zeroflow and backflow) were revisited for each Re_D under consideration. An additional, intermediate mode was introduced and was shown to modify the mode-switching mechanics. Fresh evidence on the origin of the reversed flow and the near-wall eruption mechanism documented the effects of scale that reached beyond the HVS. It was concluded that the greater Re_D, the higher the unsteadiness of the primary vortex is growing. This trend was also mapped in space. Inflection points in the time-averaged velocity profiles combined with 2D probability density functions of velocity fluctuations indicated that unsteady regions extended from close to the wall, up to 0.1 cylinder diameters above it. Furthermore, emphasis was placed on the correct interpretation of bimodality in the p.d.f.s of velocity signals. Namely, it was demonstrated that defining the origin on the x-axis is a prerequisite for drawing meaningful conclusions. Upon such an analysis, maps of the bimodal regions for both velocity components were used to quantify scale effects on junction flow dynamics.

A rough and permeable wall induced noticeable changes on the large-scale characteristics of junction flows. The absence of properly closed vortical structures from the time-averaged topology attests to this statement. Differences were identified on smaller-scales too, compared to results from the smooth and impermeable wall test. It was found that irregularities on the wall's surface enhanced streamline curvature. This resulted, locally, in the formation of small-scale flow patterns. Besides, the inspection of instantaneous flow disclosed highly intermittent and irregular patterns. This called for additional investigation through Proper Orthogonal Decomposition. Higher rank POD modes resolved energetic structures that spread throughout the junction region. No evidence for some of these structures had been provided through the classic analyses based on Reynolds decomposition. Finally, the relatively low energy content of the leading POD modes verified the aperiodic behavior of the turbulent HVS at the investigated Reynolds numbers.

The last part of this work demonstrated the first non-intrusive application of PIV within the frames of bridge scour research. The technical challenges of such a task were addressed to a satisfactory degree by integrating custom-built equipment, sophisticated data processing software, and state-of-the-art hardware into an in-house system. The detailed documentation of these parameters is expected to guide future attempts and potentially help establish PIV as the definitive diagnostic tool for bridge scour research. In addition to the technical contribution, this experiment revealed a modified mechanism for the junction flow over a mildly-scoured bed geometry (early stages of scouring). In particular, results showed that the downward-deflected jet at the leading edge of the pier dominated the flow field. A possible implication of this finding is that the downflow (and not the HVS) assumes the leading role in scouring during the initial phase of the phenomenon.

The dissertation concludes with recommendations for future work. An apparent one would be the suggestion to extend the investigation on scale effects to models consisting of rough permeable walls (mobile and immobile). A conclusive assessment of such effects would become possible, if high-quality data are obtained in prototype conditions. Of interest would also be to measure flow velocities at additional locations within the junction. To that end and without disregarding the accompanying challenges, the application of advanced versions of PIV (Tomographic or Holographic) could provide a wealth of new information. The goal of a global representation of the phenomenon dictates synchronized measurements of velocity, heat transfer, body surface pressure, wall shear stresses, and bed elevation. Finally, it is emphasized that joint experimental−numerical studies are necessary for the rapid improvement in the predicting capabilities of existing models.